博士論文

Study of equilibrium and instabilities using a Rogowski probe in the TST-2 spherical tokamak

(球状トカマク TST-2 におけるロゴスキープローブを用いた平衡と不安定性の研究)

古井 宏和

Doctor thesis

Study of equilibrium and instabilities using a Rogowski probe in the TST-2 spherical tokamak

（球状トカマク TST-2 におけるロゴスキープローブを用いた平衡と不安定性の研究）

Hirokazu Furui

Department of Complexity Science and Engineering
Graduate School of Frontier Sciences
The University of Tokyo

Abstract

Tokamak is a candidate scheme for a fusion reactor, but the reduction of its aspect ratio is required to make an economically competitive reactor. Therefore, experimental data at small aspect ratio tokamaks (i.e., spherical tokamaks) are quite important to design a prototype fusion reactor. In TST-2 (Tokyo Spherical Tokamak-2), various issues, such as plasma start-up using radio frequency (RF) waves, plasma equilibrium, plasma turbulence, instabilities and disruptions, have been studied. Current density is closely related to them, since tokamak plasma are characterized by the current density profiles. Thus, the development of current density diagnostic is quite valuable in tokamak research.

In this study, the development of a current density diagnostic using a small Rogowski coil has been performed. A Rogowski coil is a current sensor and its general shape is a toroidal coil. The exclusive advantage of a Rogowski coil is the direct measurement of an electrical current passing through a hole of the coil. In order to measure the internal current density of spherical tokamaks, a high performance small Rogowski coil is required. Therefore, we have invented a multi-layer Rogowski coil (outer diameter = 20 mm; inner diameter = 12 mm; thickness = 12 mm; number of turn 360; and thickness of the cable = 0.12 mm) wound by a specific winding method, which enables us to fabricate a small Rogowski coil with small sensitivity to the external magnetic field and with large number of turns within a short fabrication time. Using this Rogowski coil, we have successfully measured the edge current density of TST-2 plasmas with a good signal to noise ratio.

A Rogowski probe consisting of two multi-layer Rogowski coil, five magnetic pick-up coils, and two Langmuir probes has been also fabricated. The feature of the Rogowski probe is that it can be moved along the major radius of the tokamak and rotated around the shaft axis (in the toroidal-poloidal plane). As a result, the current density, magnetic field and pressure profiles were obtained. In addition, the angular dependence of the current density in the toroidal-poloidal plane was obtained. It was found that the angular dependence cannot be explained by geometrical configuration but can be interpreted by the following model developed by us. We made a sheath model in the vicinity of the Rogowski probe head and calculated the electron orbits under a given magnetic field and the sheath potentials. The calculation revealed the effects of plasma parameters, including sheath potential. The experimental angular dependence was reproduced by our model. Furthermore, a part of the plasma parameter dependences were confirmed experimentally. This is the first study on the current passing through a hole in magnetized plasmas, and we have established the insertable Rogowski coil measurement.

Using the Rogowski probe, plasma equilibrium and the instabilities were studied. In Ohmic plasma discharges, we found that the measured edge current density profiles and those calculated by an equilibrium code agree each other when the plasma is in inboard-limited configuration. For the outboard-limited configuration, a finite current in the region outside the RF antenna limiter position was observed. Such current cannot be reconstructed

by the equilibrium code. In RF startup plasma discharges, which is sustained by a dielectric loaded 4 waveguide antenna, we successfully and directly observed local current density for the first time. On the other hand, the equilibrium calculation code which allows finite scrape off layer current failed to reproduce the measured local current density. Therefore, further improvement in plasma equilibrium calculations is required.

In the studies of instabilities, we mainly investigated the difference between two types of internal reconnection events (IRE, which are instabilities often observed in spherical tokamaks). One is that occurs at the initial and the middle phase of a discharge duration, and it often induces a plasma disruption. Second is that occurs at the end of a discharge duration and it does not induce a disruption. From the comparison between them, sudden emissions of soft X-ray and low frequency magnetic fluctuations near the core region were found to be the main two precursors for the IRE which induces a disruption. For both IREs, transports of plasma density and the current from the core region to the edge region are observed, and such transports seems to cause high frequency fluctuations near the plasma edge region. In addition to IREs, edge localized filamentary structures were also observed by the Rogowski probe. The Rogowski probe was found to be a powerful tool to measure and study such localized structures.

Finally, we have developed a high performance Rogowski coils, and demonstrated that the Rogowski coil is a powerful tool to measure the current densities, such as equilibrium current, current density fluctuations and filamentary structures. A Rogowski coil enables us to study various tokamak physics.

Contents

List of Figures

List of Tables

Chapter 1

Introduction

1.1 Nuclear fusion

Nuclear fusion is considered to be a promising candidate for energy source for the future because of its high degree of safety and benign environmental impact. Among numerous fusion reactions, the DT (deuterium-tritium) reaction (see Fig. 1.1) is the most effective reaction [1]. Both deuterium and lithium (used to produce tritium) are virtually inexhaustible on the earth. Thus, fusion power is very attractive for providing the base-load power for the long-range future.

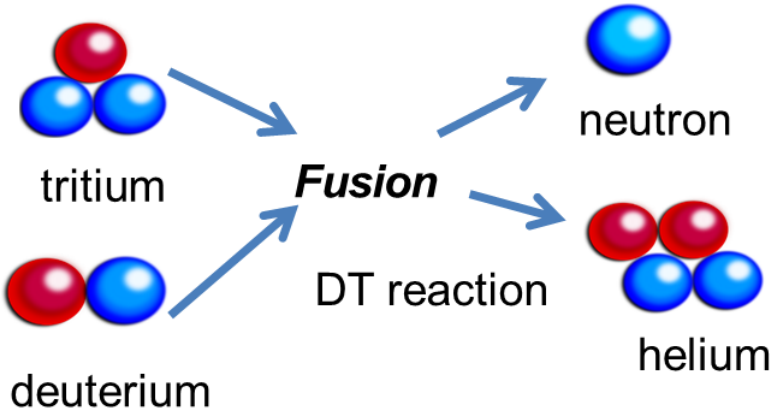

Fig. 1.1: DT reaction.

In order to realize fusion reactions on the earth, we need to generate a high temperature and high density plasma. Plasma is an ionized gas, and can be generated by supplying sufficient energy to the neutral gas. Sometimes, the plasma is called 'the fourth state of matter' [2]. In the plasma state, charged particles such as ions and electrons collide with each other. When the plasma is heated to high enough temperatures for the ions to approach close enough to each other, the nuclear fusion reaction can occur. Although, the fusion reactor has inherent safety since runaway reactions cannot occur, unlike fission reactors, there are many technical difficulties to generate plasmas with sufficiently high temperature and density, and confine the energy for a sufficiently long period of time. Therefore, it is critically important to study the physics of plasma confinement.

1.2 Tokamak and spherical tokamak

Presently, the tokamak is the most successful plasma confinement configuration. The tokamak is a toroidal magnetic confinement device with toroidal symmetry. ITER (International Thermonuclear Experimental Reactor), which is being constructed to study fusion burning plasmas, is a tokamak device [3]. A schematic configuration of the tokamak is shown in Fig. 1.2.

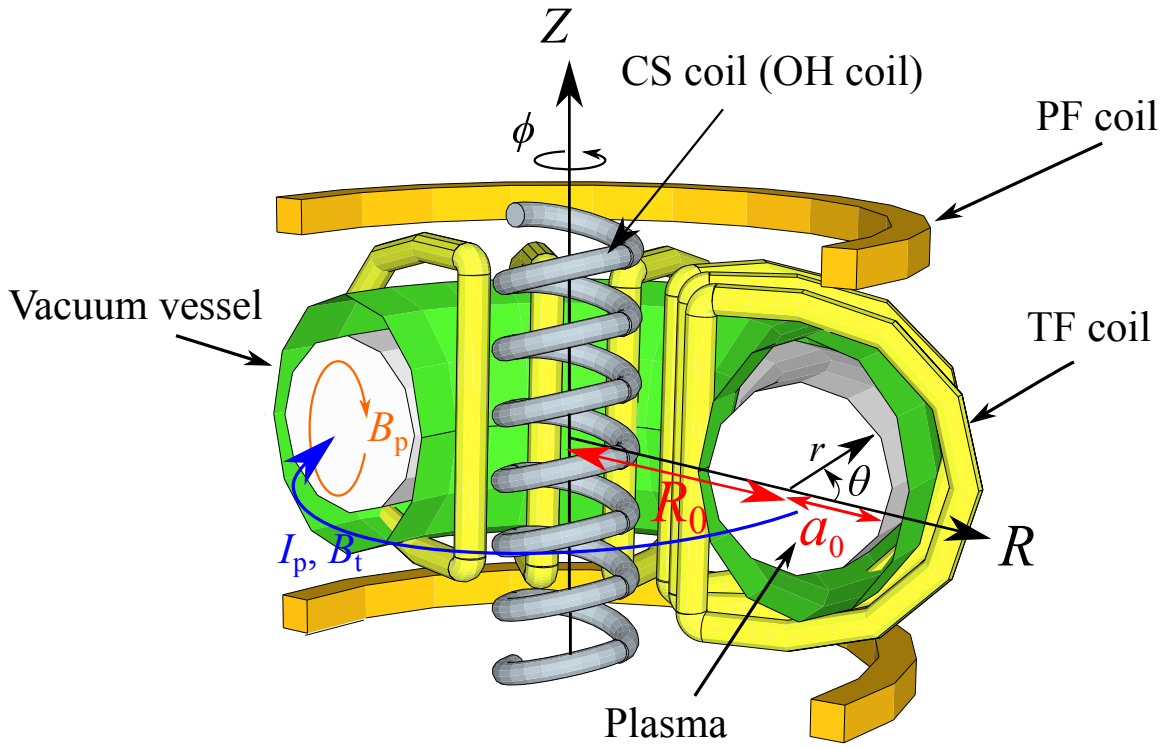

Fig. 1.2: Schematic configuration of the tokamak with several important quantities. I_p : plasma current, R_0 : major radius, a_0 : minor radius, ϕ : toroidal angle, θ : poloidal angle, B_t : toroidal magnetic field, B_p : poloidal magnetic field.

A tokamak device consists of a vacuum vessel, toroidal field (TF) coils, poloidal field (PF) coils, and the central solenoid (CS) or OH (Ohmic heating) coil. These coils play important roles in plasma confinement. B_t is the magnetic field produced by the TF coil current and B_p is the magnetic field produced by the plasma current I_p and the PF coil currents. The PF coils are used for controlling the plasma shape and position. In the tokamak, the plasma is confined by controlling these magnetic fields. The CS is used for inductive current drive and Ohmic plasma heating. As will be described later, minimizing or eliminating the CS is required to realize an attractive commercial fusion reactor.

In magnetically confined plasmas, charged particles gyrate and travel along magnetic field lines. This gyration is called the Larmor motion (Fig. 1.3). In tokamak plasmas, electrons and ions travel mainly in the toroidal direction (along the torus). If there is no I_p in the toroidal direction, charge separation occurs in the vertical (Z) direction (Fig. 1.2), and charged particles escape in the major radial direction by the $E \times B$ drift (Fig. 1.4) [1, 2]. When I_p is finite, B_p provides a short circuit path for electrons and ions in the poloidal

direction, and the plasma can be confined. Thus, driving the plasma current is essential for the tokamak.

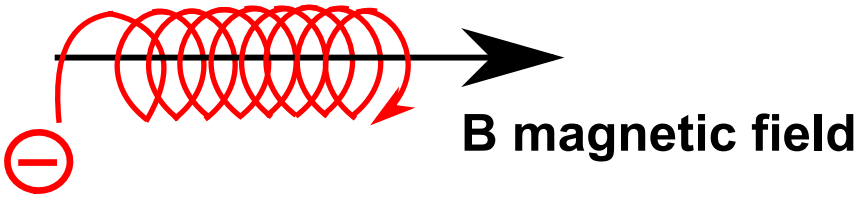

Fig. 1.3: Larmor motion.

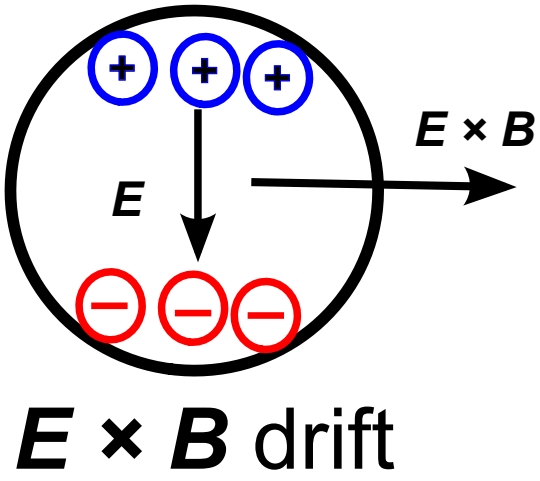

Fig. 1.4: $E \times B$ drift.

As a commercial fusion reactor, a tokamak device with a weak magnetic field strength and a high plasma pressure is desired since the cost of a tokamak device depends strongly on the magnetic field strength and the mass of the electromagnetic support structure. The β value

$$\beta = \frac{2\mu_0 < p >}{B_{t0}^2} \tag{1.1}$$

is used to characterize plasma stability. Here, μ_0 is the magnetic permeability in vacuum, $< p >$ is the volume averaged plasma pressure, and B_{t0} is the toroidal magnetic field strength at major radius $R = R_0$. In previous studies, it was demonstrated that the stability limit for β can be increased by controlling the plasma pressure profile, the current density profile, and the magnetic field configuration [4, 5].

The spherical tokamak, which can confine high pressure plasmas at a weak magnetic field strength (i.e., high β), was proposed by M. Peng [6]. A schematic comparison between the conventional tokamak and the spherical tokamak is shown in Fig. 1.5. In the spherical tokamak, the β limit is improved by reducing the aspect ratio A $(= R_0/a_0)$ and by optimizing the poloidal cross-sectional shape. Aspect ratios for a typical spherical tokamak and for a typical conventional tokamak are less than 1.5 and greater than 3, respectively. In order to realize an economically competitive fusion reactor, a reduction of the aspect ratio is effective,

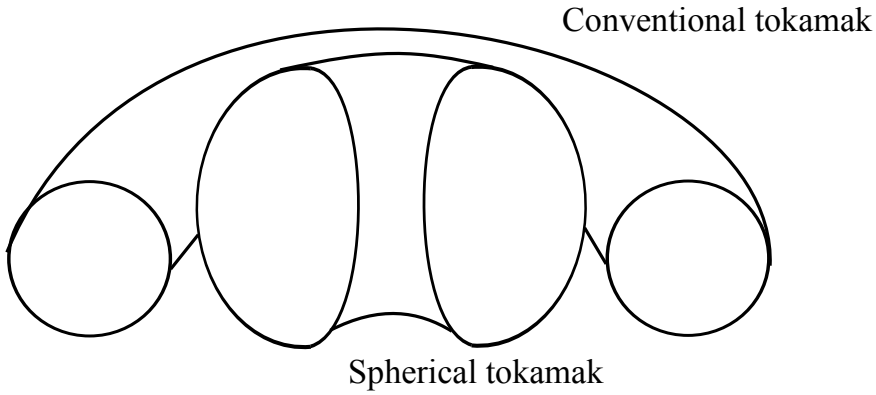

Fig. 1.5: Schematic comparison of the conventional tokamak and the spherical tokamak.

as shown by the VECTOR study [7]. Presently, JT60-SA is being constructed at JAEA (Japan Atomic Energy Agency). JT-60SA has an aspect ratio of $A = 2.5$ and its main mission is to explore improved stability of high β plasmas to indicate a favorable path toward a more efficient demonstration reactor (Demo) [8]. The Slim-CS Demo was designed with presently available technology, and adopted a reduced-size CS to reduce the reactor size and the construction cost [9]. In this device, the CS is used only for initial start-up and for plasma control. Therefore,an alternate method of plasma current ramp-up is required. For the design of a prototype fusion reactor, experimental data at small aspect ratios are quite important.

The Tokyo Spherical Tokamak-2 (TST-2, $R_0 \sim 0.38$ m, $a_0 \sim 0.25$ m, $B_\mathrm{t} \sim 0.3$ T, $I_\mathrm{p} \sim 0.1$ MA) is a spherical tokamak device at the University of Tokyo Kashiwa Campus [10]. A photograph of TST-2 is shown in Fig. 1.6.

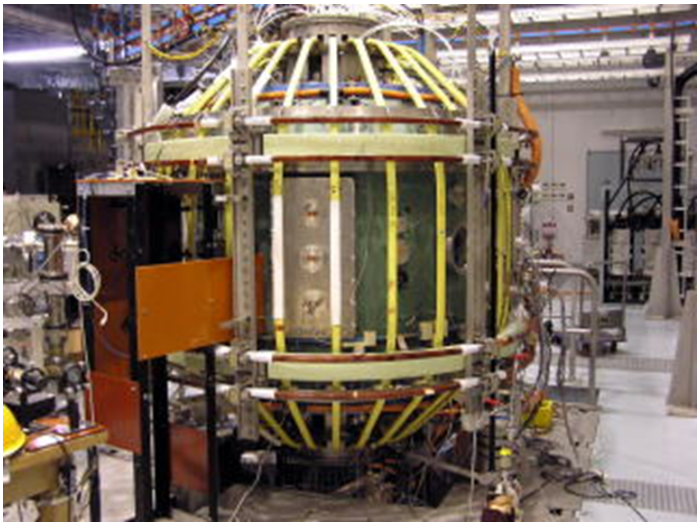

Fig. 1.6: The TST-2 spherical tokamak.

1.2.1 Tokamak plasma equilibrium

For stable fusion reactor operation, we need to develop effective methods to control the tokamak plasma. The determination of tokamak plasma equilibrium is an important issue. The plasma equilibrium is determined by the force balance between the pressure gradient force and the electromagnetic force. The plasma shape and position are controlled by external coil currents [11]. The tokamak equilibrium is usually considered to be toroidally symmetric, and the magnetic field lines lie on nested toroidal magnetic surfaces as shown in Fig. 1.7. In

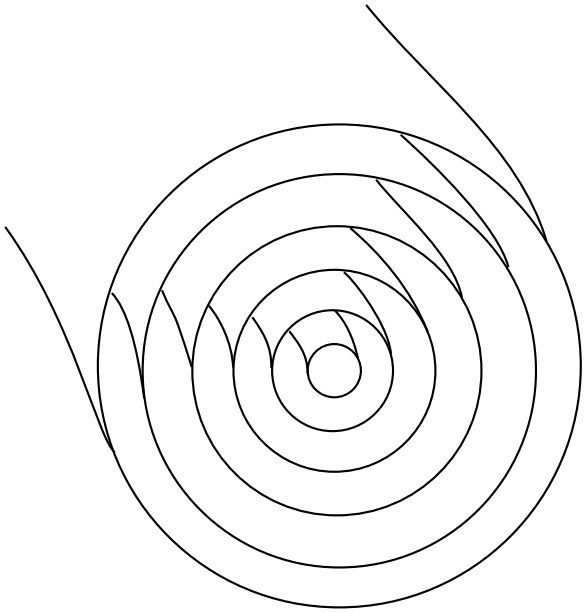

Fig. 1.7: Magnetic surfaces in a tokamak.

general, the force balance equation is expressed as

$$\boldsymbol{\nabla} p = \boldsymbol{j} \times \boldsymbol{B}, \tag{1.2}$$

where p is the plasma kinetic pressure, $\boldsymbol{j}$ is the plasma current density and $\boldsymbol{B}$ is the magnetic field. It is clear from Eq. (1.2) that $\boldsymbol{B} \cdot \boldsymbol{\nabla} p = 0$ and $\boldsymbol{j} \cdot \boldsymbol{\nabla} p = 0$. Thus, in an equilibrium state, there is no pressure gradient on the magnetic surface (on which the poloidal flux $\psi(\boldsymbol{r})$ is constant), and the current flows on the magnetic surface. Since $\psi(\boldsymbol{r})$ varies in the direction perpendicular to the flux surface,

$$\boldsymbol{B} \cdot \nabla \psi(\boldsymbol{r}) = 0. \tag{1.3}$$

In a toroidally symmetric system, a magnetic surface corresponds to a surface on which the poloidal flux is constant, and can be expressed by the vector potential as $\psi = RA_\phi(R, Z)$ [12]. From this equation, it is clear that the R and Z components of the magnetic field are given by

$$RB_R = \frac{\partial \psi}{\partial Z}, \qquad RB_Z = \frac{\partial \psi}{\partial R}. \tag{1.4}$$

In addition, from $\boldsymbol{B} \cdot \boldsymbol{\nabla} p = 0$, p and ψ should satisfy the equations:

$$-\frac{\partial \psi}{\partial Z}\frac{\partial p}{\partial R} + \frac{\partial p}{\partial Z}\frac{\partial (RB_\phi)}{\partial R} = 0, \tag{1.5}$$

$$p = p(\psi). \tag{1.6}$$

Thus, in equilibrium, the plasma pressure p is a function of ψ. Similarly, from $\boldsymbol{j} \cdot \boldsymbol{\nabla} p = 0$ and $\mu_0 j = \boldsymbol{\nabla} \times B$, B_ϕ and p should satisfy the equation

$$-\frac{\partial p}{\partial R}\frac{(RB_\phi)}{\partial Z} + \frac{\partial p}{\partial Z}\frac{\partial (RB_\phi)}{\partial R} = 0. \tag{1.7}$$

This equation shows that RB_ϕ is also a function of ψ. The relationship between RB_ϕ and ψ is written as

$$RB_\phi = \frac{\mu_0 I(\psi)}{2\pi}, \tag{1.8}$$

where R is an arbitrary radius, B_ϕ is the magnetic field at R, and $I(\psi)$ is the current flowing in the poloidal direction through hole of the torus defined by the poloidal flux surface $\psi = RA_\phi$. The R components of Eq. (1.2) can be written as

$$L(\psi) + \mu_0 R^2 \frac{\partial p(\psi)}{\partial \psi} + \frac{\mu_0^2}{8\pi^2}\frac{\partial I^2(\psi)}{\partial \psi} = 0, \tag{1.9}$$

$$L(\psi) = \left(R\frac{\partial}{\partial R}\frac{1}{R}\frac{\partial}{\partial R} + \frac{\partial^2}{\partial Z^2} \right)\psi. \tag{1.10}$$

This is the Grad-Shafranov equation [11,13,14] which describes equilibrium in axisymmetric configurations. The current density can be obtained as

$$j_\phi = -\frac{L(\psi)}{\mu_0 R}, \qquad j_{\mathrm{R}} = \frac{-1}{2\pi R}\frac{\partial I(\psi)}{\partial Z}, \qquad j_{\mathrm{Z}} = \frac{1}{2\pi R}\frac{\partial I(\psi)}{\partial R}. \tag{1.11}$$

1.2.2 Plasma heating

As explained in Sec. 1.2, I_{p} must be driven to form the tokamak configuration. A large current is applied to the CS (or OH coil) which is located at the center of the tokamak (see Fig. 1.2). When the current in the CS changes, a toroidal electric field is induced ($\boldsymbol{\nabla} \times \boldsymbol{E} = -\partial \boldsymbol{B}/\partial t$) and a toroidal plasma current is driven. This is shown schematically in Fig. 1.8. Since the plasma has a finite resistivity, the plasma is heated by Ohmic heating. Using the plasma resistivity η and the plasma current density j, the Ohmic heating power density P is written as

$$P = \eta j^2. \tag{1.12}$$

Although Ohmic heating is very effective in low temperature plasmas, it becomes ineffective in high temperature plasmas with low resistivity (because the plasma resistivity is proportional to $T_{\mathrm{e}}^{-\frac{3}{2}}$).

Magnetically confined charged particles gyrate at the cyclotron frequency ω_{c} which is proportional to the magnetic field strength. When an electromagnetic wave with the frequency ω_{ce} (electron cyclotron frequency) is injected into the plasma, electrons resonate with the wave and can absorb energy. The electron cyclotron frequency is

$$\omega_{\mathrm{ce}} = \frac{eB}{m_{\mathrm{e}}}, \tag{1.13}$$

where e is the magnitude of the electronic charge, B is the magnetic field strength, and m_{e} is the electronic mass.

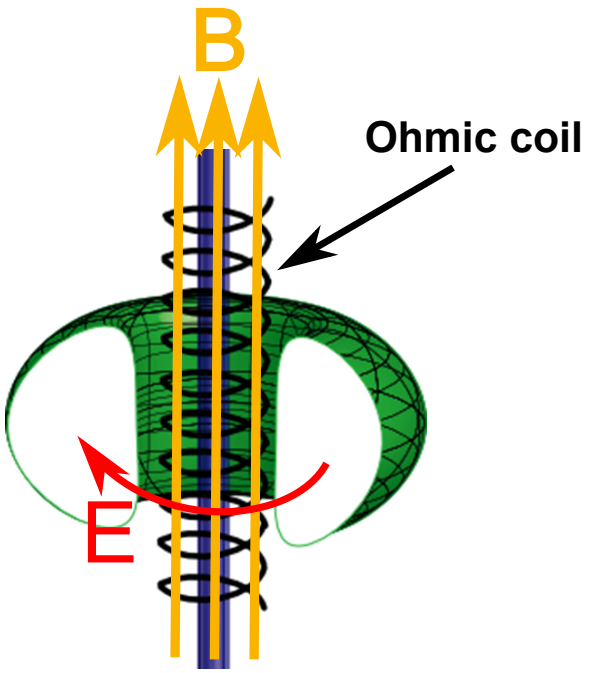

Fig. 1.8: Principle of Ohmic current drive.

1.3 Plasma sheath

When a solid material is placed inside the plasma, electrons and ions will flow to the material surface. Since the electron thermal velocity is much larger than the ion thermal velocity due to the large discrepancy in their masses, electrons reach the surface faster than ions, and accumulate near the surface. In order to limit the electron flow, the electrostatic potential of the material surface becomes negative and a large electric field is formed. Ions are accelerated towards the surface and electrons are repelled. Thus, quasi-neutrality is violated near the material surface. Such a region is called the plasma sheath. The Debye length λ_d is used to characterize the sheath thickness and is given by

$$\lambda_\mathrm{d} = \left(\frac{\varepsilon_0 T_\mathrm{e}}{n_\mathrm{e} e^2} \right)^{\frac{1}{2}}, \tag{1.14}$$

where ε_0 is the electrical permittivity in vacuum, T_e is the electron temperature and n_e is the electron density. In this thesis the temperature is measured in eV, and other parameters are measured in SI units. In order to form a stable plasma sheath, the sheath thickness varies according to circumstances.

Basically, stable formation of the plasma sheath requires that the drift velocity of ions at the the sheath entrance must be greater than the ion sound velocity $C_\mathrm{s} = \sqrt{T_\mathrm{e}/m_\mathrm{i}}$, where m_i is the ion mass. This condition is the Bohm criterion. Thus, there must be a region for ions to be accelerated up to or greater than C_s before entering the sheath. As shown in Fig. 1.9, we can separate the plasma sheath into two regions: the Debye sheath region with a characteristic length several times λ_d, and the presheath region with a characteristic length L_pre. These two regions must be connected smoothly, and there are various views. For simplicity, we present a basic calculation for the Debye sheath region in an unmagnetized plasma.

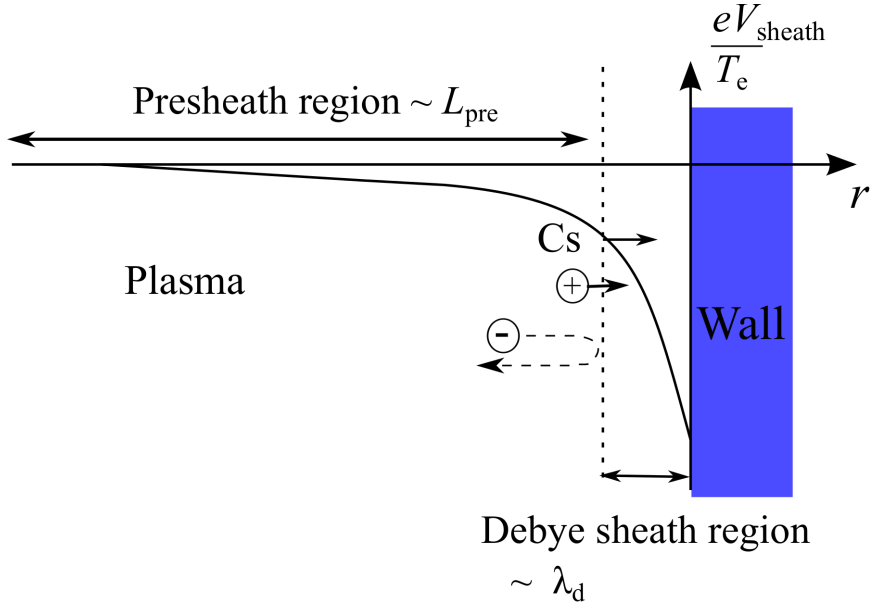

Fig. 1.9: Schematic of the plasma sheath. L_{pre} is the characteristic length of the presheath region and V_{sheath} is the surface potential.

Generally, the mean free path for thermal electrons is larger than λ_d, and the plasma is collisionless in the Debye sheath region. Thus, electrons can be assumed to satisfy the Boltzmann relationship. In order to calculate the Debye sheath potential, the following dimensionless quantities are defined [15]

$$y = \frac{m_i v_z^2}{2T_e}, \quad \chi = -\frac{eV_{\text{sheath}}}{T_e}, \quad n_{\text{norm, e,i}} = \frac{n_{e,i}}{n_0}, \quad \xi = \frac{z}{\lambda_d}, \tag{1.15}$$

where $m_i v_z^2/2T_e$ and $-eV_{\text{sheath}}/T_e$ are kinetic and potential energies of a singly charged ion normalized by the electron temperature, $n_{e,i}$ are the electron and ion densities in the Debye sheath, n_0 is the plasma density at the entrance to the Debye sheath, z is the spatial coordinate perpendicular to the material surface defined in Fig. 1.9, and ξ is the spatial coordinate normalized by the Debye length λ_d. In order to calculate the sheath potential, Poisson's equation must be solved, and we need to know the equations for electron and ion densities in the Debye sheath. As described above, the electron density is assumed to be in Boltzmann equilibrium, and the ion density can be calculated using the ion continuity equation and ion energy conservation. Thus, the Debye sheath is described by the following equations:

$$\frac{d^2\chi}{d\xi^2} = n_{\text{norm, i}} - n_{\text{norm, e}} \quad \text{Poisson}'\text{s equation,} \tag{1.16}$$

$$n_{\text{norm, e}} = \exp(-\chi) \quad \text{electron Boltzmann relation,} \tag{1.17}$$

$$n_{\text{norm, i}} y^{\frac{1}{2}} = {y_0}^{\frac{1}{2}} \quad \text{ion continuity,} \tag{1.18}$$

$$y = y_0 + \chi \quad \text{ion energy conservation,} \tag{1.19}$$

where y_0 is the normalized ion kinetic energy at the entrance to the Debye sheath. From the ion continuity equation and ion energy conservation, the ion density is given by $n_{\text{norm, i}} =$

$(1+\chi/y_0)^{-\frac{1}{2}}$. By multiplying Poisson's equation by $d\chi/d\xi$ and assuming that $d\chi/d\xi$ and χ approach 0 for $\xi \to 0$, we can obtain the normalized electric field (i.e., $d\chi/d\xi$) as

$$\left(\frac{d\chi}{d\xi}\right)^2 = 4y_0[(1+\chi/y_0)^{\frac{1}{2}} - 1] + 2(\exp(-\chi) - 1). \tag{1.20}$$

By integrating this equation numerically, the sheath potential in the Debye sheath can be calculated. Examples of calculation are shown in Fig. 1.10. From these figures, it is clear that the characteristic length for the Debye sheath is larger than λ_d and the ion density is larger than the electron density inside the Debye sheath. For small y_0, the solution of Poisson's equation diverges and y_0 must be greater than 0.5. This is the Bohm criterion and the details are discussed in Ref. [15]. While the plasma sheath has been studied since the 1920 ' s, the physics of plasma sheath is still unsolved. In addition, the sheath can present a problem for the interaction between the plasma and the plasma facing component [16]. Thus, it is still a very important subject for investigation.

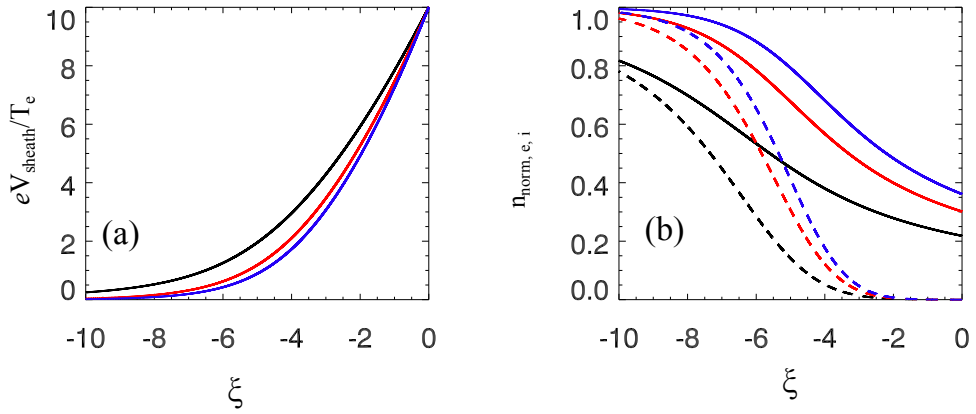

Fig. 1.10: Calculation results for the potential (a) and density (b) inside the Debye sheath. Black, red and blue lines are for $y_0 = 0.5$, 1 and 1.5. Solid curves and dashed curves in (b) are the ion and electron densities, respectively.

1.4 Magnetic reconnection and internal reconnection event in spherical tokamaks

1.4.1 Magnetic reconnection

Magnetic reconnection is a well-known phenomenon in which anti-parallel magnetic field lines in a plasma reconnect to form a different magnetic topology. It is frequently observed in the nature and in fusion plasmas. Magnetic reconnection cannot occur in a plasma with no resistivity, since the magnetic field lines are frozen in the plasma and must move together. The generalized Ohm's law is

$$\eta \boldsymbol{j} = \boldsymbol{E} + \boldsymbol{V} \times \boldsymbol{B}, \tag{1.21}$$

where η is the plasma resistivity. Using Eq. 1.21 and Ampere's law, the time derivative of the magnetic field is given by

$$\frac{\partial \boldsymbol{B}}{\partial t} = \boldsymbol{\nabla} \times (\boldsymbol{V} \times \boldsymbol{B}) + \frac{\eta}{\mu_0} \boldsymbol{\nabla}^2 \boldsymbol{B}. \tag{1.22}$$

The first and second terms on the right hand side of this equation describe convection and diffusion of the magnetic field. If the plasma has no resistivity, the second term is 0, and this equation describes the movement of the magnetic field with the plasma (frozen-in condition). When η is finite, the magnetic field can diffuse relative to the plasma. In such a case, magnetic reconnection can occur. A schematic of magnetic reconnection is shown in Fig. 1.11 When

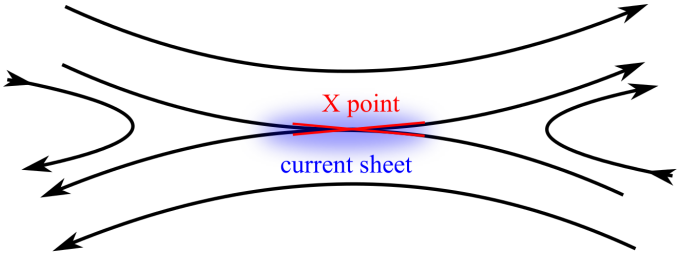

Fig. 1.11: Magnetic reconnection.

the antiparallel magnetic field lines approach each other, a localized current sheet forms at the X point. After reconnection, the straightening of the magnetic field lines take the plasma with them and particles are accelerated. When magnetic reconnection occurs, a part of the magnetic energy is converted to the plasma kinetic energy.

1.4.2 Internal reconnection event (IRE) in TST-2

The internal reconnection event (IRE) is an MHD energy relaxation phenomenon often observed in spherical tokamaks. It accompanies a transient increase of the total plasma current (positive I_p spike) caused by sudden reductions of the plasma thermal energy and magnetic energy. The latter is expressed by a reduction of the internal inductance which corresponds to the flattening of the current density profile [17]. Since a large fraction of the stored energy can be lost due to an IRE, it is an urgent issue to understand and control it. IRE is considered to occur when the pressure gradient exceeds a threshold value. IRE is observed and studied in TST-2 [18–20] and in other spherical tokamaks [21–23].

In Ref. [18], increases of the ion temperature T_i at three different spatial regions corresponding to emission regions of $\mathrm{C^V}$, $\mathrm{C^{III}}$ and $\mathrm{O^V}$ lines are observed during an IRE (see Fig. 5 in [18]). In this figure, time evolutions of I_p, impurity line intensities ($\mathrm{C^V}$ at $Z = 0$, -0.2 m, $\mathrm{C^{III}}$ at $Z = -0.2$ m and $\mathrm{O^V}$ at $Z = -0.2$ m), and ion temperatures obtained from Doppler broadening of these lines are plotted. Data shown in this figure were obtained in four different plasma discharges with similar I_p traces. ΔI_p defined in Fig. 5 in Ref. [18] is a good indicator of the strength of IRE. The four shots selected have the same ΔI_p. T_i increased up to ~ 400 eV ($\mathrm{C^V}$ at $Z = 0$, -0.2 m and $\mathrm{O^V}$ at $Z = -0.2$ m). For $\mathrm{C^{III}}$ at $Z = -0.2$ m, the increase of T_i starts earlier than others, but the increment is much smaller. During the period indicated by the arrow in Fig. 5(b) in Ref. [18], the intensities of $\mathrm{C^V}$ at $Z = 0$ m and -0.2 m are constant in time suggesting that the profile of $\mathrm{C^V}$ line emission intensity became flatter and that T_i obtained from $\mathrm{C^V}$ represents the ion temperature over a broad region. For $\Delta t \geq 0.2$ ms, the $\mathrm{C^V}$ intensity at $Z = 0.2$ m decreases and the intensity profile became peaked again. Thus, the decay of the $\mathrm{C^V}$ intensity at $Z = 0$ m reflects the core information.

In Refs. [19, 20], pick-up coils and a tangential pin-hole camera with a 20-channel PIN-diode array were used to measure magnetic fluctuations and the radial SXR (soft X-ray radiation) profile during IREs in TST-2 Ohmic plasmas. Figure 4 in Ref. [19] shows time

evolutions of the frequency spectra of magnetic fluctuations measured by pick-up coils located at $R = 0.49$, 0.51, 0.53 m, and in the shadow of the outboard limiter, $I_{\rm p}$ and the loop voltage. A growth of 10 kHz magnetic fluctuations ($R \leq 0.51$ m) accompanied by a growth of up to the 4th harmonic are shown. In addition, a 10 kHz mode appears behind the limiter. Just before the drop of the loop voltage, stabilization of harmonics and a growth of mode at 15 kHz and 30 kHz are also observed. From these results, we can infer that some non-linear processes are involved in MHD instabilities which cause the IRE.

Figure 4 in Ref. [20] shows a typical time trace during an IRE in a TST-2 Ohmic plasma discharge. The time traces of the SXR camera shows an inward shift of the plasma. The increase of $I_{\rm p}$ starts from 21.3 ms, and magnetic fluctuations with mode numbers $n = 1$ (10 kHz) and 2 (20 kHz) grow. A rapid increase of H_α line emission indicate hydrogen recycling from the vacuum vessel wall. The SXR profile shows a collapse at $t = 21.35$ ms, and the particles are expelled from the plasma core region. After that, the SXR signal propagates towards outside of the plasma.

1.4.3 Non-linear simulations of IRE

Theree-dimensional MHD simulations in toroidal geometry were performed and several key features of IRE have been revealed by H. Hayashi and N. Mizuguchi [24, 25]. The boundary of the computational region is a perfectly conducting wall. The following full set of resistive and compressible MHD equations were used for the simulation:

$$\frac{\partial \rho}{\partial t} = -\boldsymbol{\nabla} \cdot (\rho \boldsymbol{v}), \tag{1.23}$$

$$\frac{\partial}{\partial t}(\rho \boldsymbol{v}) = -\boldsymbol{\nabla} \cdot (\rho \boldsymbol{v}\boldsymbol{v}) - \boldsymbol{\nabla} p + \boldsymbol{j} \times \boldsymbol{B} + \mu \left[\boldsymbol{\nabla}^2 \boldsymbol{v} + \left(\frac{1}{3} \boldsymbol{\nabla} (\boldsymbol{\nabla} \cdot \boldsymbol{v}) \right) \right], \tag{1.24}$$

$$\frac{\partial \boldsymbol{B}}{\partial t} = -\boldsymbol{\nabla} \times \boldsymbol{E}, \tag{1.25}$$

$$\frac{\partial p}{\partial t} = -\boldsymbol{\nabla} \cdot (p \boldsymbol{v}) - (\gamma - 1) p \nabla \cdot \boldsymbol{v} + (\gamma - 1)(\eta \boldsymbol{j}^2 + \Phi - \boldsymbol{\nabla} \cdot \boldsymbol{q}), \tag{1.26}$$

$$\boldsymbol{j} = \boldsymbol{\nabla} \times \boldsymbol{B}, \tag{1.27}$$

$$\boldsymbol{E} = -\boldsymbol{v} \times \boldsymbol{B} + \eta \boldsymbol{j}, \tag{1.28}$$

$$\Phi = 2\mu \left(e_{ij} e_{ji} - \frac{1}{3} (\boldsymbol{\nabla} \cdot \boldsymbol{v})^2 \right), \tag{1.29}$$

$$e_{ij} e_{ji} = \frac{1}{2} \left(\frac{\partial v_i}{\partial x_j} + \frac{\partial v_j}{\partial x_i} \right), \tag{1.30}$$

$$\boldsymbol{q} = -\kappa \boldsymbol{\nabla}_{\parallel} (p/\rho). \tag{1.31}$$

Figure 3 in Ref. [24] shows the calculation result for the pressure profile during an IRE. Parameters used for the simulation were: aspect ratio $A = 1.35$, elongation $\kappa = 1.6$, central beta $\beta(0) = 48\%$, and the central safety factor $q(0) = 0.91$. As seen in Fig. 3 in Ref. [24], the plasma pressure in the central region falls on a timescale of $100\tau_{\rm A}$, and the thermal energy is transported from the core to the edge. $100\tau_{\rm A}$ roughly corresponds to 1μs.

Figure 6 in Ref. [24] shows the development of an isobaric surface of the plasma and magnetic field lines for the same calculation condition as Fig. 3 in Ref. [24]. It can be seen that the thermal energy is transported from the plasma core region to the plasma edge region by convection caused by the excited modes. This can be seen as the collapse of the plasma pressure profile. In addition, simulation results suggest that a current sheet structure is

formed in the region where the bulge-like perturbation grows. It is localized near the plasma edge and in the toroidal direction.

Figure 2 in Ref. [25] shows the overall plasma structure monitored by a CCD (charged couple device) camera in the START spherical tokamak [21]. Frame (a) was taken with a higher time resolution of 30μs, whereas frames (b)-(d) were taken with a time resolution of 100 μs). From Fig. 2(a) in Ref. [25], a helical structure, which is localized in a narrow region and in the toroidal direction is observed. These are very similar to the simulation result shown in Fig. 6 in Ref. [24]. In Fig. 2(b) in Ref. [25], a filamentary structure can still be seen. Overall distortions are observed in Figs. 2(c) and (d) in Ref. [25].

1.4.4 IRE in NSTX

In NSTX (National Spherical Torus Experiment) [26], IREs were also studied using 3 sets of SXR detectors (16 vertical and 16+16 horizontal channels) and pick-up coils (see Fig. 2 in Ref. [23]). Two types of IREs were studied, minor IRE and major IRE. The vertical array of detectors have sensitivities to both SXR and UV (ultraviolet), and the two horizontal arrays have sensitivity to only SXR. Typical plasma discharges with minor IRE and major IRE are shown in Fig. 1 in Ref. [23]. For the minor IRE case, $I_{\rm p}$ decreases moderately after the $I_{\rm p}$ spike. On the other hand, for the major IRE case, plasma disruption occurs at the same time as the $I_{\rm p}$ spike. In these two types of discharges, the time sequence of events was different.

An expanded view of SXR and magnetic signals for a minor IRE are shown in Fig. 3 in Ref. [23]. A sinusoidal oscillation can be seen on SXR and magnetic signals before the IRE. The toroidal mode number n and the poloidal mode number m are both 1. This precursor oscillation persists for 10 ms. From the horizontal and vertical arrays of SXR detectors, we can see that the precursor oscillation moves to a larger minor radius. After the oscillation slows down, the oscillation stops (mode locking). This condition lasts for about 2 ms, and then an internal crash occurs followed by peripheral UV radiation. This peripheral radiation is considered to be due to influx of impurities from the wall caused by highly energized electrons escaping from the plasma core.

Figure 5 in Ref. [23] shows the time sequence for a major IRE. In this case, a spontaneous development of the locked mode is seen (phase I). After 5 ms, the plasma collapses and the energy is transferred from the core region to the external region (phase II). The crash of the core SXR emission is caused by a flattening of the $T_{\rm e}$ profile, similar to the thermal quench in conventional tokamaks. In phase III, $I_{\rm p}$ starts to increase, then MHD activity in the edge region increases. The increase of $I_{\rm p}$ could be a consequence of the expansion of the current channel. As a result of central cooling, $I_{\rm p}$ falls. It is apparent that this current quench is caused by the vertical instability. During this period, Figs. 3 and 5 in Ref. [23] show that a hot region is formed in the cold plasma region with the center displaced downward and outward.

1.5 Plasma diagnostics in TST-2

1.5.1 Magnetic pick-up coil

The magnetic pick-up coil is a fundamental diagnostic for magnetic field. The principle of magnetic pick-up coil is based on electromagnetic induction. When a magnetic field $\boldsymbol{B}$ passing through the pick-up coil changes in time as shown in Fig. 1.12, an output voltage V is induced. The relationship between V and B is given by

$$V = SN\frac{\partial \boldsymbol{B}\cdot\boldsymbol{n}}{\partial t}, \tag{1.32}$$

where S is the cross sectional area of the pick-up coil, N is the number of turns, and $\boldsymbol{n}$ is the normal vector perpendicular to S as shown in Fig. 1.12. The pick-up coil measured the time derivative of the magnetic field, and by integrating the signal in time the magnetic field is obtained.

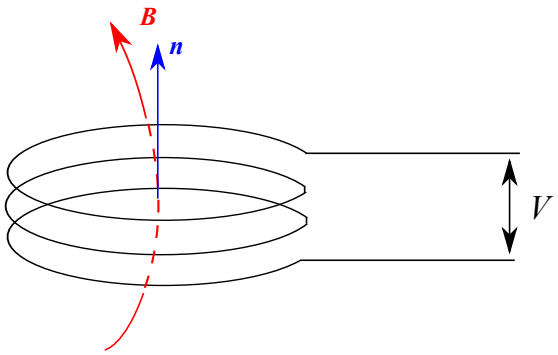

Fig. 1.12: Magnetic pick-up coil.

Pick-up coils are used to measure the spatial distribution of the magnetic field which is needed to calculate plasma equilibrium [27]. They can also measure MHD fluctuations, and toroidal and poloidal mode numbers (n and m) can be derived [28]. Dozens of pick-up coils are located inside the TST-2 vacuum vessel. Fig. 1.13 shows the locations of the pick-up coils in toroidal and poloidal cross sections of TST-2. Hereafter, we call pick-up coils in Fig. 1.13(a) and (b) as n coils and m coils, respectively.

1.5.2 Langmuir probe

Current-voltage characteristic

The Langmuir probe is a traditional plasma diagnostic developed by I. Langmuir in 1924 [29]. It can measure many plasma parameters. The Langmuir probe is a small electrode inserted into a plasma. When an electrode is located in a plasma, some ions and electrons enter the electrode. The magnitude of electric current flowing into the electrode due to such ions and electrons ($I_{\mathrm{electrode}}$) depends on the difference between the plasma potential (or space potential, V_{s}) and the electrode potential ($V_{\mathrm{electrode}}$). When $V_{\mathrm{electrode}}$ is sufficiently lower than V_{s}, $I_{\mathrm{electrode}}$ is dominated by ions, and is called the ion saturation current I_{is}. On the other hand, when $V_{\mathrm{electrode}}$ is larger than or equal to the plasma potential, $I_{\mathrm{electrode}}$ is dominated by electrons, and is called the electron saturation current I_{es}. When a voltage is applied to the electrode and varies in time, the relationship between $I_{\mathrm{electrode}}$ and $V_{\mathrm{electrode}}$ shows a characteristic shape (I-V curve). A schematic of the I-V curve is shown in Fig. 1.14 (red curve).

Typically, the I-V curve can be divided into three regions (Regions I, II and III), where the electron current is dominant, where both electrons and ions enter the electrode, and where the ion current is dominant. In Fig. 1.14, V_{f} is the floating potential, which is the potential when the ion and electron currents are balanced (i.e., $I_{\mathrm{electrode}} = 0$ A). When the target plasma to be measured has a Maxwellian velocity distribution, the electron temperature and

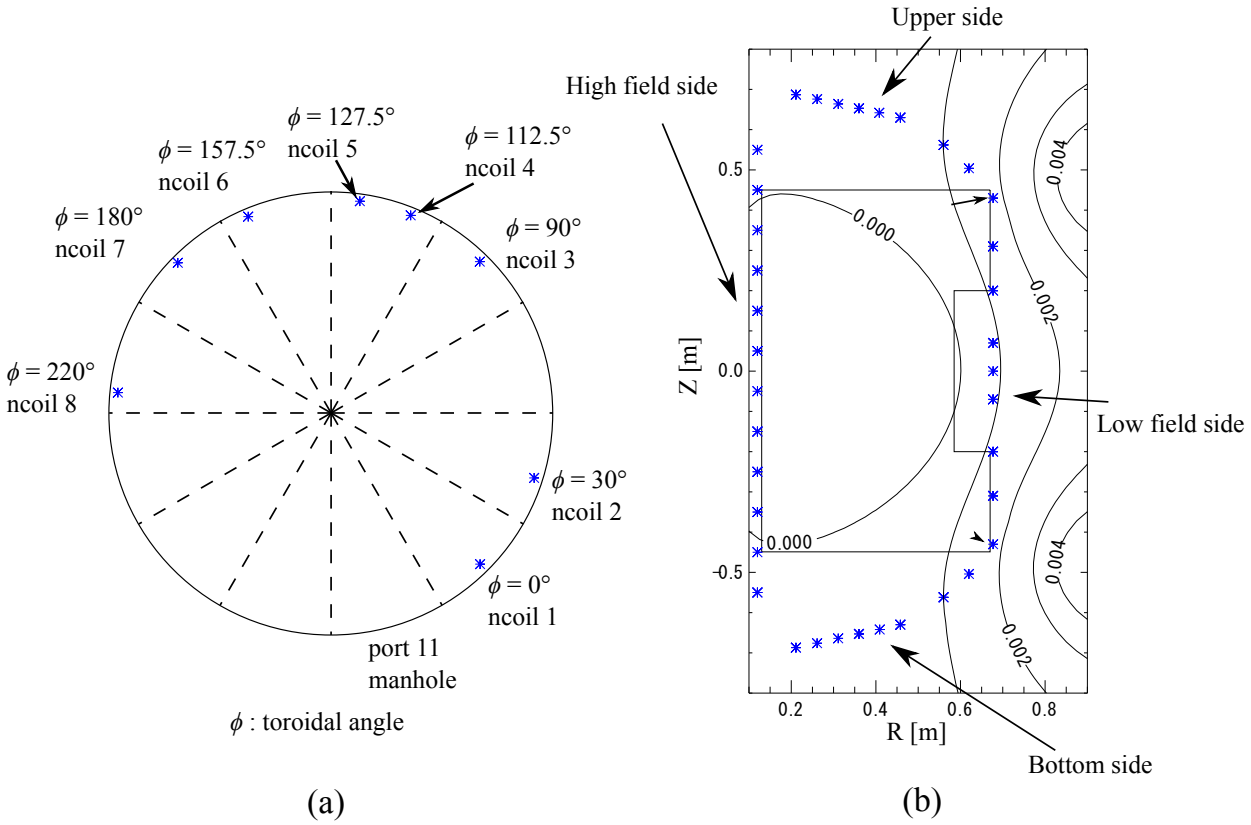

Fig. 1.13: Locations of magnetic pick-up coils inside the TST-2 vacuum vessel. (a) toroidal cross section viewed from the top, and (b) poloidal cross section. Blue symbols indicate the locations of pick-up coils.

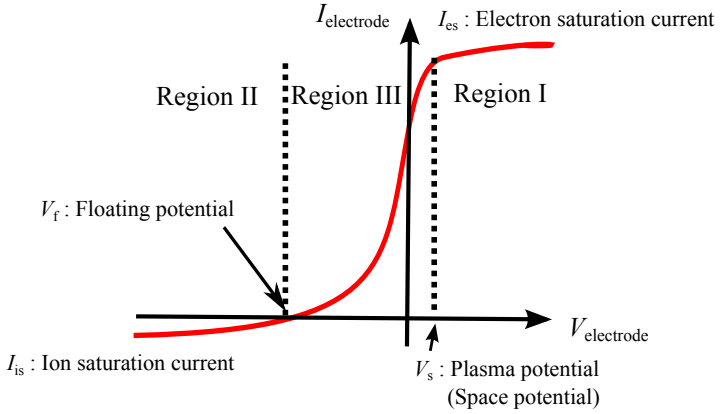

Fig. 1.14: Schematic of Langmuir probe I-V characteristic curve.

density can be estimated from the I-V curve. Since the shape of the I-V curve depends on the velocity distribution function, it can deviate from the typical shape for Maxwellian distribution. For example, when the velocity distribution is bi-Maxwellian, consisting of bulk electrons and energetic electrons, V_f becomes very negative, and the I-V curve shows a tail in Region III [30]. In such a case, typical I-V fitting assuming Maxwellian distribution cannot be used. In this section, we present a representative case of I-V curve fitting assuming a Maxwellian plasma.

Firstly, we give $I_\mathrm{electrode}$ for Regions I and II as

$$I_\mathrm{es} = \frac{1}{4} e n_\mathrm{e} S_\mathrm{electrode} \left(\frac{8 T_\mathrm{e}}{\pi m_\mathrm{e}} \right)^{\frac{1}{2}}, \tag{1.33}$$

$$I_\mathrm{is} = \exp\left(-\frac{1}{2}\right) e n_\mathrm{e} S_\mathrm{electrode} \left(\frac{T_\mathrm{e}}{m_\mathrm{i}} \right)^{\frac{1}{2}}, \tag{1.34}$$

where $S_\mathrm{electrode}$ is the surface area of the electrode exposed to the plasma. Here, I_es and I_is are given as constants, but in reality, there are weak dependences on $V_\mathrm{electrode}$ depending on the measurement condition such as the size of the electrode. In Region III, $I_\mathrm{electrode}$ increases exponentially with $V_\mathrm{electrode}$ if the electron velocity distribution is Maxwellian (see Fig. 1.14). The electron current I_e is given by

$$I_\mathrm{e} = I_\mathrm{es} \exp\left(\frac{V_\mathrm{electrode} - V_\mathrm{s}}{T_\mathrm{e}} \right). \tag{1.35}$$

By taking the logarithm of Eq. (1.35), T_e can be estimated from its slope, and n_e can be estimated using T_e and Eq. (1.34). In principle, n_e can also be estimated using Eq. (1.33), but this is quite difficult since I_es can be distorted easily by a variety of factors such as plasma fluctuations and electron Larmor motion. From Eqs. (1.33) and (1.34), the plasma potential is given by

$$V_\mathrm{s} = V_\mathrm{f} + \frac{T_\mathrm{e}}{e} \log\left(\frac{m_\mathrm{i}}{2\pi m_\mathrm{e}} \right). \tag{1.36}$$

In actual experiments, there are difficulties in estimating T_e and n_e precisely. In the following subsection, we present a method and examples of I-V curve fitting for data obtained in TST-2 Ohmic plasmas.

Examples of I-V curve fitting

A schematic of the circuit used for Langumuir probe measurement in TST-2 is shown in Fig. 1.15. In TST-2, a coaxial cable is used for Langmuir probe measurement. The outer conductor of the coaxial cable and the circuit ground is connected to the tokamak ground. The current is measured by the voltage drop across the resistance R in the circuit (see Fig. 1.15).

A typical example of the measured $I_\mathrm{electrode}$ data is shown in Fig. 1.16. In this experiment, a sine wave voltage at 100 kHz was applied to the electrode. The measured signal is distorted due to the capacitance between the center and outer conductors of the coaxial cable. The sine wave in Fig. 1.16(c) and the asymmetry of the raw data in Fig. 1.16(d) show this effect. The capacitance effect is determined by curve fitting to the raw $I_\mathrm{electrode}$ data in the absence of plasma (red curve in Fig. 1.16(c)). The capacitance effect determined this way is subtracted from the raw $I_\mathrm{electrode}$ data in the presence of plasma. By eliminating the capacitance effect, we can obtain a clearly symmetric I-V curve as shown by the blue curve in Fig. 1.16(d).

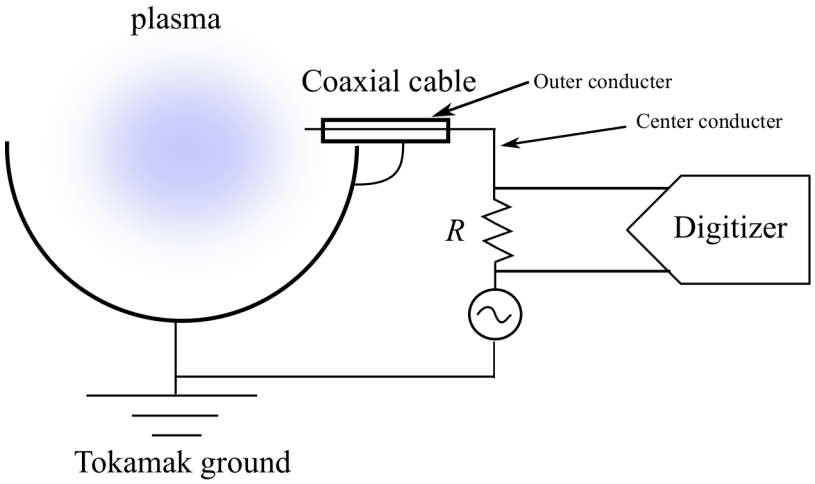

Fig. 1.15: Schematic of Langmuir probe measurement circuit used in TST-2.

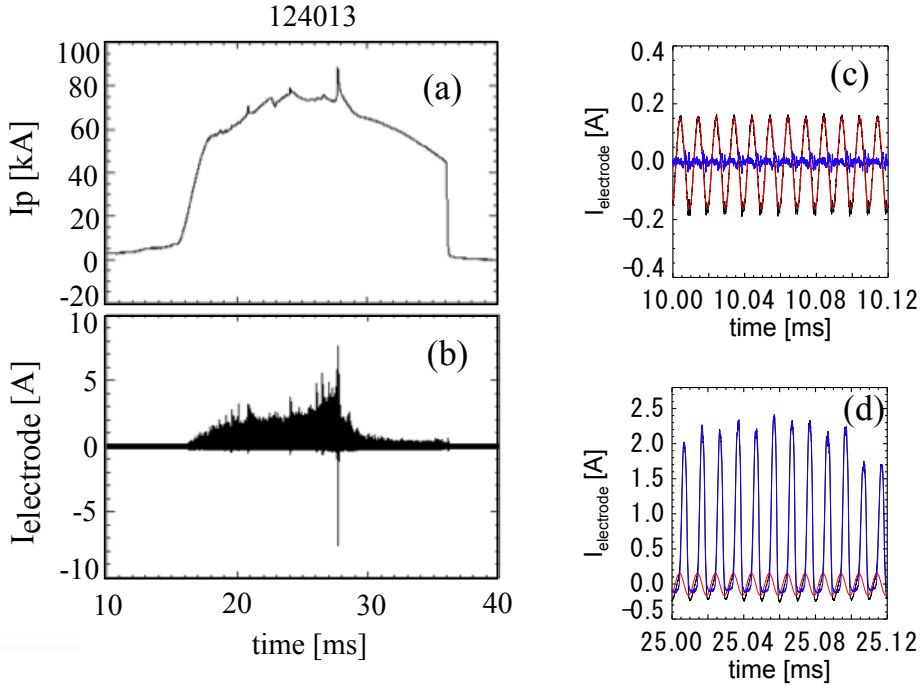

Fig. 1.16: Typical measured current flowing into the probe electrode. (a) I_{p}, (b) $I_{\mathrm{electrode}}$. (c) and (d) are enlarged views of (b) for two time intervals without and with plasma. Black, red and blue curves in (c) and (d) are the raw $I_{\mathrm{electrode}}$ data, fitted curve (capacitance effect) and the corrected $I_{\mathrm{electrode}}$ data with the capacitance effect subtracted.

For the estimation of T_e and n_e, I-V curve fitting must be performed precisely. The selection of a model function for fitting is important. In TST-2 Ohmic plasmas, the measured I_{is} shows a weak dependence on the applied voltage. The model function used in this thesis is

$$I_{electrode} = a_1 \exp\left(\frac{V_{electrode} - a_3}{a_2}\right) + a_4 V_{electrode} + a_5. \quad (1.37)$$

The dependence of I_{is} on $V_{electrode}$ is given by a linear function ($a_4 V_{electrode} + a_5$). a_2 corresponds to the electron temperature T_e. For I-V curve fitting, initial values for a_1, a_2, a_3 and a_4 should be determined. In order to estimate them, we need rough estimations of T_e and n_e.

Figure 1.17 shows a typical I-V curve and a semi-log plot of the I-V curve. The red line in Fig. 1.17(a) shows a linear fitting result for the ion saturation current, $a_4 V_{electrode} + a_5$ in Eq. (1.37). For the estimation of initial a_4 and a_5, certain regions of $V_{electrode}$ for linear fitting are tested, and we select the fitting results whose a_4 is greater than 0, and the smallest a_4 in the selected sets is chosen. The red line in Fig. 1.17(b) shows a linear fitting result where $V_{electrode}$ is above V_f. From the slope of the red curve, we can estimate T_e. In Eq. (1.37), a_3 corresponds to V_s. Since V_s is expected to be approximately $1.5T_e$, we set the initial a_3 to be 1.5 times the initial a_2 in this fitting.

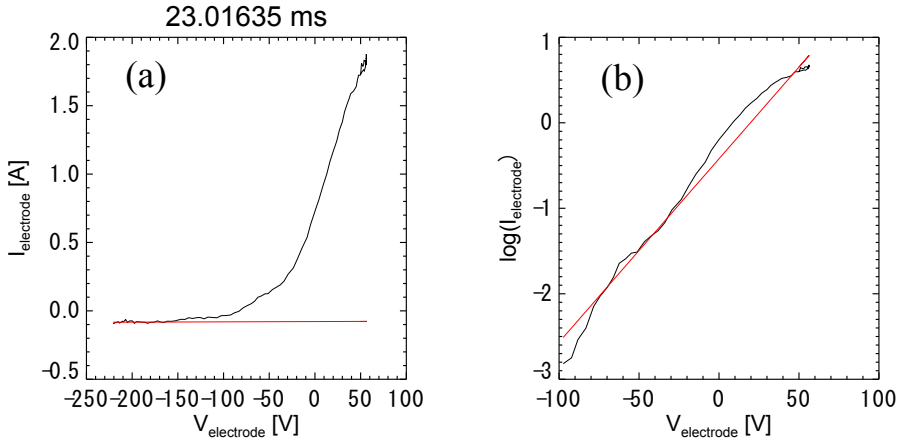

Fig. 1.17: Typical I-V curve (a) and a semi-log plot of the I-V curve (b). Red lines in (a) and (b) are linear fitting results for I_{is} and for $\log(I_{electrode})$, where $V_{electrode}$ is above V_f, respectively.

Initial values of a_1, a_2, a_3, a_4 and a_5 can be estimated as described above. Using these values, we perform a nonlinear fitting to the measured I-V curve. The fitting result depends strongly on the fitting region of $V_{electrode}$. In addition, a_1, a_3 and a_4 must be greater than 0. If the fitting region is not adequate, these values may become negative. In this fitting, 20 regions were tested, and we selected the results with a_1, a_3 and $a_4 \geq 0$. Figure 1.18 shows the fitting results for the I-V curve in Fig. 1.17. As described above, the fitting regions are different in each case (see the blue curves in Fig. 1.18). For precise estimation, the result with the smallest fitting error σT_e is chosen for the electron temperature. For the case of Fig. 1.18, (a) is adopted and n_e is estimated using I_{is} and T_e determined by fitting.

Thomson scattering (TS) is presently the most reliable T_e diagnostic. A TS system is used in TST-2 [31]. In order to verify T_e derivation from the I-V curve, a comparison between electron temperatures measured by TS and Langmuir probe was performed, as shown in Fig.

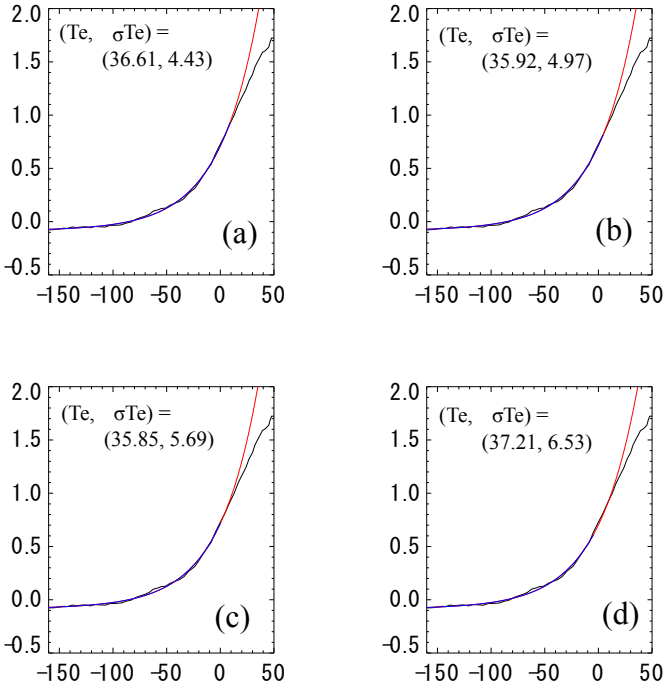

Fig. 1.18: Fitting results using the model of Eq. (1.37). Black curve: raw data, red and blue curves: fitted curves. Blue curve shows the fitting region. T_e and σT_e are the electron temperature and the fitting error for T_e.

1.19. The electron temperature was measured at the same radial location. We can see the agreement within the error bars of the measurements. This demonstrates the validity of T_e estimation by fitting to the I-V characteristic curve. In the following sections, the estimation of T_e from Langmuir probe measurement are performed by the fitting model described here.

1.5.3 Interferometer

A microwave interferometer is a standard diagnostic to measure the line-integrated electron density [32]. A schematic of a typical interferometer system is shown in Fig. 1.20. When a microwave beam passes through the plasma, the phase velocity differs from that in vacuum. In a microwave interferometer diagnostic, the line-integrated density can be measured from the phase difference between the wave which passes through the plasma and the wave which does not pass through the plasma (see Fig. 1.20). The phase shift of microwave φ when it passes through a plasma of thickness L in the x direction is given by

$$\varphi = \int_L k_\mathrm{p} dx = k_0 \int_L N dx, \tag{1.38}$$

where k_p is the wavenumber in the plasma, k_0 is the wavenumber in vacuum, and N is the refractive index of the plasma ($N^2 = 1 - (\omega_\mathrm{pe}/\omega)^2 = 1 - n_\mathrm{e}/n_\mathrm{c}$, where n_e and n_c are the electron density and the cut-off density). The phase difference between the two waves (passing through the plasma and passing through vacuum) is given by

$$\delta\varphi = k_0 \int_L (1 - N) dx. \tag{1.39}$$

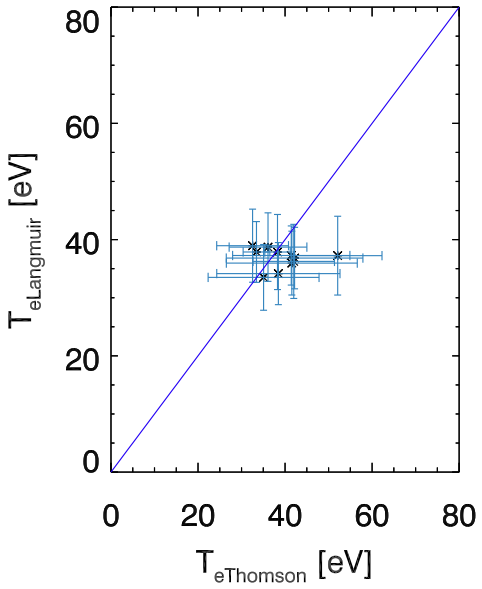

Fig. 1.19: Comparison between the electron temperatures measured by the Langmuir probe and by Thomson scattering (shots 119860-119873). Symbols: experimental data points, blue line: equality of $T_{\mathrm{eLangmuir}}$ and T_{eThomson}. $T_{\mathrm{eLangmuir}}$ was obtained by averaging T_{e} over 1 ms and the error bars of $T_{\mathrm{eLangmuir}}$ show the standard deviations in 1 ms. The error bars of T_{eThomson} show the fitting errors.

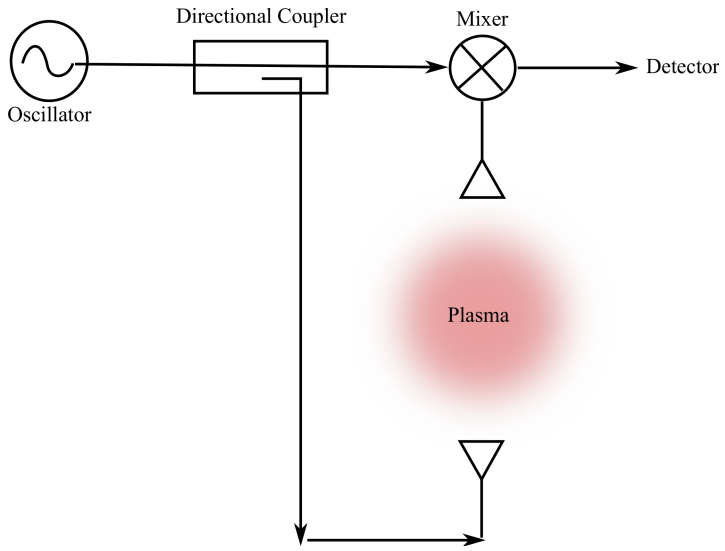

Fig. 1.20: Schematic of a typical interferometer system.

When $n_e \ll n_c$, N is approximately given by

$$N \approx 1 - \frac{1}{2}\left(\frac{n_e}{n_c}\right). \tag{1.40}$$

Using this equation, Eq. (1.39) can be rewritten as

$$\delta\varphi \cong \frac{k_0}{2n_c}\int_L n_e dx, \tag{1.41}$$

showing that the line-integrated density can be measured.

1.5.4 Fast visible-light camera

Fast visible-light cameras are frequently used to study plasmas, and its importance is growing with the development of technology. Plasmas emit visible light radiation through a variety of processes. Plasma boundary, plasma position and localized composition can be inferred from these emissions [33]. A fast visible-light camera is useful for the study of MHD equilibrium and instabilities [34]. In Ref. [35], a photograph of a high speed camera (MEMRECAM HX-3, NAC Image Technology. Inc.) used in the experiment in this thesis is shown.

The maximum frame rate of MEMRECAM HX-3 is 1,300,000 frames/s. Detailed specifications of MEMRECAM HX-3 can be found in [35]. Figure 7 in Ref. [36] shows recent results obtained in amagnetic reconnection experiment in the UTST spherical tokamak [37,38] using this camera. The stratified visible light emission before fast reconnection shows the current sheet. The photograph taken during the fast reconnection phase indicates emissive regions in the upper left and lower right regions, which are inferred to be due to energetic electrons localized along one pair of separatrix [36].

1.5.5 Radiation measurements

In TST-2 experiments, soft X-ray (wavelength $\sim 10^{-8}$ m) radiation from the plasma are measured using surface barrier diodes (SBDs) and photodiodes (AXUV-20EL, AXUV-16ELOHYB1, RAD Device Co., Ltd.). These are semi-conductor detectors. The electrical conductivity of a semi-conductor increases with temperature. When impurities are added to a semi-conductor, its property changes. Types of semi-conductors can be classified into p-type, n-type and p and n-type (p-type has missing electrons, n-type has extra electrons and p and n-type is electrically neutral). For the detection of X-rays, the depletion layer, which is a p-n junction in a semiconductor crystal, is used. When an X-ray photon hits the depletion layer, pairs of holes and electrons are produced and they move towards negative and positive electrodes. As a result, electrical current is created whose magnitude is proportional to the incident photon energy.

The energy regions which can be measured by SBD and AXUV detectors are different. The measurement of X-rays in different energy ranges can be performed by simultaneous measurements using different detectors with different filters.

1.6 Review of current density measurements

The current density profile has important roles in plasma equilibrium, momentum transport, magnetic reconnection and particle transport. Therefore, reliable measurements of the current density profile is quite important for understanding the physics of tokamak plasmas. In particular, the measurement of the edge current density profile in a spherical tokamak is important for the following reasons.

(1) Particle transport

The radial particle transport flux can be expressed as [39]

$$\Gamma_{r,e} = \frac{< \tilde{n}\tilde{E}_{\perp} >}{B} - \frac{< \tilde{j}_{\parallel,e}\tilde{B}_r >}{B}, \tag{1.42}$$

where $\Gamma_{r,e}$ is the radial electron flux, $\tilde{n}$ is the fluctuating density, $\tilde{E_{\perp}}$ is the fluctuating perpendicular electric field, $\tilde{j}_{\parallel,e}$ is the fluctuating parallel current density, $\tilde{B_r}$ is the fluctuating radial magnetic field and B is the static magnetic field strength. Since the particle transport is inversely proportional to B, transports in low toroidal field configuration such as the spherical tokamak and the reversed field pinch, can be larger than that in the conventional tokamak. In MST (Madison Symmetric Torus) reversed field pinch experiments, current density fluctuations were measured using multi-channel magnetic probes and an electrostatic analyzer [40, 41], and they have concluded that the current density fluctuations can affect transport. In addition, they have demonstrated that both fluctuations and transport can be suppressed by improving the current density profile [42]. In the HIST spherical tokamak, the toroidal current density profile and fluctuations were measured using 6 Rogowski coils arranged in the radial direction, and studied plasma equilibrium in plasmas produced by CHI (coaxial helicity injection) [43]. Although the HIST group has measured the current density profile, the large size of the Rogowski coil did not permit measurements of small-scale structures and fluctuations. For turbulence-driven particle transport study small-scale structures and fluctuations must be measured.

(2) H-mode physics

The low confinement mode (L-mode) and the high confinement mode (H-mode) are the two standard confinement regimes of tokamak operation. In the H-mode, high temperature and high β plasmas can be produced more easily, and it is considered to be a favorable operating mode for a fusion reactor [44, 45]. The H-mode operation has been accomplished in spherical tokamaks such as START, MAST, NSTX and Pegasus [46–49]. In H mode plasmas, an MHD instability called the ELM (Edge localized mode) is observed. The ELM can cause significant particle and energy loss, which can result in serious damages to plasma facing components. It is known that the edge pressure gradient and the edge current density play important roles in H-mode and ELM [50, 51]. In MAST and Pegasus, edge current density diagnostics using EBW (Electron Bernstein wave) emission and Hall probe array are being developed [52, 53].

(3) Plasma equilibrium in RF start-up experiments

In order to realize a spherical tokamak fusion reactor, the CS must be eliminated to achieve sufficiently low aspect ratio. In the absence of the CS, an effective non-inductive plasma current start-up method to reach high enough plasma current and plasma temperature must be developed. Plasma start-up experiments using radio frequency (RF) waves are being performed in TST-2, QUEST, LATE and MAST spherical tokamaks [54–57]. In TST-2 and LATE experiments, equilibrium calculations suggest that a highly localized plasma current in the plasma edge region [58, 59]. These localized currents are considered to be carried by highly energetic electrons accelerated by RF waves [60, 61]. Understanding of the physical mechanisms of current generation current density profile formation is needed to extrapolate knowledge from past experiments on conventional tokamaks.

(4) Measurement of filamentary structures

Filamentary structures have been observed during MHD activities such as ELMs and IREs. Such filamentary structures can cause localized heat loads on plasma facing components and a wide range of studies using visible-light imaging by high-speed cameras and three-dimensional MHD simulations have been performed [25, 62]. For the study of filamentary structures, it is important to obtain information on its spatial scale in toroidal, poloidal and radial directions, how they are created, and how much current they carry. These properties are needed to calculate their effects on plasma facing components including diverter target plates for fusion reactors.

1.6.1 Magnetic probes

A magnetic pick-up coil array has been used conventionally in small low-temperature tokamaks for MHD studies [63,64]. Recently, a Hall probe array consisting of Hall element sensors was used as a current density profile diagnostic [53,65]. In these diagnostics, the current density profile is reconstructed from the measured poloidal magnetic field profile using Ampere's law, $\mu_0 \boldsymbol{j} = \boldsymbol{\nabla} \times \boldsymbol{B}$. An example of current density profile measurement using a pick-up coil array is shown in Ref. [28,63]. Pick-up coils mounted on a probe shaft were used to measure the radial profile of the poloidal magnetic field. For tokamak plasmas, the toroidal current density j_t can be derived from

$$\mu_0 j_\mathrm{t} = \frac{\partial B_\mathrm{p}}{\partial r} - \frac{\partial B_\mathrm{r}}{\partial z}, \tag{1.43}$$

$$= \frac{\partial B_\mathrm{p}}{\partial r} - \frac{B_\mathrm{p}}{a}, \tag{1.44}$$

where B_p is the poloidal magnetic field, B_r is the radial magnetic field, a is the radius of curvature of the magnetic field at the pick-up coil. Equation 1.44 is derived assuming the cylindrically symmetric assumption of the plasma shape. The advantage of this diagnostic is that both the magnetic field profile and the current density profile can be obtained simultaneously. However, there are several difficulties for accurate determination of the current density profile as described below.

On the mid-plane of a tokamak plasma, the magnitude of B_r is much smaller than B_t or B_p. For example, in TST-2 Ohmic plasmas, B_t and B_p are typically in the range 0.1–0.3 T and 0.04–0.08 T while B_r is less than 5 mT. Thus, for a precise measurement of B_r, coil windings with very small sensitivities to B_t and B_p are required. If there is a measurement error of about 10% for B_r, the error for spatial differentiation can easily become large. In addition, high accuracies are required for location and orientation of the pick-up coils on the probe head. For the same reasons, the first term on the right hand side of Eq. (1.43) tends to have large measurement errors.

It is difficult to measure an unknown current density profile or fine-scale structures in the current density profile with magnetic pick-up coils. Figure 1.21(a) shows a case with line currents orthogonal to the page in alternating directions. The rectangles labeled Pick 1 and Pick 2 are pick-up coils. In order to derive I_1, the horizontal spatial derivative must be calculated accurately from the signals measured by Pick 1 and Pick 2. For Pick 1, I_1 produces B_1 in the upward direction, and I_2 also produces aB_2 in the same direction, so Pick 1 cannot distinguish B_1 from B_2. In addition, Pick 1 is also sensitive to B_3 created by I_3. The situation is the same for Pick 2. In this case, the spatial derivative cannot be determined

uniquely, and I_1 cannot be calculated unambiguously. When the current density profile is unknown, this diagnostic has such an uncertainty.

Figure 1.21(b) shows the case in which a small structure in the current density profile exists between the pick-up coils but its position is closer to Pick 1. In this case, the magnetic fields at Pick 1 and Pick 2, and their difference are given by

$$\begin{aligned} B_1 &= \frac{\mu_0 I}{2\pi}\frac{1}{l_1}, \\ B_2 &= -\frac{\mu_0 I}{2\pi}\frac{1}{l-l_1}, \\ B_1 - B_2 &= \frac{\mu_0 I}{2\pi}\frac{1}{l_1(1-l_1/l)}, \end{aligned} \tag{1.45}$$

When I is located half way between the pick-up coils, the difference between B_1 and B_2 is $\frac{\mu_0 I}{\pi}\frac{2}{l}$, and the ratio between this difference and Eq. (1.45) is

$$\Big(4\frac{l_1}{l}(1-\frac{l_1}{l})\Big)^{-1}. \tag{1.46}$$

As shown by this result, the pick-up coil array diagnostic has an uncertainty due to the position of the localized current between pick-up coils.

1.6.2 Rogowski coil

The Rogowski coil is a current sensor which is often used for measuring short pulse and large electrical currents [66]. Because of its high insulation ability, the Rogowski coil is employed in many industrial situations. The Rogowski coil is sometimes called the Chattock-Rogowski coil since it was described first in 1887 [67] by A. P. Chatthock. In 1921, W. Rogowski rediscovered that the Chattokck-Rogowski coil is an excellent current sensor. In tokamak plasmas, the Rogowski coil has been used for current density measurements [68], but much less frequently than pick-up coil arrays. The Rogowski coil has the form of a toroidal coil. When a time-varying electrical current passes through the hole of the Rogowski coil, an output voltage V is induced. The relationship between the current and the output voltage is given by

$$V = \frac{\mu_0 N S}{l}\frac{dI}{dt}, \tag{1.47}$$

where μ_0 is the magnetic permeability in vacuum, S is the cross-sectional area of the coil core, N is the number of turns and l is the circumference of the coil core. The Rogowski coil signal is proportional to N and S, and is inversely proportional to l.

A precisely fabricated Rogowski coil has a constant turn density N/l and a constant cross-sectional area S. Since the principle of the Rogowski coil is based on Ampere's law, an ideal Rogowski coil has no sensitivities to fields generated by currents flowing external to the Rogowski coil. Thus, when an ideal Rogowski coil has N/l and S, the total magnetic flux Φ is given by [69]

$$\Phi = \frac{SN}{l}\int_0^{2\pi r} B dl. \tag{1.48}$$

For a Rogowski coil with non-uniformity, the flux deviates from Eq. (1.48), and the Rogowski coil has unwanted sensitivities to fields generated by external currents.

The advantage of using the Rogowski coil is that it can measure the current directly without taking spatial derivatives. Thus, there are no uncertainties associated with the pick-up coil array described in Sec. 1.6.1. The same signal is obtained regardless of where the

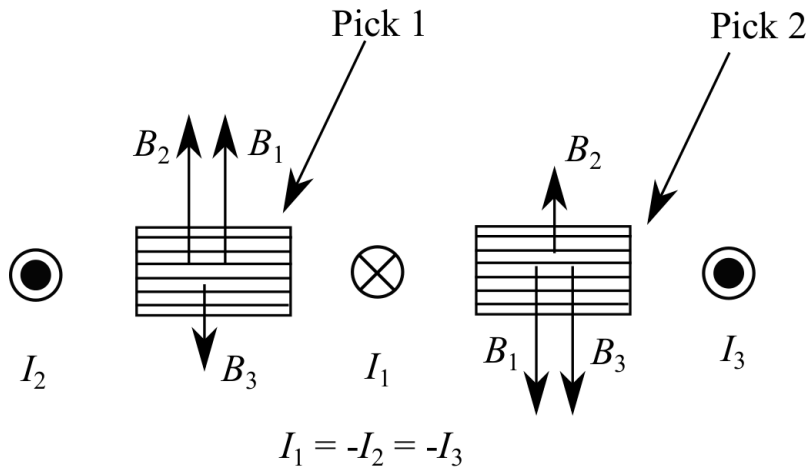

(a)

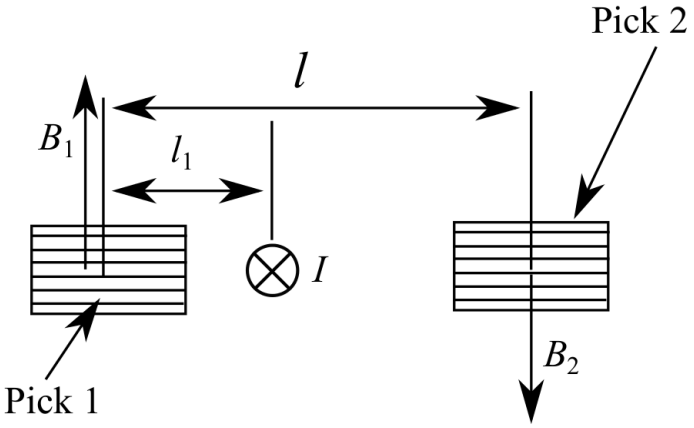

(b)

Fig. 1.21: (a) A case with one line current into the page and two line currents out of the page, and (b) a case in which a localized current exists between pick-up coils but not exactly half way. Rectangles labeled Pick 1 and Pick 2 are pick-up coils.

current passes through the hole. In addition, it is easy to calculate the current since it is obtained by using Eq. (1.47). In addition, since the Rogowski coil measures the current passing through the hole, it can measure the current direction. Since the measurement of the parallel current is quite important, the Rogowski coil has a powerful advantage compared to other methods.

However, there are some difficulties as explained below. Firstly, a small Rogowski coil is needed to achieve high spatial resolution and to minimize perturbation to the plasma. On the other hand, since the current must pass through the hole of the Rogowski coil, the hole radius must be large enough. In addition, the sensitivity of the Rogowski coil ($\mu_0 NS/l$) tends to be small. Since there is a limitation on the size of the Rogowski coil, the number of turns must be increased to improve the sensitivity. When designing a Rogowski coil for current density measurement, these tradeoffs must be considered carefully. Secondly, accurate windings with constant S and N/l are required to ensure small sensitivities to fields generated by external currents. For measuring the local current in a tokamak, a small Rogowski coil is inserted into the plasma. In tokamak discharges, there are currents external to the Rogowski coil such as the plasma current, PF coil current and TF coil current. These currents are from several kA to over 100 kA. On the other hand, the current passing through the hole of the Rogowski coil is only about 10 A. Thus, the noise source is much larger than the signal source. Thirdly, the sheath effect on the measured signal must be taken into account. The electron orbit can be affected by the plasma sheath potential formed around the hole of the Rogowski coil. This effect has never been investigated. In order to develop the Rogowski coil as a reliable current density diagnostic, it is inevitable to study the plasma sheath effect.

1.6.3 Motional Stark effect measurement

The Motional Stark Effect (MSE) measurement is a conventional current density profile diagnostic for tokamak plasmas developed by F. M. Levinton [70]. In MSE, a neutral beam is injected into the plasma and the polarization of the Balmer-alpha transition ($n = 3$ to $n = 2$) line emission from neutral hydrogen or deuterium is measured. When a neutral hydrogen or deuterium atom moves across the magnetic field with velocity $\boldsymbol{V}$, it experiences the Lorentz electric field, $\boldsymbol{E} = \boldsymbol{V} \times \boldsymbol{B}$ and the emitted Balmer-alpha light is polarized. The polarization provides a local (1–2 cm resolution) and accurate magnetic pitch angle measurement θ_{pitch} $= \tan^{-1}[B_{\mathrm{p}}/B_{\mathrm{t}}]$. From the measured pitch angle profile and equilibrium calculation, the current density profile can be reconstructed. The advantages of this measurement are that it can measure the current density without disturbing the plasma with high spatial resolution, and that the safety factor (q) profile can be obtained at the same time. Since the signal strength of MSE measurement depends on the magnetic field strength and the Stark splitting is insufficient at low magnetic fields, it is difficult to apply this technique to spherical tokamaks. Furthermore, the necessity to use a neutral beam makes it difficult for small-scale experiments.

1.6.4 EBW measurement

Since the EBW can propagate in overdense plasmas (i.e., $\omega_{\mathrm{pe}} \gg \omega_{\mathrm{ce}}$, where ω_{pe} is the electron plasma frequency and ω_{ce} is the electron cyclotron frequency), the use of EBW for emission measurement, current drive and heating is being considered as an alternative where the ECW cannot be used. In [71], it was proposed that high radial resolution measurements of the edge current density profile can be performed based on the anisotropic properties of mode conversion of the EBW, and a current density profile diagnostic was newly developed

to study H-mode plasma physics [52]. Advantages of this technique are that it can measure the current density in the plasma edge region (i.e., less limitation for the measurement of current density profile at the plasma edge), and that it can measure not only the current density profile but also the electron temperature profile in principle. However, this technique is extremely new and the analysis is complicated.

1.7 Objectives of this thesis

In previous sections, we presented representative current density diagnostics. Their features are summarized in Table 1.1.

	Large or small tokamak device	Advantages	Disadvantages
MSE	large	•high spatial resolution •both j and B •no plasma disturbance	difficult for small B device
EBW	large and small	•high spatial resolution •both j and B •no plasma disturbance	complicated analysis
Pick-up coil array	small	•both j and B •high spatial resolution	•difficult for unknown j profile •difficult for small scale current •plasma disturbance
Rogowski coil	small	•direct measurement •easy principle •current direction •high spatial resolution	•small sensitivity •highly accurate windings •sheath effect •plasma disturbance

Table 1.1: Comparison of current density diagnostics.

The first goal of this study is to develop the Rogowski coil as an edge plasma current density diagnostic, in particular for the TST-2 spherical tokamak. TST-2 is a medium-sized spherical tokamak with high experimental mobility. It has both Ohmic and RF (21 MHz, 200 MHz, 2.45 GHz and 8.2 GHz) heating systems. Ohmic plasmas in TST-2 are overdense, and MHD instabilities in the frequency of 10–100 kHz are often observed. Sometimes, IREs and disruptions are also observed. In TST-2, it is possible to perform various plasma studies including RF plasma start-up, plasma turbulence and instabilities, and disruption. For these studies, it is quite important to measure the edge current density profile as described in Sec. 1.6. The SlimCS Demo reactor with a reduced-size CS [9] and the VECTOR commercial

reactor [7] are designed with smaller aspect ratio compared to typical conventional tokamaks, and both devices require I_p ramp-up without the CS. A wide variety of tokamak fusion physics research performed on TST-2, including a successful demonstration of I_p ramp-up by RF waves, would contribute to the early realization of fusion power on earth.

As shown in Table 1.1, there are some difficulties to be solved in developing the Rogowski coil as a current density profile diagnostic, to increase the sensitivity, to wind the coil with high precision and uniformity, and to consider the sheath effect. In addition, no one has compared the pick-up coil array and the Rogowski coil directly. Since the Rogowski coil has good linearity, it can be used to measure both slow evolutions of the current density profile and fast fluctuations. Furthermore, it can measure the direction of current flow. Thus, it is a powerful diagnostic for current density profile measurement, and enables studies of various plasma fusion topics. For example, during an IRE, an existence of a localized filamentary current structure is expected from 3 dimensional MHD simulation [25]. It is quite interesting to measure such structures using a Rogowski coil. In addition, it is important to determine the time sequence of physical phenomena during an IRE (i.e., to identify the trigger mechanism for IRE). In RF plasma start-up experiments, the Rogowski coil can be a powerful tool since it can measure the local current directly with no uncertainties even for the case with unknown current profile. The objectives of this thesis are:

1. to develop a small Rogowski coil with highly accurate windings and large number of turns
2. to measure a slow evolution of current density in Ohmic plasmas
3. to study the plasma sheath effect for the Rogowski coil diagnostic
4. to compare measurements using the pick-up coil array and the Rogowski coil
5. to measure the plasma current in the edge region in RF start-up plasmas
6. to confirm the existence of current density fluctuations and to investigate the time sequence of physical phenomena during an IRE

Chapter 2

Development of a small multilayer Rogowski coil

2.1 Numerical evaluation of sensitivity to external fields

Two types of Rogowski coil are well known. One has a normal forward helical winding around the torus (mainly poloidal turns with one toroidal turn) and a backward toroidal winding called the return cable. The other has two layers of winding: one layer of forward helical winding and another layer of backward helical winding. Hereafter, these two types are referred to as the return winding and the two-layer winding, respectively. Ten Rogowski coils of each type were made, and we found that the two-layer winding always performed better than the return winding. This is probably because of the difficulty in precisely adjusting the area enclosed by the return coil. Thus, we used the two-layer winding in our experiment. To estimate and minimize the sensitivity of the two-layer winding to external magnetic fields, we performed numerical simulations. The configuration of the Rogowski coil and external magnetic fields $B_{\rm z}$ (corresponding to the toroidal field in a tokamak) and $B_{\rm y}$ (corresponding to the poloidal field in a tokamak) are shown in Fig. 2.1.

The wire of the Rogowski coil was represented by a set of points with coordinates (r, θ, z), and the fabrication error was simulated by adding random errors to each coordinate at each point. In the rectangular cross-section case, we need four points per turn to define the wire. In a uniform magnetic field, the effective projection areas ($S_{\rm x-y}$ and $S_{\rm x-z}$) give the sensitivity to the external magnetic fields. These areas are calculated by summing up the projected areas of the triangles formed by two adjacent coordinates on the wire and a reference point. For a Rogowski coil with finite $S_{\rm x-y}$ and $S_{\rm x-z}$, the relationship between the output voltage and, the toroidal and poloidal components of the magnetic field ($B_{\rm t}$ and $B_{\rm p}$) are given as

$$V_{\rm B_t} = S_{\rm x-y}\frac{\partial B_t}{\partial t}, \tag{2.1}$$

$$V_{\rm B_p} = S_{\rm x-z}\frac{\partial B_{\rm p}}{\partial t}. \tag{2.2}$$

In the simulation, the outer diameter, the inner diameter, the thickness, and the number of turns of the Rogowski coil are taken to be 20 mm, 12 mm, 12 mm and 240 turns, respectively. The calculation was repeated 500 times with different sets of random errors. The results are shown in Fig. 2.2. The error bar is the standard deviation derived from 500 trials. From

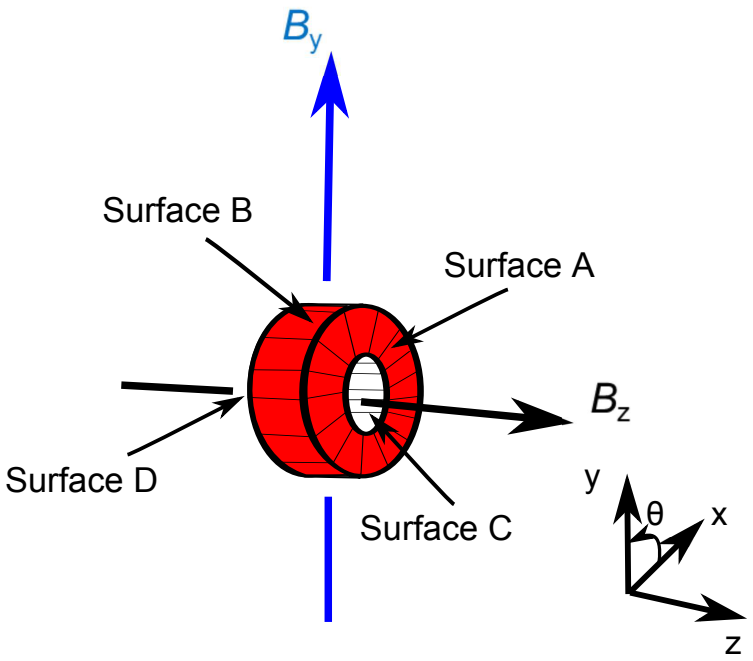

Fig. 2.1: Rogowski coil in an external field. B_z corresponds to the toroidal field in a tokamak, and B_y corresponds to the poloidal field in a tokamak [72].

Figs. 2.2 (a), (b) and (c), it can be seen that the manufacturing errors in the θ direction tends to cause higher sensitivity than those in the r or z directions.

2.2 Optimum two-layer winding

In the previous section, it was found that minimizing the errors in the θ direction reduces S_{x-y} and S_{x-z} effectively. Several winding cores with small cutouts at the corners were made in order to set the correct number of turns by fixing the cable in place precisely. We tested three cutout arrangements with the same size and number of turns. The three winding patterns are shown in Fig. 2.3. The red and blue lines represent the forward and backward windings, respectively. Surfaces A, B, C and D are defined in Fig. 2.1. In pattern 1, the cutouts on all surfaces have the same phase (i.e., at the same θ). In pattern 2, the cutouts on the right and left sides of surfaces B and C have the same phase, and the cutouts on the two sides of surfaces A and D have the opposite phase (i.e., shifted by half a period). In pattern 3, the cutouts on the two sides of surfaces A and B have the opposite phase and the cutouts on the two sides of surfaces C and D have the same phase.

We wound the Rogowski coils manually on the three winding cores. In order to determine which pattern is most effective for reducing unwanted sensitivities (i.e., S_{x-y} and S_{x-z}), we performed a test using a Helmholtz coil. The Helmholtz coil consists of two circular coils with the same radius a, separated from each other by distance a. This configuration is very similar to a pair of PF coils (upper and lower) in a tokamak. A precisely fabricated Helmholtz coil produces a constant and straight magnetic field in the direction of the coil axis inside the region between the two coils. A configuration for the sensitivity test is shown in Fig. 2.4. The Rogowski coil is located at the center of the Helmholtz coil, and is connected to an

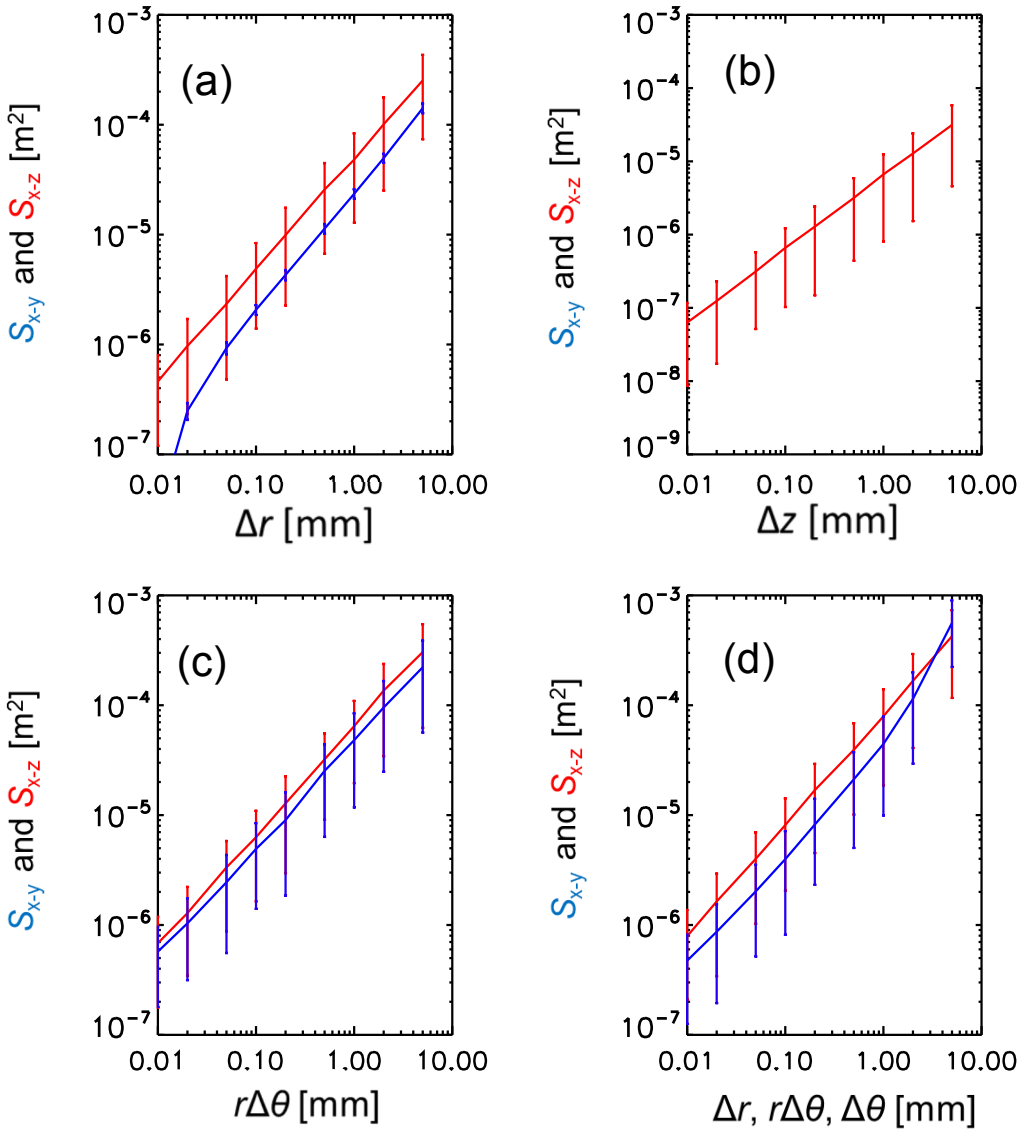

Fig. 2.2: $S_{\mathrm{x-y}}$ and $S_{\mathrm{x-z}}$ of the two layer winding, where Δr, Δz and $r\Delta\theta$ are errors in each direction [72].

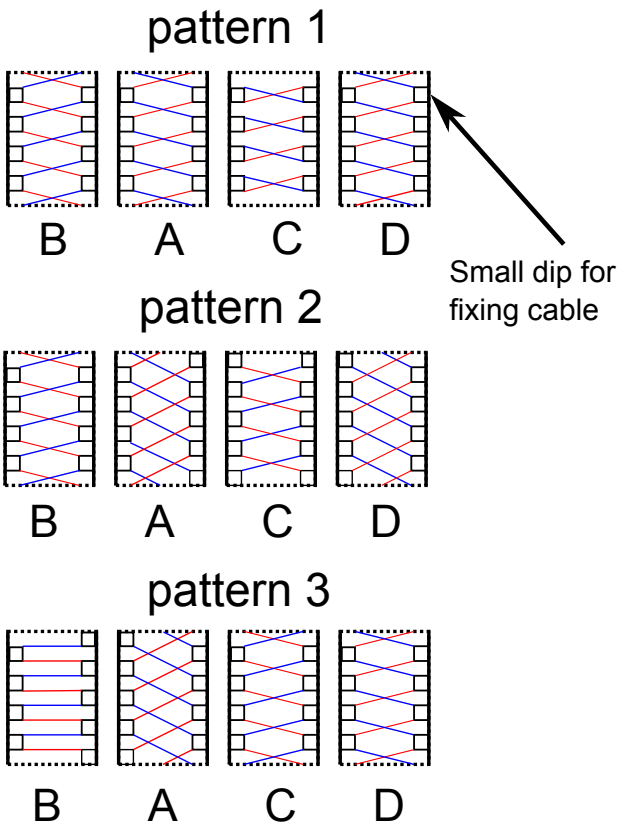

Fig. 2.3: The three winding patterns tested. Surfaces A, B, C and D denote the four (top, inner, bottom, and outer) surfaces of the rectangular cross section of the winding core (see Fig. 2.1) [72].

amplifier circuit. By applying an alternating current to the Helmholtz coil from a function generator and a bipolar amplifier, we can test the sensitivities to external magnetic fields, $S_{\mathrm{x-y}}$ and $S_{\mathrm{x-z}}$.

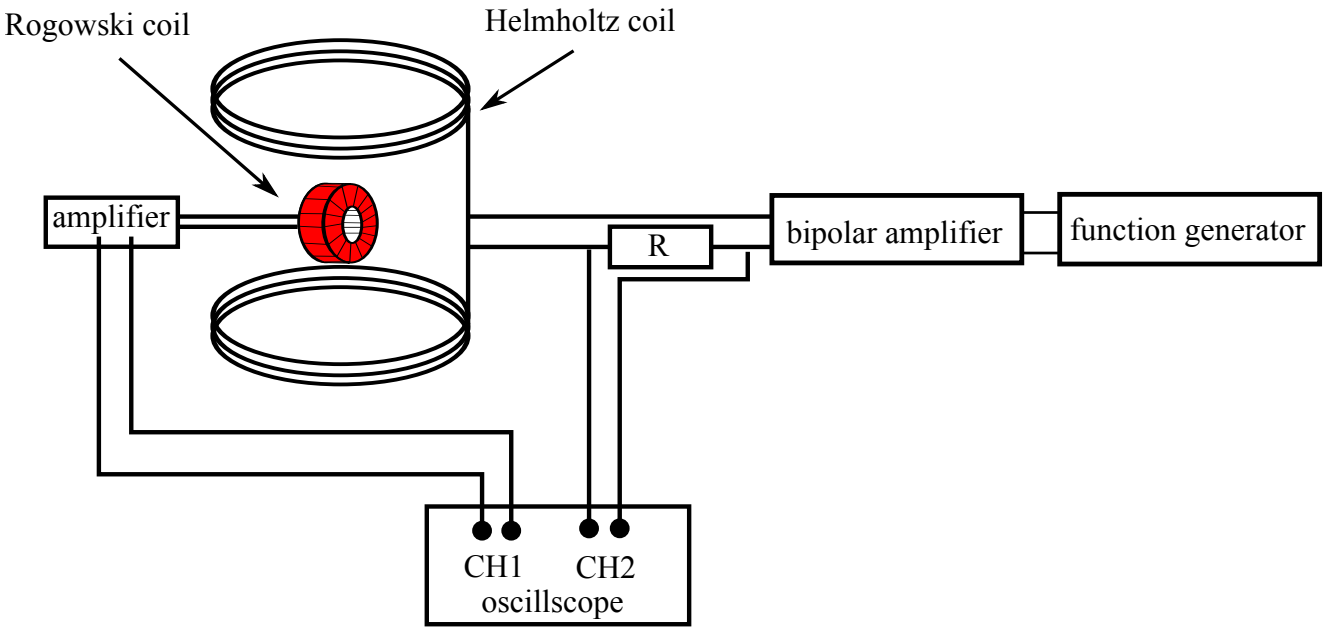

Fig. 2.4: Configuration of sensitivity test to determine $S_{\mathrm{x-y}}$ and $S_{\mathrm{x-z}}$ [72].

pattern	$S_{\mathrm{x-y}}$ [m^2]	$S_{\mathrm{x-z}}$ [m^2]
pattern 1	1.8×10^{-5}	4×10^{-5}
pattern 2	1×10^{-5}	4×10^{-5}
pattern 3	1.8×10^{-5}	2×10^{-6}

Table 2.1: Sensitivity comparison of the three Rogowski coils.

Table 2.1 summarizes the results of the test. The sensitivity to B_{z} ($S_{\mathrm{x-y}}$) was always $\sim 10^{-5}$ m^{-2} for all patterns. On the other hand, the sensitivity for pattern 3 to B_{y} ($S_{\mathrm{x-z}}$) was always an order of magnitude smaller than for patterns 1 and 2. The cable is wound with a certain tension so that the cable is fixed in place at each cutout. Therefore, it is useful to have a zigzag pattern in addition to the uniform helical structure necessary for the Rogowski coil. The cable traversing surfaces A, C and D in pattern 1 has almost no zigzag structure. On the other hand, there are zigzag patterns on all surfaces in patterns 2 and 3, so it can be expected that $S_{\mathrm{x_y}}$ for pattern 2 is as small as that for pattern 3. To explain the experimentally observed difference, we simulated patterns 2 and 3, but no noticeable difference between the two patterns was seen. Although we were unable to explain why $S_{\mathrm{x_z}}$ for pattern 3 is better (i.e., smaller) than that for pattern 2, we adopted pattern 3 based on these measurements.

2.3 Multi-layer Rogowski coil

To obtain a large signal intensity, the cross sectional area S and the number of turns N should increase, and the circumference of the coil core l should decrease. As a local current diagnostic, the Rogowski coil must be sufficiently small. On the other hand, the size of the central hole of the Rogowski coil should be large enough to enable the local current to pass through. S and l must be determined considering these aspects. On the other hand, it is clear that a larger signal can be obtained for larger N. Therefore, the number of turns must be large to obtain sufficient signal intensity. To increase N, we used a twisted wire pair. If we use a twisted wire for a two-layer winding, we can make a four-layer Rogowski coil. The use of a twisted wire shortens the winding time and improves durability. A small Rogowski coil with a large number of turns is wound using a thin cable, but that requires careful winding and increases the fabrication time. By making a four layer Rogowski coil with two forward and two backward windings using a twisted wire, we successfully fabricated an eight-layer Rogowski coil (Fig. 2.5). When we compare the and, The fabrication times per unit turn for the eight-layer winding is a factor of 20 shorter than for the one-layer return-type winding. The eight-layer winding performed better than the twelve-layer winding. In making a twelve-layer Rogowski coil, it was difficult to count the number of turns in a cutout. Furthermore, it was difficult to keep the winding uniform for a twelve-layer Rogowski coil. After winding the cable, it is necessary to adjust the position of the cable at the cutout (cutout width = 0.5 mm) using a small tool like a thin needle. We made the adjustment by monitoring the

Fig. 2.5: Eight-layer Rogowski coil: Outer diameter = 20 mm; inner diameter = 12 mm; thickness = 12 mm; number of turns = 360; and cable diameter = 0.12 mm [72].

sensitivity, and achieved a good performance as shown in Sec. 2.5. For Ohmically heated plasmas, the dominant sources of noise are from B_{z} and B_{y}. We define the signal-to-noise ratio S/N as $S/N(B_{\mathrm{z}})$, $S/N(B_{\mathrm{y}})$, which are the ratios of the current signal to noise in the B_{z} and B_{y} directions, respectively. The S/N depends not only on $S_{\mathrm{x-y}}$ and $S_{\mathrm{x-z}}$, but also on coil dimensions, the magnitude of noise, and the magnitude of signal. They can be defined as

$$SN(B_{\mathrm{z,\,y}}) = \frac{K_{\mathrm{A}}\pi r_{\mathrm{inner}}^2}{S_{\mathrm{x-y,\,x-z}}}\frac{j}{B_{\mathrm{z,\,y}}}, \tag{2.3}$$

where K_{A} is the sensitivity to the current passing through the hole, r_{inner} is the inner radius, j is the current density in front of the hole. Here, we assumed that j is constant throughout the hole region. As is shown in Eq. 2.3, $S/N(B_{\mathrm{z,\,y}})$ also depends on r_{inner}. Using the method described in Sec. 2.1, we can calculate the dependences of $S/N(B_{\mathrm{z,\,y}})$ on coil dimensions. The calculation results are shown in Fig. 2.6.

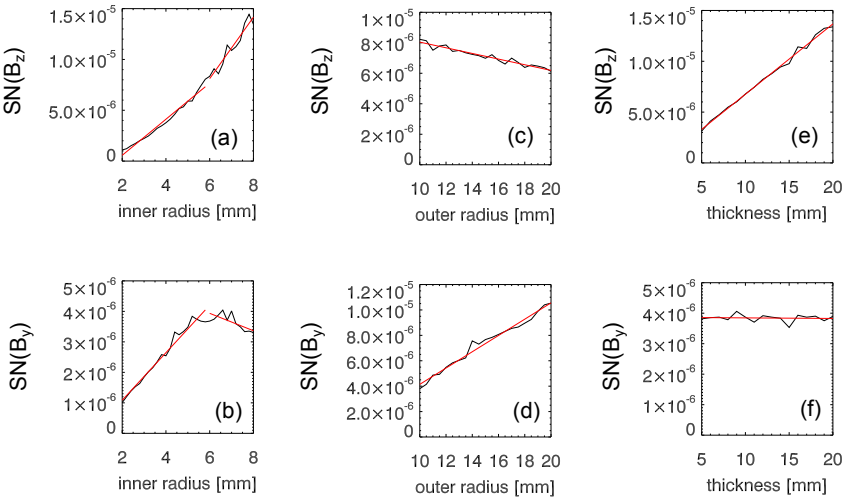

Fig. 2.6: Dependences of $S/N(B_{\mathrm{z,\,y}})$ on Rogowski coil dimensions. (a) and (b) Dependences on the inner radius, (c) and (d) dependences on the outer radius , and (e) and (f)dependences on the thickness. Typical dimensions: outer diameter = 20 mm, inner diameter = 12 mm, thickness = 12 mm, and number of turns = 360. Black curve shows the calculation result and the red curve shows the linear fitting result [72].

From Fig. 2.6, we found that $S/N(B_{\mathrm{z}})$ increases with the inner radius and the thickness, whereas it decreases with the outer radius. $S/N(B_{\mathrm{y}})$ increases with the outer radius and it is independent of the thickness. On the other hand, $S/N(B_{\mathrm{y}})$ is optimized by controlling the inner radius. This is due to the dependence on the radius of the hole. The outer radius and the thickness were determined from the viewpoints of plasma disturbance and fabrication.

2.4 Frequency response of the multi-layer Rogowski coil

Since an equivalent circuit of a Rogowski coil consists of an inductance L and a capacitance C [73], the sensitivity of a Rogowski coil has a frequency-dependent response to the current passing through the hole of the Rogowski coil. For the measurement of the current, we need to know such characteristics. The frequency response can be checked from a calibration. The calibration setup for a Rogowski coil is shown in Fig. 2.7. A function generator (FG) is a source of voltage. The Rogowski coil signal is proportional to the frequency and magnitude of the current passing through the hole (see Eq. 1.47). The current flowing through the hole of the Rogowski coil is measured by the voltage drop across the resistance R in Fig. 2.7. The sensitivity at each frequency is obtained by changing the frequency of the current using the FG. The calibration result is shown in Fig. 2.8. Figs. 2.8(a) and (b) show the frequency responses of the sensitivity and the phase difference between the current being measured and the output signal of the Rogowski coil. From (a) and (b), linear dependences on the

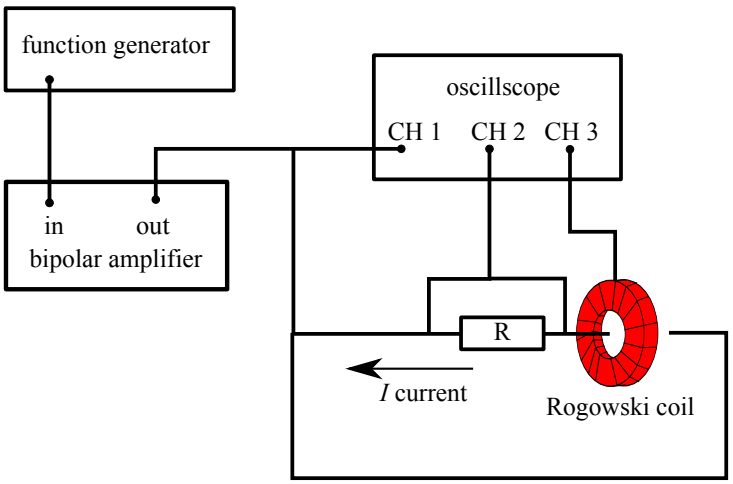

Fig. 2.7: Calibration setup for a Rogowski coil.

frequency is seen up to 200 kHz, and the sensitivity and the phase difference start to increase and decrease sharply from about 300 kHz. The resonance frequency is around 350 kHz.

2.5 Typical signals of the Rogowski coil

The sensitivities to external magnetic fields were measured using a Helmholtz coil as shown in Fig. 2.4. A typical frequency for calibration was 500 Hz, which is far from the resonance frequency (around 350 kHz, see Fig. 2.8) of the Rogowski coil. Because the output signal of the Rogowski coil was very small, an amplifier with a gain of 100 was used. $S_{\mathrm{x-y}}$ and $S_{\mathrm{x-z}}$ were 1.37×10^{-6} m^2 and 5.20×10^{-6} m^2, respectively. We also simulated $S_{\mathrm{x-y}}$ and $S_{\mathrm{x-z}}$ for the eight-layer Rogowski coil. Comparing the calibration and simulation results, the fabrication accuracy of the eight-layer Rogowski coil is determined to be smaller than ± 0.1 mm. The eight-layer Rogowski coil was used to measure the edge current in Ohmic plasmas. In the experiment, the output of the Rogowski coil was connected to an integrator circuit with a cutoff frequency of about 0.03 Hz and a gain of about 1100 s^{-1}. The Rogowski coil was located just inside the last closed flux surface ($R = 551$ mm) and on the mid plane ($Z = 0$ mm). Figure 2.9 (b) shows the time evolution of the local current measured by the Rogowski coil. The observed local current was about 15 A when the plasma current reached its maximum value. On the other hand, the expected current calculated assuming a parabolic current density profile is 10 A. In the discharge, an abrupt current drop was seen at 23 ms. This seems to be caused by an internal reconnection event that redistributes the current [18].

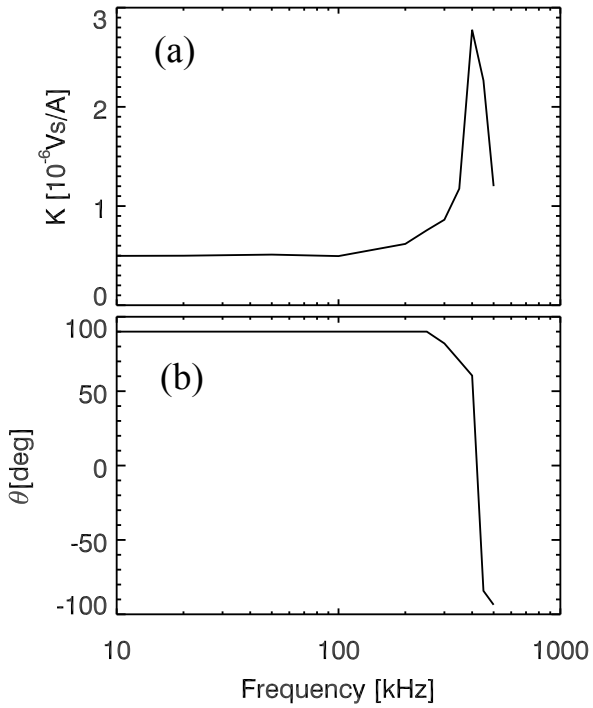

Fig. 2.8: Calibration result for the Rogowski coil. (a) Frequency response of the sensitivity and (b) frequency response of the phase difference between the current and the output signal of the Rogowski coil.

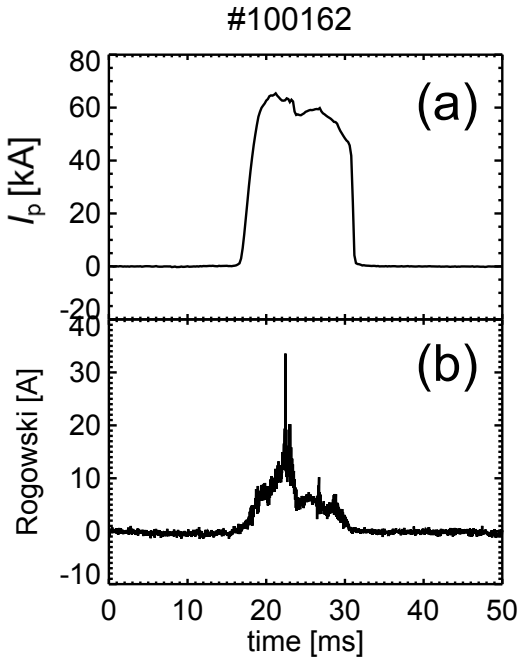

Fig. 2.9: Time evolutions of (a) the plasma current and (b) the local current measured by the Rogowski coil [72].

Chapter 3

Performance of the Rogowski probe

3.1 Rogowski probe

For the measurement of the current density profile in TST-2, we fabricated a Rogowski probe consisting of two multi-layer Rogowski coils [72], five pick-up coils and two Langmuir probes [74]. Cross-sectional views of the Rogowski probe head is shown in Fig. 3.1. The probe head is covered by copper shielding and enclosed in a ceramic cover. There is a ceramic cylinder through the hole of the Rogowski coil to prevent direct contact with the plasma. The two multi-layer Rogowski coils and pick-up coils are lined up in the radial direction. Pick-up coil 1 and pick-up coil 3 consist of two pick-up coils for measuring the toroidal and poloidal magnetic fields ($B_{\rm t}$ and $B_{\rm p}$) simultaneously. Pick-up coil 2 is a one dimensional pick-up coil. The dimensions of the Rogowski probe head are 27 mm by 27 mm by 156 mm. The radius of the hole is 4.6 mm. The probe is located on the equatorial plane ($Z = 0$ mm) of TST-2. The copper shielding has a thickness of less than 0.5 mm, and is connected to the tokamak ground (i.e., the TST-2 vacuum vessel). The Rogowski probe can be moved along the major radius of the tokamak, and can be rotated around the shaft axis (in the toroidal-poloidal plane. Thus, measurements of the current density (Rogowski coils), magnetic field (pick-up coils), and pressure (Langmuir probes) profiles in the major radial direction, including the angular dependence in the toroidal-poloidal plane, can be accomplished. The definition of the orientation angle of the Rogowski coil hole is shown in Fig. 3.2. The dashed arrow indicates the direction of the hole axis and θ is the angle between the hole direction and the toroidal direction. When θ is set to 0° (i.e., the hole direction is parallel to the toroidal direction), pick-up coil 2 measures $B_{\rm p}$. In the case of $\theta = 90^\circ$, pick-up coil 2 measures $B_{\rm t}$. Figure. 3.3 shows a photograph of the Rogowski probe seen from inside of the vacuum vessel of TST-2.

3.2 Integrator circuit

The output voltage of a Rogowski coil is the time derivative of the current passing through the hole. In order to study the time evolution of the current $I(t)$, this signal must be integrated. First we tested numerical integration, but we found that numerical integration does not produce reliable results because of large fluctuations on the Rogowski coil signal. Thus, we decided to use an analog integrator circuit. A circuit diagram of the integrator is shown in Fig. 3.4. It has a gain of $G = 2200\,{\rm s}^{-1}$ and an integration time of 4.7 s, which are sufficient for both Ohmic and RF plasmas in TST-2. The electromagnetic noise from TF, PF and OH coil currents were successfully reduced to a low enough level by wiring the circuit

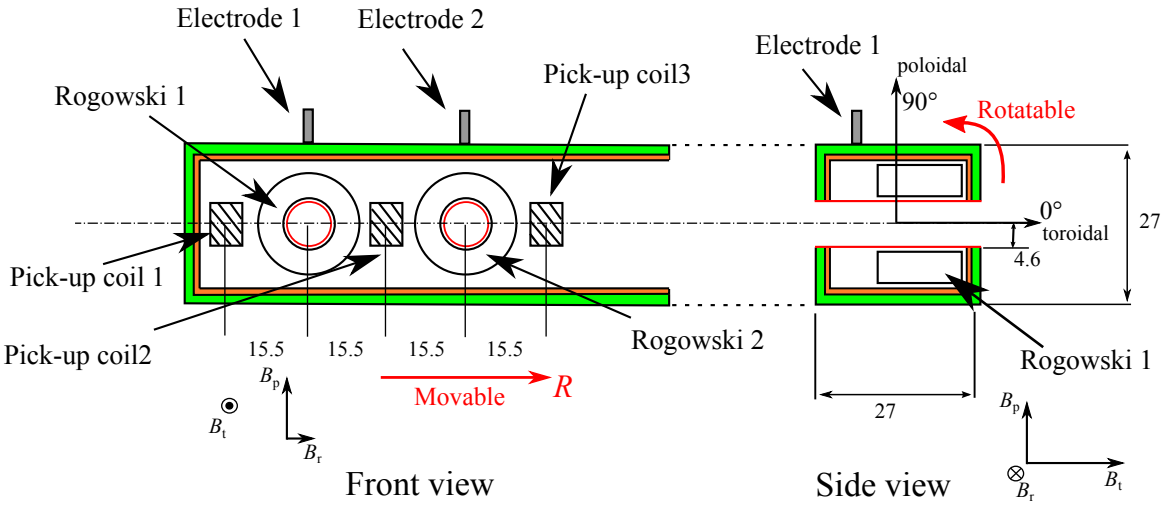

Fig. 3.1: Cross-sectional views of the Rogowski probe consisting of Rogowski coils 1 and 2, pick-up coils 1 through 3, and Langmuir probe electrodes 1 and 2. The Rogowski probe assembly is covered by copper shielding (orange region) and enclosed in a ceramic cover (green region). There is a ceramic cylinder (red region) through the hole of the Rogowski coil to prevent direct contact with the plasma.

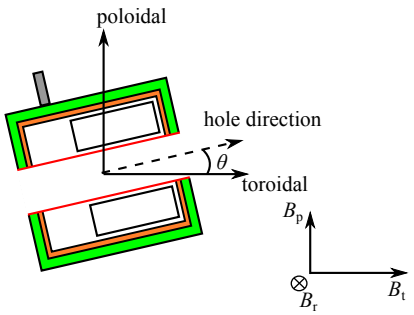

Fig. 3.2: Definition of the Rogowski coil hole direction.

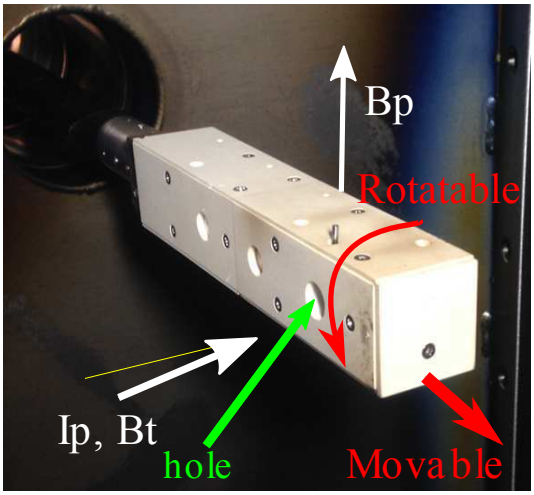

Fig. 3.3: Photograph of the Rogowski probe seen from inside the TST-2 vacuum vessel.

carefully to avoid the ground loop between the two operational amplifiers. The white noise tends to be large because of the long integration time and large gain. We tested many kinds of operational amplifiers, and found that the smallest white noise is achieved with a set of two OPA627ap.

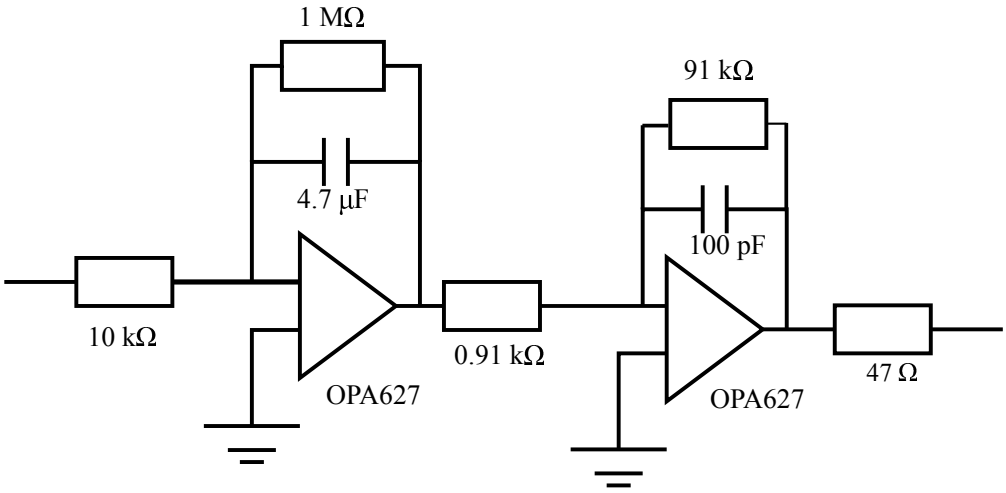

Fig. 3.4: Integrator circuit for the Rogowski coil.

The current sensitivities of the Rogowski coils (Rogowski 1 and Rogowski 2 in Fig. 3.1) are $K \simeq 5 \times 10^{-7}$ Vs/A. The output voltage of the integrator circuit for the Rogowski coil can be written as

$$V_{\text{out}} = G \int V_{\text{Rogowski}}\, dt = GKI(t). \tag{3.1}$$

where V_{Rogowski} is the raw output signal of the Rogowski coil. We can see that V_{out} is proportional to $I(t)$. Calibration similar to that shown in Fig. 2.7 was performed for the integrator connected to the output of a Rogowski coil. The is shown in Fig. 3.5. The current measured by the Rogowski coil was calculated using Eq. (3.1), and was also measured from

the voltage drop across the resistor. Good agreement was obtained between them. Using Eq.

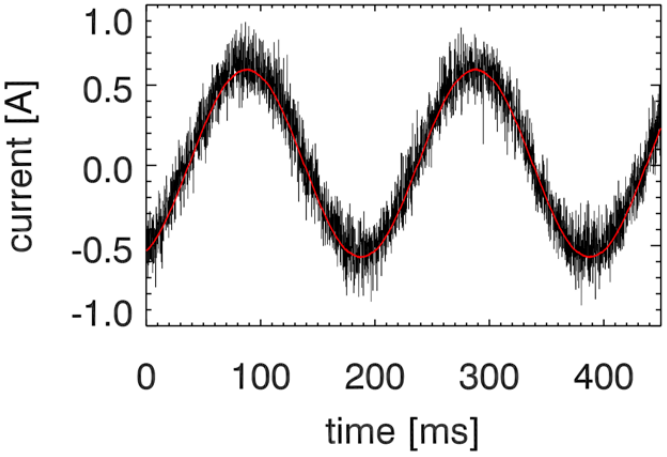

Fig. 3.5: Result of calibration of the integrator circuit connected to the output of a Rogowski coil. Black: current calculated from the integrator output signal using Eq. (3.1). Red: current passing through the hole of the Rogowski coil measured by the voltage drop across a resistor as shown in Fig. 2.7).

(3.1) and the area of the hole for the current to pass, we can calculate the current density as

$$j = I/(\pi a^2) = V_{\rm out}/(GK\pi a^2) \tag{3.2}$$

where a is the radius of the hole. In the following sections and chapters, we calculate the current densities using Eq. (3.2).

3.3 Absolute sensitivity calibration of magnetic pick-up coils

In this section, we present the method and result of absolute calibration of the pick-up coils installed in the Rogowski probe head. As described in Sec. 3.1, pick-up coils 1 and 3 are two-dimensional pick-up coils, each consisting of two orthogonal pick-up coils. Hereafter, we call the pick-up coils in pick-up coil 1 and 3 as pick-up coil 1-1 pick-up coil 1-2, and pick-up coil 3-1, pick-up coil 3-2. When the hole direction is set to be 0°, pick-up coils 1-1 and 3-1 measure the toroidal magnetic field $B_{\rm t}$ and pick-up coils 1-2 and 3-2 measure the poloidal magnetic field $B_{\rm p}$. The outputs of these pick-up coils are also connected to the integrator circuit to obtain the time evolution of the magnetic field components.

First, we show typical signals of pick-up coils when only the TF coil was energized for the case of $\theta = 40°$ (see Fig. 3.6). Since the hole direction is 40°, all pick-up coils show signals very similar to the time evolution of $B_{\rm t}$ calculated from the TF coil current. By fixing the location of the Rogowski probe head in the major radius direction, and by changing the direction of the hole in the toroidal-poloidal plane (i.e., changing θ), we can test the dependence of $B_{\rm t}$ sensitivity on θ for each pick-up coil. The result is shown in Fig. 3.7. In this test, $B_{\rm t}$ for each coil location was calculated from the TF coil current, and black symbols show the measured sensitivity ($V_{\rm out}/B_{\rm t}$, where $V_{\rm out}$ is the output voltage of a pick-up coil). The sensitivities of pick-up coils 1-1 and 3-1 show a sine wave shape while the other pick-up coils show a

cosine wave shape. For the case of $\theta = 0°$, pick-up coils 1-1 and 3-1 measure B_t, while the other three coils measure B_p. In this case, the former coils and the latter coils must show approximately the maximum and the minimum sensitivities and their angular dependence must be sine and cosine curves. Thus, the test result is consistent with the expectation. Red curves in Fig. 3.7 are fitted curves using the functions

$$K_{Bt}(\theta) = a_0 \cos(\theta + a_1) + a_2 \ (B_t \text{ sensitivity for pick-up coil 1-1 and 3-1}), \quad (3.3)$$
$$K_{Bt}(\theta) = a_0 \sin(\theta + a_1) + a_2 \ (B_t \text{ sensitivity for pick-up coil 1-2, 2 and 3-2}), \quad (3.4)$$

where $K_{Bt}(\theta)$ is the B_t sensitivity as a function of θ. By moving fitting functions in the θ direction by $-\frac{\pi}{2}$, the sensitivities to B_p can be written as

$$K_{Bp}(\theta) = -a_0 \sin(\theta + a_1) + a_2 \ (B_p \text{ sensitivity for pick-up coil 1-1 and 3-1}), \quad (3.5)$$
$$K_{Bp}(\theta) = a_0 \cos(\theta + a_1) + a_2 \ (B_p \text{ sensitivity for pick-up coil 1-2, 2 and 3-2}), \quad (3.6)$$

where $K_{Bp}(\theta)$ is the B_p sensitivity as a function of θ. Good fits were obtained using Eqs. (3.3) and (3.4) The fitted parameters, a_1, a_2 and a_3, are listed in Table. 3.1.

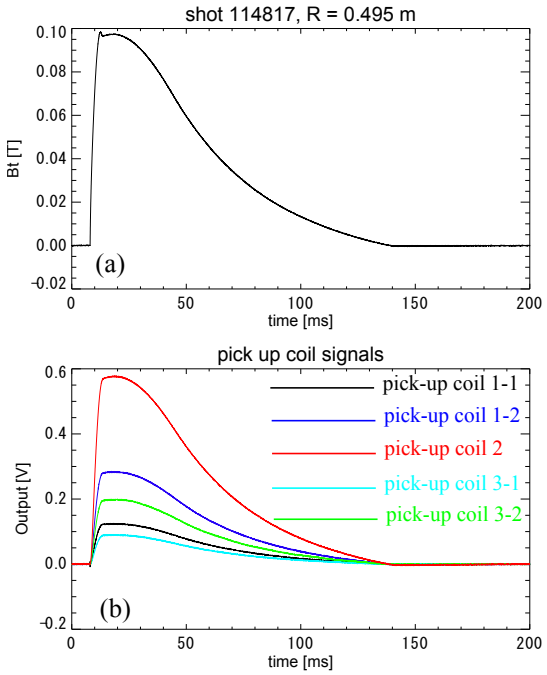

Fig. 3.6: Typical signals of pick-up coils for the case of $\theta = 40°$. (a) Time evolution of B_t at $R = 0.495$ m calculated from the TF coil current I_{TF} ($B_t = \frac{\mu_0 I_{TF}}{2\pi R}$). (b) Time evolutions of pick-up coil signals.

Measurement of magnetic field pitch angle

By using a two-dimensional pick-up coil, the magnetic field strength $B = \left({B_t}^2 + {B_p}^2\right)^{0.5}$ and the magnetic field pitch angle $\theta_{pitch} = \tan^{-1}(B_p/B_t)$ can be calculated. For example, when pick-up coil 1 is oriented at a finite angle θ (see fig. 3.2), pick-up coil 1-1 and pick-up coil 1-2 have finite effective cross sections in both toroidal and poloidal directions. Thus, the their

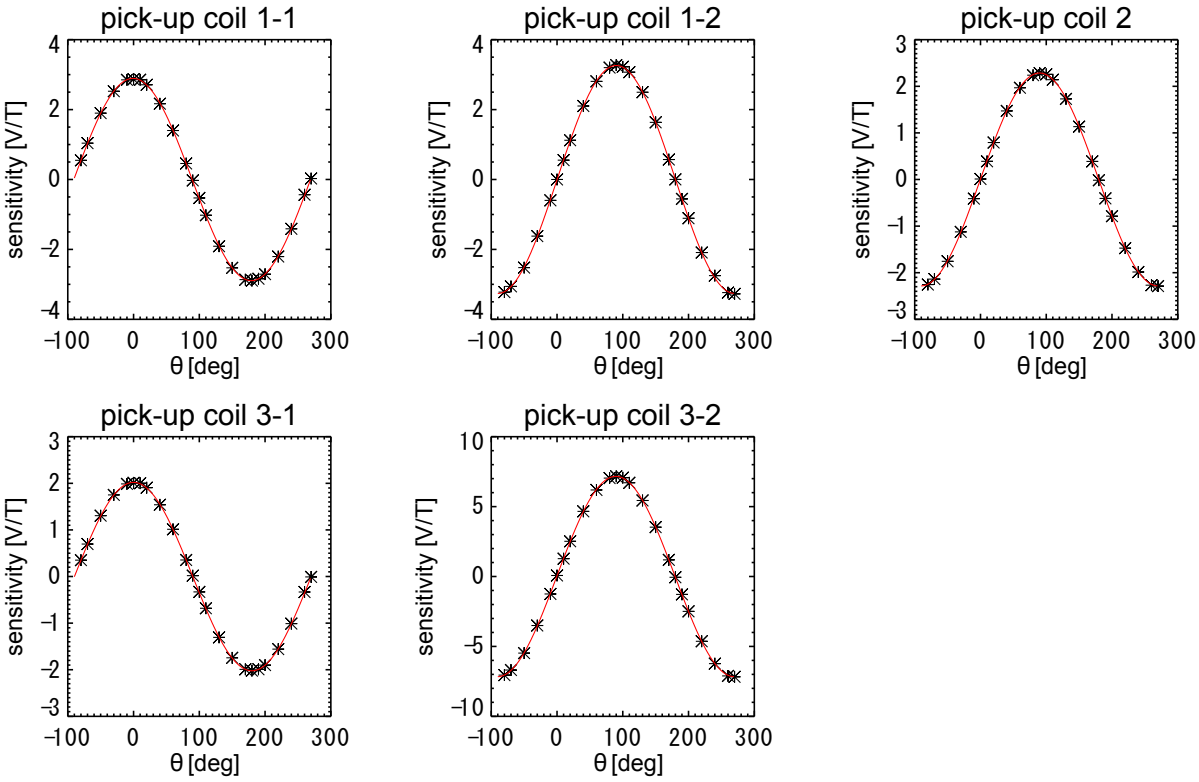

Fig. 3.7: Dependence of B_{t} sensitivity on θ for each pick-up coil. Black symbols: measured sensitivity. Red curves: curves fitted by $a_0\cos(\theta + a_1) + a_2$ or $a_0\sin(\theta + a_1) + a_2$.

pick-up coil	a_0	a_1	a_2	fitting function for B_{t}	fitting function for B_{p}
pick-up coil 1-1	2.89	0.0149	-0.0010	$a_0\cos(\theta + a_1) + a_2$	$-a_0\sin(\theta + a_1) + a_2$
pick-up coil 1-2	3.26	-0.0030	0.0009	$a_0\sin(\theta + a_1) + a_2$	$a_0\cos(\theta + a_1) + a_2$
pick-up coil 2	2.28	0.0029	-0.0042	$a_0\sin(\theta + a_1) + a_2$	$a_0\cos(\theta + a_1) + a_2$
pick-up coil 3-1	2.02	-0.0015	0.0024	$a_0\cos(\theta + a_1) + a_2$	$a_0\cos(\theta + a_1) + a_2$
pick-up coil 3-2	7.16	0.0070	-0.0037	$a_0\sin(\theta + a_1) + a_2$	$-a_0\sin(\theta + a_1) + a_2$

Table 3.1: Fitted parameters from sensitivity calibration of pick-up coils.

signals are expressed by a linear combination of $B_{\rm t}$ and $B_{\rm p}$. The geometry is shown in more detail in Fig. 3.8.

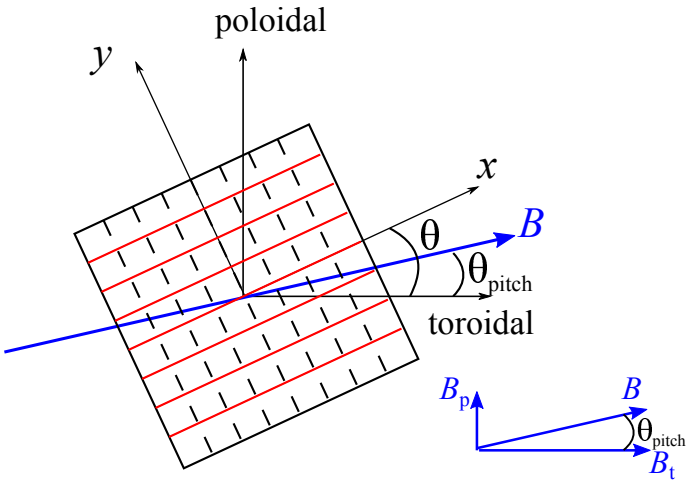

Fig. 3.8: Pick-up coil 1 oriented at angle θ. The square is the core of pick-up coil 1. Black dashed lines: windings of pick-up coil 1-1, wound perpendicular to the x axis. Red lines: windings of pick-up coil 1-2, wound perpendicular to the y axis. . The blue arrow indicates the directions of $\boldsymbol{B}$, The toroidal and poloidal components $B_{\rm t}$ and $B_{\rm p}$ are shown in the lower right diagram. $\theta_{\rm pitch}$ is the pitch angle of $\boldsymbol{B}$ ($\theta_{\rm pitch} = \tan^{-1}(B_{\rm p}/B_{\rm t})$).

Using Eqs. (3.3)–(3.6), the output signals for pick-up coils 1-1 and 1-2 for the case shown in Fig. 3.8 can be written as

$$V_{\text{1-1}} = K_{\text{Bt1-1}}(\theta)B_{\rm t} + K_{\text{Bp1-1}}(\theta)B_{\rm p}, \tag{3.7}$$
$$V_{\text{1-2}} = K_{\text{Bt1-2}}(\theta)B_{\rm t} + K_{\text{Bp1-2}}(\theta)B_{\rm p}, \tag{3.8}$$

where $V_{\text{1-1}}$ and $V_{\text{1-2}}$ are the output signals of pick-up coils 1-1 and 1-2, $K_{\text{Bt1-1}}(\theta)$, $K_{\text{Bt1-2}}(\theta)$, $K_{\text{Bp1-1}}(\theta)$ and $K_{\text{Bp1-2}}(\theta)$ are the $B_{\rm t}$ and $B_{\rm p}$ sensitivities for angle θ for each coil, respectively. From Eqs. (3.7) and (3.8), we can calculate $B_{\rm t}$ and $B_{\rm p}$ as

$$B_{\rm t} = \frac{V_{\text{1-1}}K_{\text{Bp1-2}}(\theta) - V_{\text{1-2}}K_{\text{Bp1-1}}(\theta)}{K_{\text{Bt1-1}}(\theta)K_{\text{Bp1-2}}(\theta) - K_{\text{Bp1-1}}(\theta)K_{\text{Bt1-2}}(\theta)}, \tag{3.9}$$
$$B_{\rm p} = \frac{V_{\text{1-1}}K_{\text{Bt1-2}}(\theta) - V_{\text{1-2}}K_{\text{Bt1-1}}(\theta)}{K_{\text{Bp1-1}}(\theta)K_{\text{Bt1-2}}(\theta) - K_{\text{Bt1-1}}(\theta)K_{\text{Bp1-2}}(\theta)}.-, \tag{3.10}$$

From the calculated $B_{\rm t}$ and $B_{\rm p}$ (Eqs. (3.9) and (3.10)), $\theta_{\rm pitch}$ is calculated. In the test of Fig. 3.7, we measured the sensitivity of each pick-up coil to the magnetic field. In order to calibrate the absolute sensitivity, we also performed a test with only the PF coil energized. Dozens of pick-up coils are located on the inside of the vacuum vessel wall as shown in Fig. 1.13(b), and the Rogowski probe is located at $Z = 0$ m. We compared the signals measured by pick-up coil 1 and pick-up coils located at (R, Z) = (0.7 m, 0.07 m) and (0.7 m, −0.07 m). The test result is shown in Fig. 3.9. Pick-up coil 1 was located at $R = 0.7$ m and θ was set to 17.5°. $B_{\rm p}$ was calculated using the parameters determined from sensitivity calibration shown in Table. 3.1 and Eq. (3.10). Good agreement was obtained in measured magnetic fields,and the uncertainty in the absolute sensitivity is estimated to be within 3%.

Next, we checked the B_p signal measured in typical plasma discharges. The result is shown in Fig. 3.10. In each case B_p measured by pick-up coils almost agreed but small differences were observed. In the test shown in Fig. 3.9, only the PF3 coil was energized and the magnetic field in the region around the pick-up coils was nearly uniform. In the case shown in Fig. 3.10, B_p is produced by the plasma current I_p, PF coil current and the eddy currents flowing in the vacuum vessel. In this case, the magnetic field in the region around the pick-up coils is not uniform. This is believed to be the reason for the small differences in the measured B_p seen in Fig. 3.10.

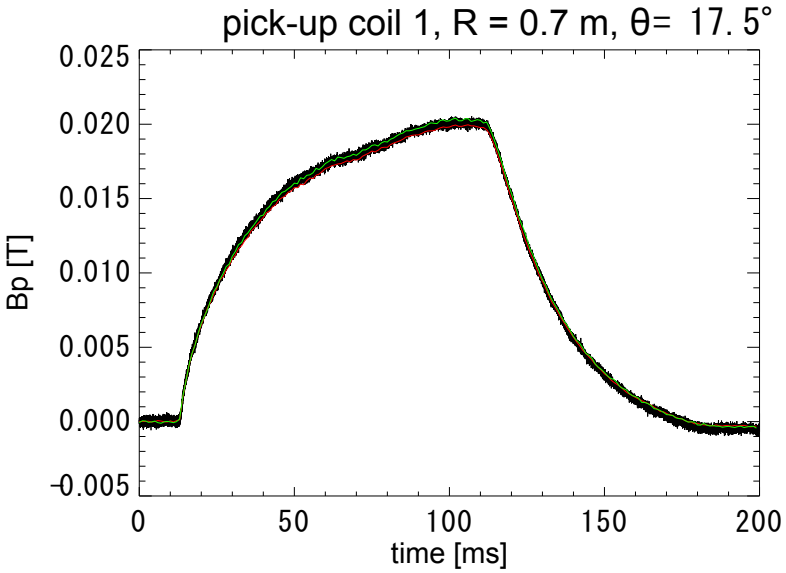

Fig. 3.9: Comparison of measured B_p when only the PF coil was energized. Black: B_p measured by pick-up coil 1 on the Rogowski probe with $\theta = 17.5$ °. Red and green: B_p measured by pick-up coils located at $(R, Z) = (0.7\text{ m}, 0.07\text{ m})$ and $(0.7\text{ m}, -0.07\text{ m})$.

Lastly, we evaluated the accuracy of the θ_{pitch} measurement. As shown in Fig. 3.7, with only the TF coil energized, measurements were made by changing θ on a shot by shot basis. Since there is no B_p in this test, the measured θ_{pitch} should be 0°. The time evolution of the measured θ_{pitch} is shown in Fig. 3.11. θ_{pitch} was calculated using Eqs. (3.9) and (3.10) and averaged over 1 ms. The error for the measurement is estimated to be within $\pm 0.25°$ for both pick-up coils 1 and 3.

Based on the calibration results described in this section, we conclude that the measurement of the magnetic field using the pick-up coils on the Rogowski probe is reliable.

3.4 Open vs. closed hole experiment

In Sec. 2.5, a typical signal of the Rogowski coil was shown. In order to evaluate the signal to noise ratio (S/N) of the Rogowski coil, signals obtained with the hole of the Rogowski coil open and closed were compared. As described in Chap. 2, an unideally fabricated Rogowski coil has sensitivities to external magnetic fields. In addition, a Rogowski coil can be sensitive to electrostatic noise (i.e., capacitive electrostatic coupling) [75] due to plasma potential fluctuation. From the closed hole experiment, we can evaluate the total noise due to external magnetic fields and electrostatic noise. A comparison between the signal of Rogowski coil 1

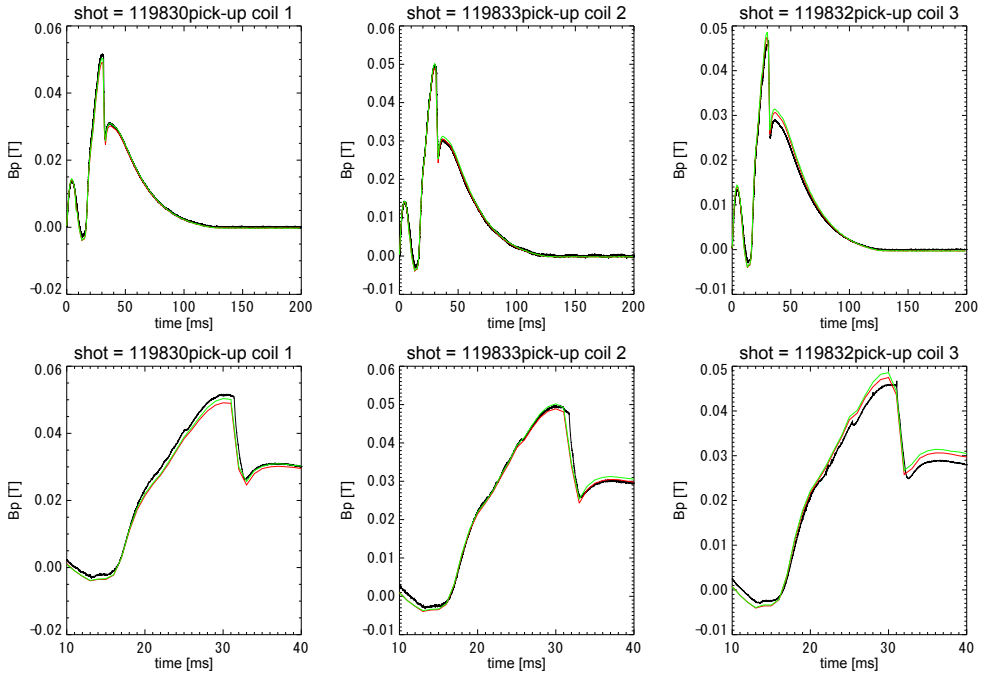

Fig. 3.10: Comparison of measured $B_{\rm p}$ for a typical plasma discharge. Black: $B_{\rm p}$ measured by pick-up coils on the Rogowski probe. Red and green: measured by pick-up coils located at $(R,\, Z) = (0.7\ {\rm m},\, 0.07\ {\rm m})$ and $(0.7\ {\rm m},\, -0.07\ {\rm m})$.

with the hole open and closed is shown in Fig. 3.12. The hole direction θ was set to be 0° (see. Fig. 3.2). In this experiment, good discharge reproducibility was obtained. As shown in Fig. 3.12(b), the signal of Rogowski coil 1 for the case with the hole closed was very small. This test was repeated at several values of θ. When the signal is averaged over 1 ms, the noise level is less than 5 kA/m^2. Since a typical signal level for j is 100 kA/m^2, the present S/N is greater than 20.

3.5 Angular dependence of Rogowski coil sensitivity

The direction of the hole of the Rogowski probe can be rotated in toroidal-poloidal plane. Therefore, the dependence of the Rogowski coil signal on the angle between the hole direction and the magnetic field direction can be measured. Hereafter, we call this dependence the angular dependence of current density j. The center of Rogowski coil 1 was located inside of the LCFS (Last closed flux surface, at $R = 515.5$ mm). The current densities measured in several θ cases are shown in Fig. 3.13. The symmetric inversion for 0° and 180° was obtained and the offset in the measurement is negligible. The signal for 15° is larger than that at 0°, and this is the effect of the finite pitch angle of the current density $\theta_{\rm j}$.

By changing θ on a shot by shot basis, the angular dependence of j can be measured (Fig. 3.14). The black symbols are the measured data points at $t = 26$ ms (averaged over 1 ms). From Fig. 3.14(a), the angular dependence from −10° to 40° is clearly inverted from the angular dependence from 170° to 220°. When the angular dependence is measured over many discharges, it is important to confirm the reproducibility of the plasma. In this experiment, macroscopic parameters such as $I_{\rm p}$, $B_{\rm t}$, and $B_{\rm p}$ are reproduced to within 1%–2%. In the

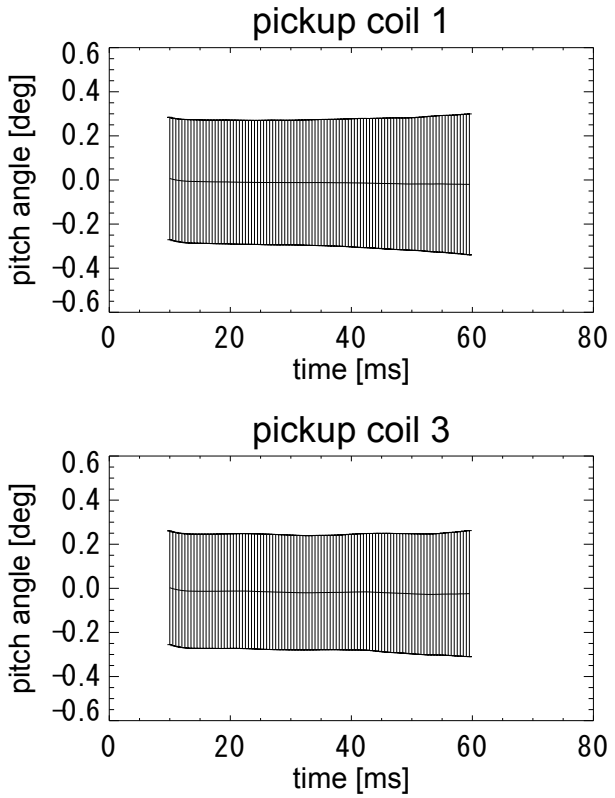

Fig. 3.11: Test of the θ_{pitch} measurement. Data points are averaged over 24 shots for the test. Error bars show the scatter of the mean value.

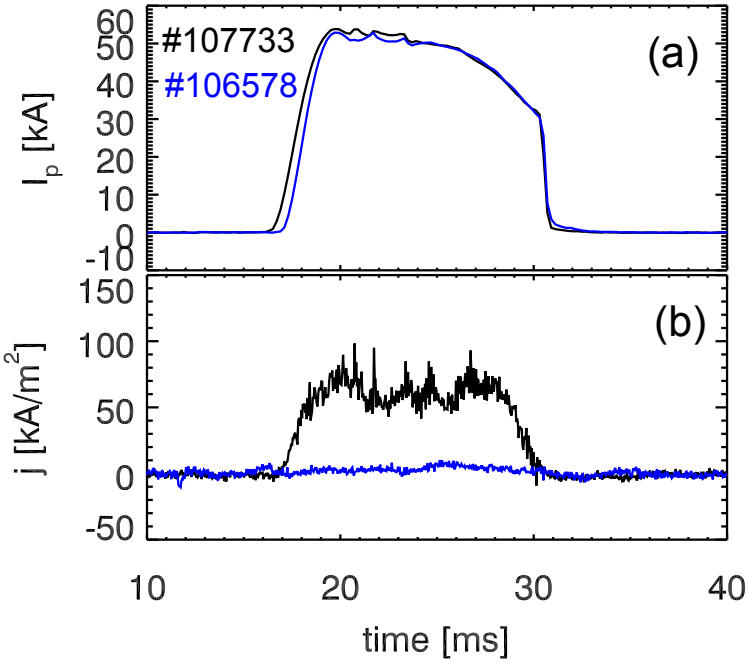

Fig. 3.12: Comparison of the Rogowski coil signal with the hole open (black) and closed (blue). (a) I_p , and (b) j measured by Rogowski coil 1 [74].

expanded view shown in Fig. 3.14(b) ($-20°$ to $60°$), several data points at the same angle are shown, with scatters of 5%-20%. These scatters are larger than the noise level evaluated in Sec. 3.4.

In Fig. 3.14(b), the measured angular dependence were fitted by a Gaussian function (blue). The scatters of the Rogowski coil signals of 10% were used for the fitting weights. The systematic error was also considered. From the peak location of the fitted Gaussian function, the j pitch angle, θ_j, can be determined. Since the depth of the hole is 26 mm, the angular dependence deviates from the cosine shape. A geometrical dependence was obtained by calculating the projected cross sectional area of the hole (green curve in Fig. 3.14(b)) using the equation $S(\theta) = 2a2\cos\theta(\psi - \sin(2\psi)/2)$ where $\psi = \arccos(d\tan\theta/2a)$ (a is the radius of the hole, θ is the angle between the axis of the hole and the magnetic field line, and d is the height of the cylinder). $S(\theta)$ in Fig. 3.14(b) is shifted horizontally, and expanded vertically to fit the experimental profile. In this calculation, a finite sheath potential effect is not taken into account.

Figure 3.15 shows the relationship between the magnetic field pitch angle θ_B measured by the pick-up coil 2 and θ_j measured by Rogowski 1. In these discharges, the difference of θ_B between radial positions of the Rogowski 1 and the pick-up coil 2 is less than $1°$. When there is a finite pressure gradient ∇p, θ_B and θ_j must be slightly different each other to satisfy $\boldsymbol{j} \times \boldsymbol{B} = \boldsymbol{\nabla} p$. Since near the LCFS in low field side, the pressure gradient force ($-\boldsymbol{\nabla} p$) directs outward so the electromagnetic force $\boldsymbol{j} \times \boldsymbol{B}$ must direct inward. Thus, θ_B can be slightly larger than θ_j. A possible angular difference is less than $1°$ for this case from EFIT calculation.

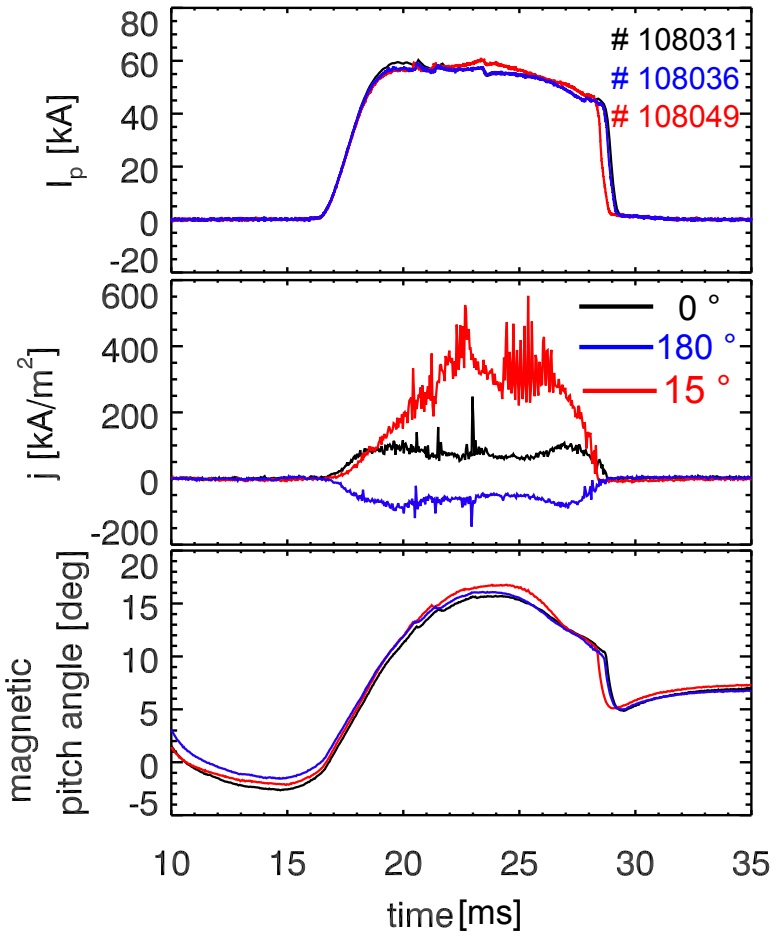

Fig. 3.13: Comparison of Rogowski coil signals for $\theta = 0°$, 180° and 15°. (a) I_p , (b) j measured by the Rogowski coil, and (c) magnetic field pitch angle [74].

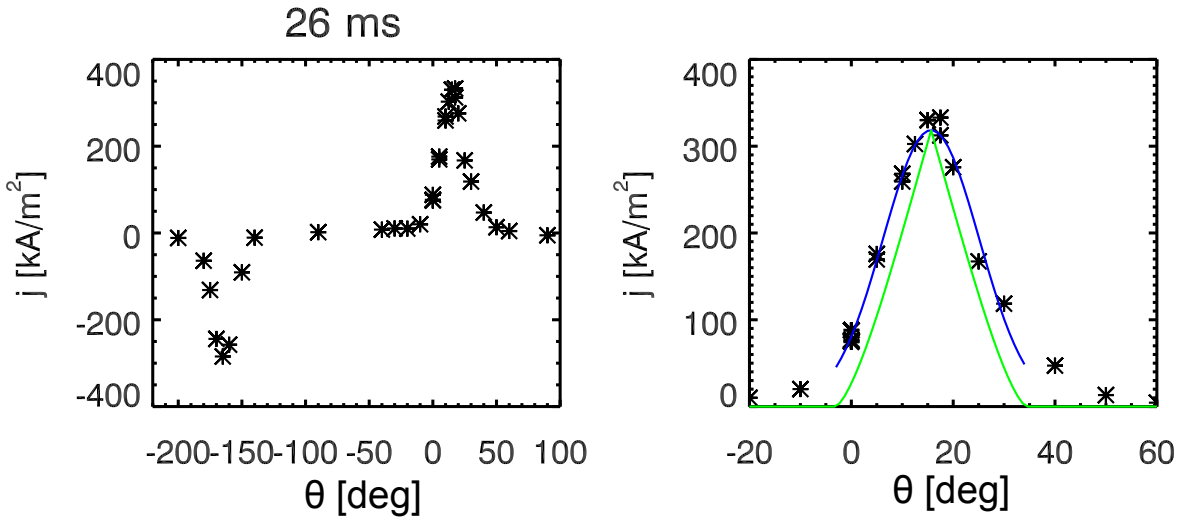

Fig. 3.14: Angular dependence of j (a) and expanded view with a fitted curve (blue) and a geometrical geometrical dependence (green) (b) [76].

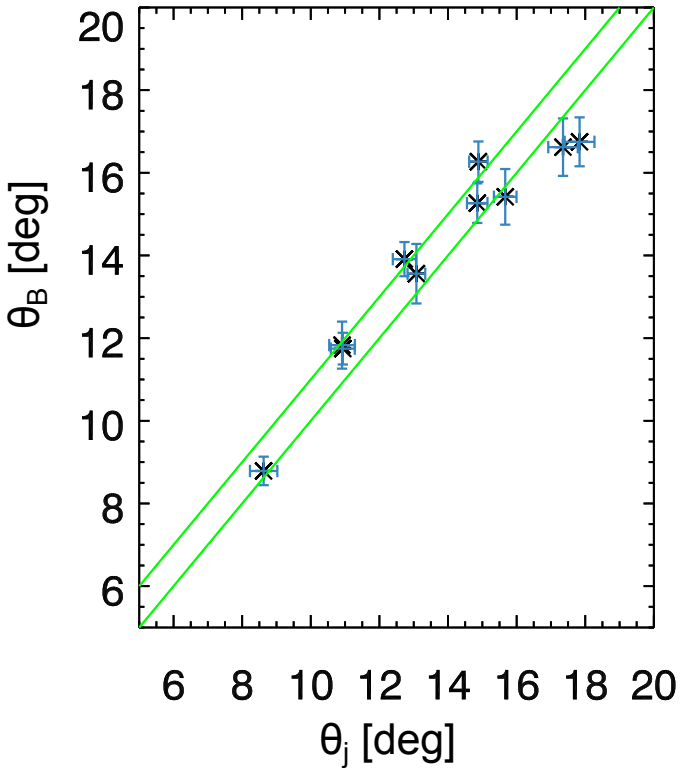

Fig. 3.15: Magnetic field pitch angle θ_B vs. current density pitch angle θ_j. Lines indicating 0° and 1° difference between θ_B and θ_j are also shown [74].

3.6 Electrostatic noise test

A Rogowski coil can have a sensitivity to electrostatic noise [75]. Since there are electrostatic potential fluctuations in the plasma, it is possible for a Rogowski coil signal to be affected by electrostatic noise. If the sensitivity to noise is large, the noise can mistakenly be identified as current fluctuations. Thus, it is important to check the sensitivity to noise. In order to estimate the signal (current fluctuation) to noise (electrostatic potential fluctuation) ratio, two kinds of the noise tests were performed. Photos of the test setups are shown in Fig. 3.16. In (a), a tin foil stick was placed inside the hole. In (b), the probe head was covered by a tin

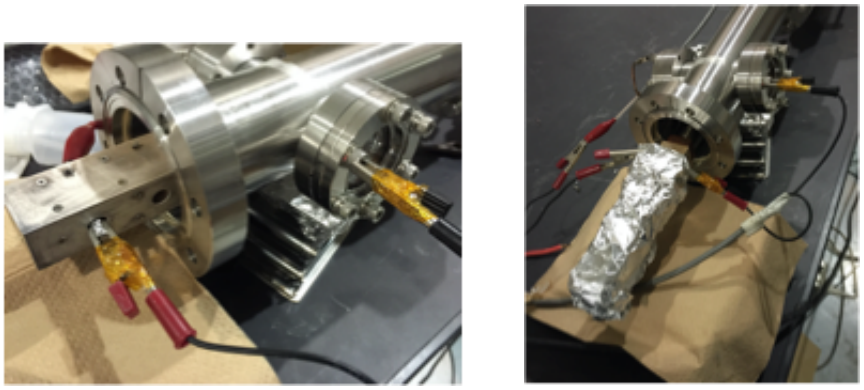

Fig. 3.16: Electrostatic noise tests for the Rogowski coils (Rogowski 1 and Rogowski 2). (a) Test I for inside the hole, and (b) Test II for outside the probe head.

foil.

In these tests, the main frame of the probe was grounded, and the frequency responses of the Rogowski coils (Rogowski 1 and Rogowski 2) to the applied voltage between the tin foils and the ground were measured. The test results are shown in Fig.3.17. K_{ele} is the sensitivity to electrostatic noise, V_{out} is the output signal of the Rogowski coil and V_{applied} is the amplitude of the applied voltage. From Fig. 3.17, the sensitivity to electrostatic noise of Rogowski coils are up to 2.4×10^{-9} $V_{\mathrm{out}}\mathrm{second}/V_{\mathrm{applied}}$. From the noise test, we need to estimate S/N of the Rogowski coils to electrostatic noise. In this case, we can define S/N as

$$S/N = \frac{K_{\mathrm{current}} I}{K_{\mathrm{ele}} V_{\mathrm{applied}}}, \tag{3.11}$$

where K_{current} is the sensitivity of the Rogowski coil to the current passing through the hole. Examples of S/N given by Eq. (3.11) for several currents are shown in Fig. 3.18.

In TST-2 Ohmic plasmas, a typical potential fluctuation near the plasma edge is up to ± 50 V. From Fig. 3.19, we can see that the amplitude of current fluctuation is greater than ± 5 A, so S/N can be estimated to be greater than 20 from Fig. 3.18. In addition, the current measured by Rogowski coil 1 and the current deduced from magnetic fields measured by pick-up coils 1 and 2 agreed with each other (see Fig. 3.19 black and red traces). This result ensures the accuracy of the measurement and confirms the existence of a large local current fluctuation.

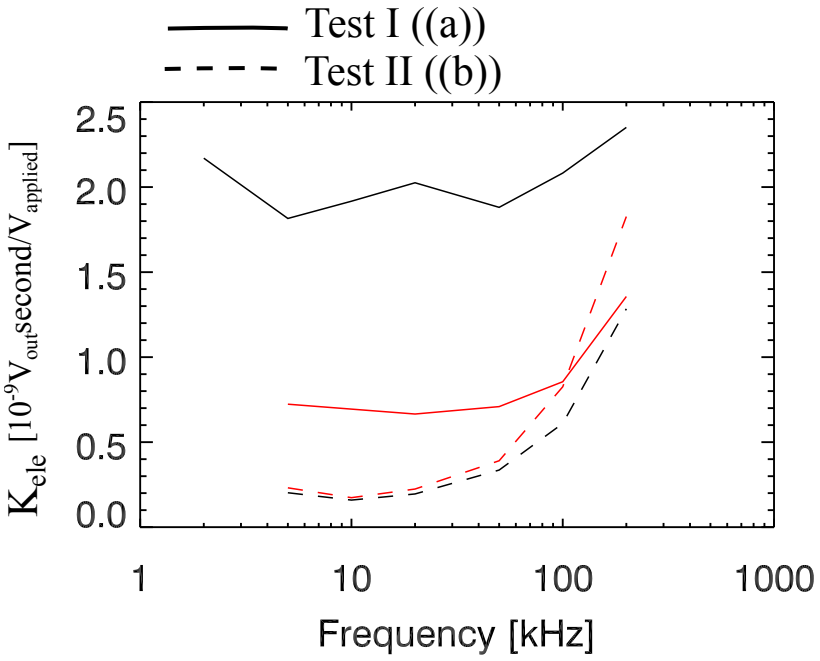

Fig. 3.17: The result of electrostatic noise tests. Black and red solid lines are the results of Test I for Rogowski 1 and Rogowski 2. Black and red dashed lines are the results of Test II for Rogowski 1 and Rogowski 2.

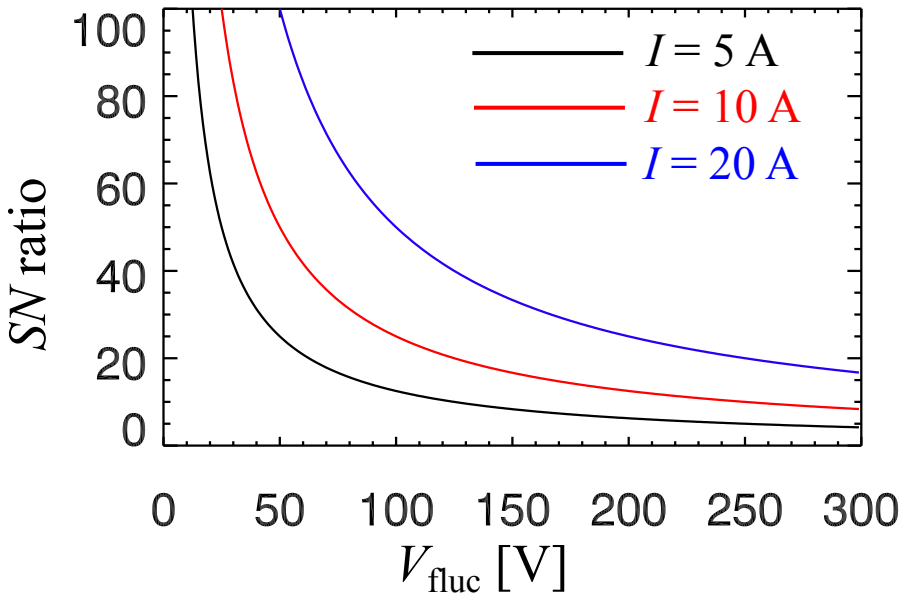

Fig. 3.18: Examples of S/N between the current fluctuation and the potential fluctuation for $I = 5$, 10, 20 A.

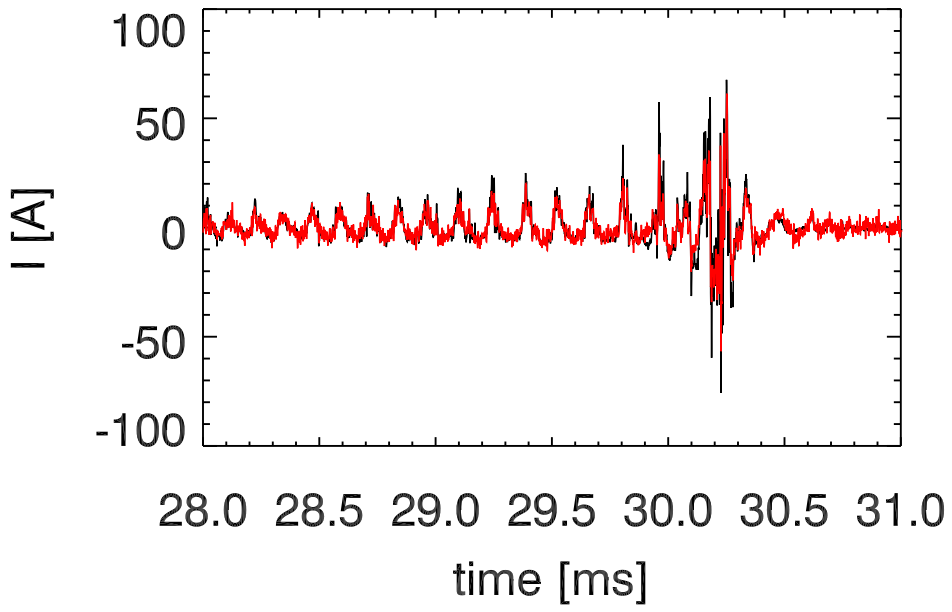

Fig. 3.19: Typical current signals measured by Rogowski 1 (black) and that deduced from pick-up coils 1 and 2 (red). For time integration, analog integrators with a time constant of 1 ms were used.

Chapter 4

Plasma sheath effect

4.1 The sheath model

In previous sections, we presented the results of current density measurement, and it was found that the sensitivities to external magnetic fields and electrostatic potential fluctuation are sufficiently small compared to the current signal of the Rogowski coil. As discussed in Chap. 3, one uncertainty for the diagnostic remains: the plasma sheath effect. Since the current is carried by electrons which pass through the hole of the Rogowski coil, it is possible that their orbits are affected by the sheath potential in the vicinity of the Rogowski probe head. The sheath is formed near the insulating material that protects the probe head. In order to investigate the sheath effect on the diagnostic, we consider a sheath model and calculate electron orbits numerically under the influence of a given sheath potential. First, we describe the numerical calculation in detail.

The Rogowski coil is located inside the probe head, and is covered by ceramic shields. Figure 4.1 shows a schematic drawings of the Rogowski probe. The Rogowski coil is indicated by the hatched region. The Rogowski probe can be moved along the major radius of the tokamak, and can be rotated around the shaft axis (in the toroidal-poloidal plane). This allows the measurements of the radial profile and the angular profile of the current. Figure 4.2 shows the definition of the (x, y and z) coordinate system and the angle θ. The z axis is the symmetry axis of the Rogowski coil, and the y axis is in the direction of the major radius. θ is the angle between the z axis and the direction of the magnetic field $\boldsymbol{B}$ (defined by the toroidal and poloidal components B_t and B_p).

Here, we introduce a sheath model. Since the sheath is affected by the angle between the magnetic field and the material surface, we should divide the plasma region into three regions, and use different functions in each region. The definitions of the three regions: Regions I, II and III are shown in Fig. 4.3. r_hole and t are the radius of the hole (4.6 mm) and the thickness of the Rogowski probe (27 mm). Black dots in the front view and the side view represent the target point (r, z) where we calculate the sheath potential. Δr and Δz are the coordinates used to express the functions of the sheath potential, and are given as $\Delta r = r_\mathrm{hole} - r$ and $\Delta z = -t/2 - z$ (for $z \leq -t/2$) or $\Delta z = z - t/2$ (for $z \geq t/2$). A, B, C and D are the points used in Sec. 4.2.

Generally, the sheath consists of the Debye sheath and the presheath which accelerates ions from 0 velocity to the acoustic velocity. In a tokamak plasma discharge, several kinds of presheath should be considered, such as the magnetic presheath [77], collisional presheath and collisionless ptesheath [78]. The magnetic presheath length is estimated to be of the order of ion Larmor radius [77], and it depends on the angle between $\boldsymbol{B}$ and the wall [77].

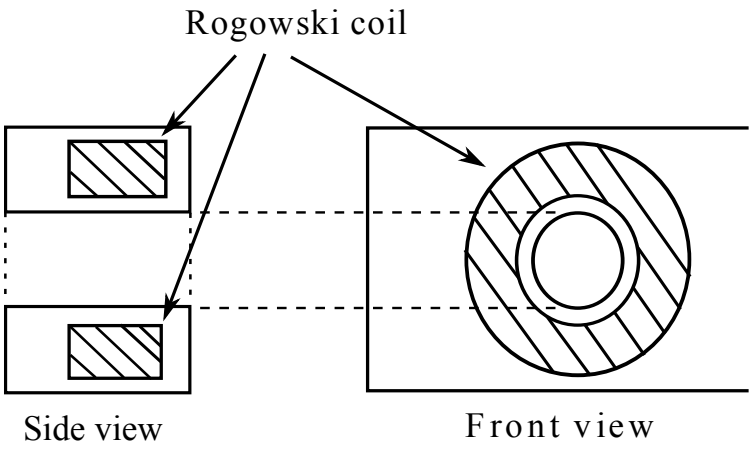

Fig. 4.1: Rogowski coil inside the Rogowski probe head.

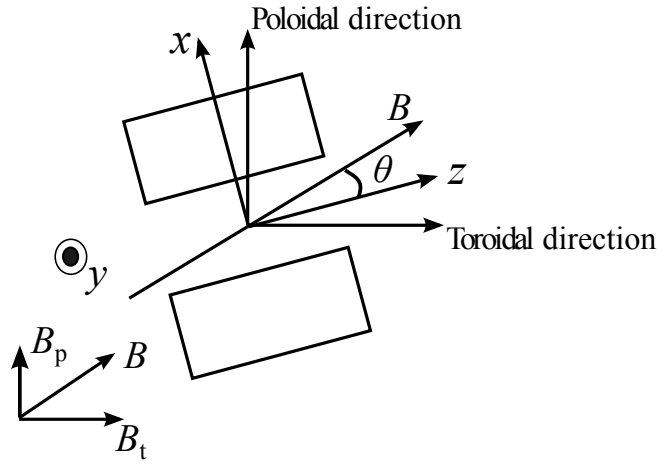

Fig. 4.2: The definition of the coordinates (x, y, z) and the angle of θ.

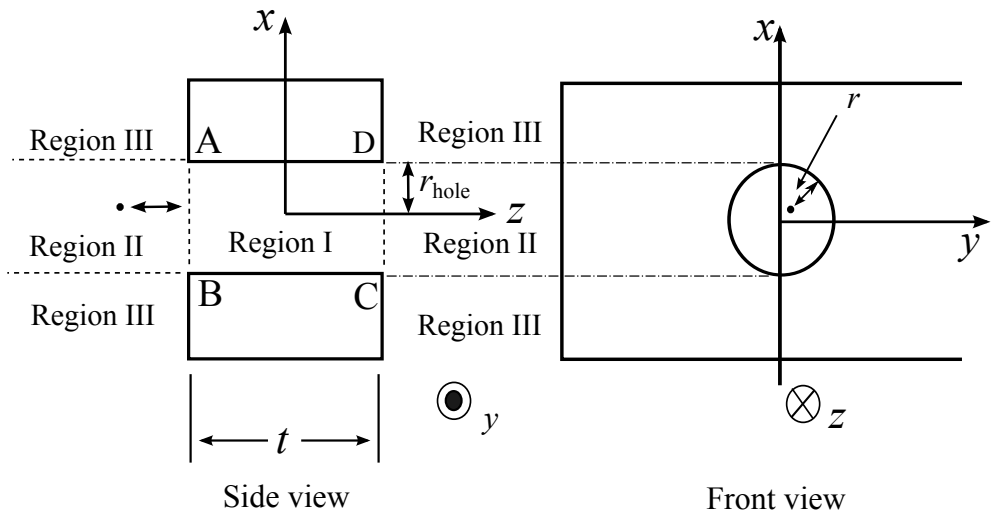

Region I $|z| \leqq t/2$ and $r \leqq r_{hole}$ $(r = (x^2 + y^2)^{0.5})$,
Region II $z > t/2$ or $z < -t/2$ and $r \leqq r_{hole}$,
Region III $z > t/2$ or $z < -t/2$ and $r > r_{hole}$.

Fig. 4.3: Definitions of Regions I, II and III for the sheath model, and representative points A, B, C and D.

In TST-2 Ohmic plasmas, the ion Larmor radius is about 2 mm which is comparable to $r_{\rm hole}$ (4.6 mm).

The sheath model for the orbit calculation, including the angular dependence of the magnetic presheath, was constructed referring to the analytical sheath equation consisting of the Debye sheath and the magnetic preseath [79]. The potentials in Region I, II and III are written as

$$V_{\rm Region\ I}(\Delta r) = V_1 \exp\left(-\frac{\Delta r}{2\lambda_{\rm d}}\right) + V_1 \exp\left(-\frac{\Delta r}{r_{\rm i} + L_{\rm s}}\right), \tag{4.1}$$

$$V_{\rm Region\ II}(\Delta r, \Delta z) = V_1 \exp\left(-\frac{\sqrt{\Delta r^2 + \Delta z^2}}{2\lambda_{\rm d}}\right) + V_2 \exp\left(-\sqrt{\left(\frac{\Delta r}{r_{\rm i} + L_{\rm s}}\right)^2 + \left(\frac{\Delta z}{\rho_{\rm i}\sin\theta + L_{\rm s}}\right)^2}\right), \tag{4.2}$$

$$V_{\rm Region\ III}(\Delta z) = V_1 \exp\left(-\frac{\Delta z}{2\lambda_{\rm d}}\right) + V_2 \exp\left(-\frac{\Delta z}{\rho_{\rm i}\sin\theta + L_{\rm s}}\right). \tag{4.3}$$

where $V_{\rm Region\ I,\ II,\ III}$ are the sheath potentials in Regions I, II and III, respectively, $\lambda_{\rm d} = \sqrt{\epsilon_0 T_{\rm e}/n_{\rm e}e}$ is the Debye length, $\rho_{\rm i}$ is the ion Larmor radius, $L_{\rm s}$ is the length of the collisionless presheath [78], and $r_{\rm i}$ is the magnetic presheath length whose order is the same as $\rho_{\rm i}$. The definition of $r_{\rm i}$ is given later. In Ref. [78], the equation for the collisionless presheath length is introduced [Eq. (39), $L_{\rm s} = \left(\sqrt{2}/3(\sqrt{1-2\phi_{\rm W}}-2)^{\frac{3}{2}} + 2\sqrt{2}(\sqrt{1-2\phi_{\rm W}}-2)^{\frac{1}{2}}\right)\lambda_{\rm d}$, where $\phi_{\rm W}$ is the normalized wall potential]. Since the collisional term is very small in TST-2 Ohmic plasmas, it is ignored in this sheath model. The sheath potential at the wall surface ($\Delta r = 0$ in Region I, $\Delta r = 0$ and $\Delta z = 0$ in Region II, and $\Delta z = 0$ in Region III) is set to be equipotential. Hereafter, we express the potential at the wall surface as $V_{\rm wall}$.

The values of V_1 and V_2 in Eqs. (4.1)–(4.3) must be determined somehow. In Ref. [80], a parameter $f_{\rm d}$ which quantifies the contribution of the Debye sheath term is introduced as

$$f_{\rm d} = 1 - \frac{V_{\rm Region\ I}(6\lambda_{\rm d})}{V_{\rm Region\ I}(0)}. \tag{4.4}$$

For given $f_{\rm d}$ and $V_{\rm Region\ I}(0)$, we can determine V_1 and V_2 using Eq. (4.1). These values are used in Eqs. (4.2) and (4.3). With the decrease of $f_{\rm d}$, the contribution of the presheath increases.

The parameters $r_{\rm i}$ and $\rho_{\rm i}\sin\theta$ represent the angular dependence of the magnetic presheath length. When $\boldsymbol{B}$ is parallel to the wall, the magnetic presheath length cannot be defined accurately [81]. In our sheath model, the magnetic presheath length was set to $\rho_{\rm i}$ for the parallel case. Thus, in Region Ⅲ, it is given by $\rho_{\rm i}\sin\theta$. On the other hand, in Region I and Region Ⅱ, the situation is more complicated. Figure 4.4 shows the angle ϕ between the wall surface and $\boldsymbol{B}$. In these Regions, the magnetic presheath depends on ϕ, which can be

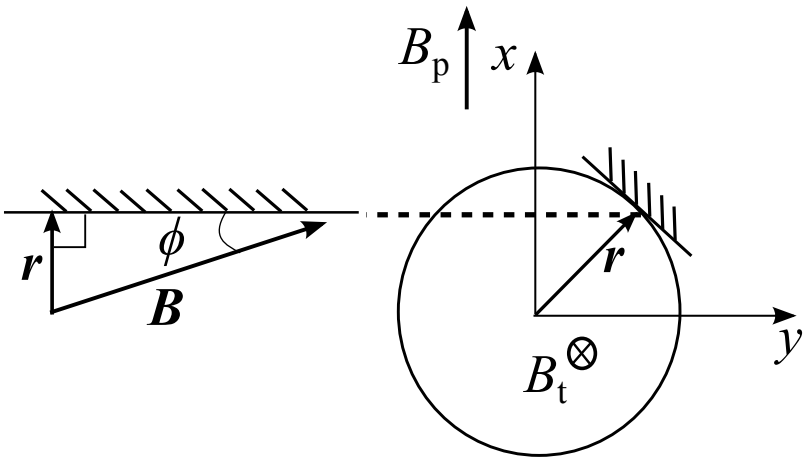

Fig. 4.4: Angle between $\boldsymbol{B}$ and the probe wall in Region I and Region Ⅱ.

calculated using $\boldsymbol{r}$ and $\boldsymbol{B}$. Thus, each set of $\boldsymbol{B}$ and $\boldsymbol{r}$ have different ϕ and different presheath length when θ is finite. $r_{\rm i}$ is defined to include the ϕ dependence as

$$\phi = \frac{\pi}{2} - \cos^{-1}(\hat{\boldsymbol{r}}\cdot\hat{\boldsymbol{B}}) \tag{4.5}$$

$$= \frac{\pi}{2} - \cos^{-1}\left(\frac{x}{\sqrt{x^2+y^2}}\sin\theta\right), \tag{4.6}$$

$$r_{\rm i} = \rho_{\rm i}\left(1 - 2\sin^2\frac{\theta}{2}\sin^2\phi\right). \tag{4.7}$$

Equation (4.7) indicates that $r_{\rm i}$ decreases monotonically with the increase of ϕ. In the case of $\theta = 0$, $r_{\rm i}$ is equal to $\rho_{\rm i}$ for any set of $\boldsymbol{B}$ and $\boldsymbol{r}$. In the region $-r_{\rm hole} \le x \le r_{\rm hole}$ and $y = 0$, $r_{\rm i}$ is equal to $\rho_{\rm i}\cos\theta$. In the region $-r_{\rm hole} \le y \le r_{\rm hole}$ and $x = 0$, $r_{\rm i}$ is equal to $\rho_{\rm i}$ for any θ.

Examples of $V_{\rm Region\ I}$ given by Eq. (4.1) is shown in Fig. 4.5. Near $r = r_{\rm hole}$, the contribution of the Debye sheath is dominant and the electric field is quite large. With the decrease of $f_{\rm d}$, the contribution of the presheath increases. Figure 4.6(a) shows a contour plot of the sheath potential in the y-x plane. Contour shape reflects the angular dependence expressed by Eq. (4.7). For $\theta = 0°$, the shape is axially symmetric (i.e., circles). A smooth

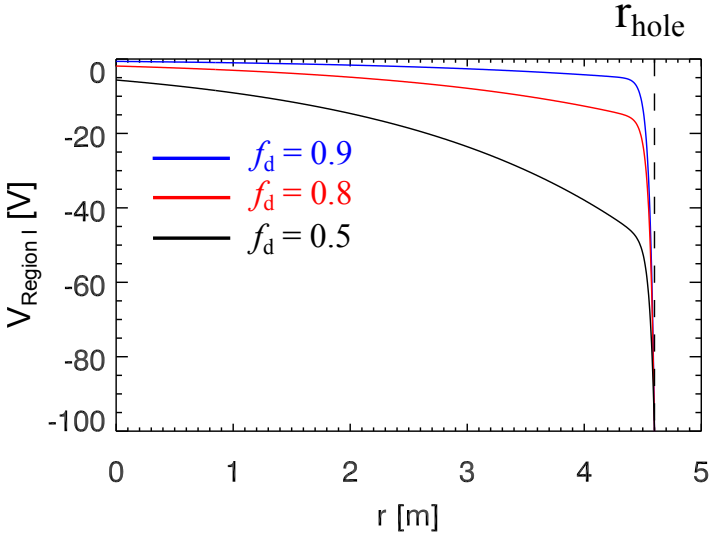

Fig. 4.5: Potential given by Eq. (4.1) as a function of r. $V_{\rm wall}$, θ, $\lambda_{\rm d}$, $\rho_{\rm i}$ and $L_{\rm s}$ were set to be -100 V, 0°, 20 μm 1.5 mm and 0.1 mm, respectively . Black, red and blue curves show $V_{\rm Region\ I}$ for the cases with $f_{\rm d} = 0.5$, 0.8, and 0.9. (V_1, V_2) for the black, red, and blue curves are (-49.53 V, -50.47 V), (-83.16 V, -16.84 V), and (-94.37 V, -5.63 V). Dashed line shows the location of $r_{\rm hole}$ (4.6 mm).

transition from Region I to Region III can be seen in Fig. 4.6(b). In the x-z plane, there are no large differences between the shapes for cases with different θ.

4.2 Electron orbit calculation

For orbit calculation, Newmark's beta method was used to solve the equation of motion $m_{\rm e} d\boldsymbol{v}/dt = -e(\boldsymbol{E} + \boldsymbol{v} \times \boldsymbol{B})$ under a given magnetic field $\boldsymbol{B}$ and a sheath electric field. The $\boldsymbol{\nabla} B$ drift and the curvature drift are included in the calculation ($B = B_0 \frac{R_0}{R}$, where R is the major radius in the tokamak, R_0 is the radial location of the center of the hole, and B_0 is the magnetic field strength at R_0). Normally, the time steps for the calculation are set to $\frac{0.1}{f_{\rm ce}}$ and $\frac{0.002}{f_{\rm ce}}$ for low energy electrons and high energy electrons, respectively, where $f_{\rm ce}$ is the electron cyclotron frequency. Low and high energy electrons are those with kinetic energy lower or higher than $|-eV_{\rm wall}|$. In addition, $\boldsymbol{E}$ and $\boldsymbol{\nabla} E$ could be large when Δr, Δz or $\sqrt{\Delta r^2 + \Delta z^2}$ is small. Thus, in the regions where Δr, Δz or $\sqrt{\Delta r^2 + \Delta z^2}$ is smaller than $10\lambda_{\rm d}$, the time step is set 100 times smaller than the normal time step.

In the absence of a sheath potential, an electron exhibits a parallel motion along the magnetic field when we can neglect the finite Larmor radius. Therefore, the condition for an electron to pass through the hole depends on whether the field line penetrates through the hole. In such a case, the sensitivity of the Rogowski coil depends on the hole geometry and the relative angle θ between the field line direction and the hole direction. The dependence of the sensitivity on θ can thus be calculated. Hereafter, the angular dependence of this sensitivity is referred to as the geometrical curve. However, when we consider the $\boldsymbol{E} \times \boldsymbol{B}$ drift due to the sheath electric field, the electron orbit is changed and the sensitivity becomes different from the geometrical curve.

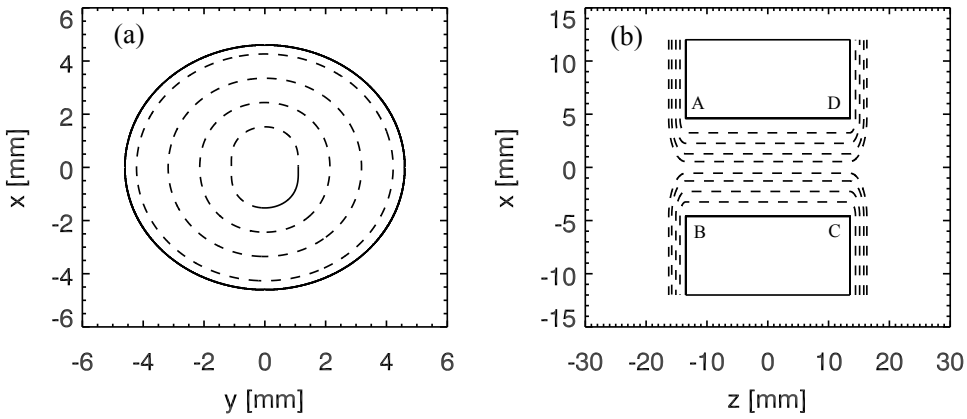

Fig. 4.6: Contour plots of the sheath potential for $\theta = 35°$ (dashed curves). $V_{\rm wall}$, $\lambda_{\rm d}$, $\rho_{\rm i}$, $L_{\rm s}$ and $f_{\rm d}$ were set to -100 V, 20 μm, 1.5 mm, 0.1 mm and 0.5 respectively. (a) contour plot in the y-x plane, (b) contour plot in the z-x plane.

We show two representative cases: in the first case the electron can pass through the hole geometrically ($\theta = 0°$, Fig. 4.7), and in the second case the electron cannot pass through the hole geometrically ($\theta = 25°$, Fig. 4.8).

Figure 4.7 shows the electron orbit when $\theta = 0°$. The electron was initially located at (x, y, z) = (2.5 mm, -2.5 mm, $-t/2 - \rho_{\rm i}$). The drift along the wall surface is due to the $\boldsymbol{E} \times \boldsymbol{B}$ drift. In this case, $\boldsymbol{E}_\perp$ is finite and $\boldsymbol{E}_\parallel$ is zero. Thus, the guiding center of the electron shows a constant parallel motion with a nearly constant $\boldsymbol{E} \times \boldsymbol{B}$ perpendicular drift.

In Fig. 4.8, an electron orbit when $\theta = 25°$ is shown. The electron was initially located at (x, y, z) = (-3.8 mm, -2.5 mm, $-t/2 - \rho_{\rm i}$). In this case, both $\boldsymbol{E}_\perp$ and $\boldsymbol{E}_\parallel$ are finite. As the electron approaches the wall surface (defined in Sec 4.1), the electron is decelerated due to the sheath potential, and when the parallel velocity is low the electron is reflected near the wall. Near the reflection point (i.e., $\Delta r \approx 0$ mm), the $\boldsymbol{E}_\perp \times \boldsymbol{B}$ drift velocity becomes large. In this region, the z component of the $\boldsymbol{E} \times \boldsymbol{B}$ drift is $E_{\rm y}/B\sin\theta$, and the electron shows a rightward motion as shown in Fig. 4.8(b). As a result, the electron exhibits a zigzag motion between the wall surfaces, and the electron can eventually pass through the hole. The orbit in Fig. 4.8 demonstrates that the measured current can be finite even if the angle θ is larger than that allowed geometrically.

4.3 Angular dependence of the current

A large number of electron orbits were calculated for a given θ. The initial z locations (z_0) were fixed at $-t/2 - \rho_{\rm i}$. In the y-x plane, the initial r locations ($r_0 = \sqrt{{x_0}^2 + {y_0}^2}$) were distributed uniformly using random numbers, with the maximum r_0 set sufficiently larger than $r_{\rm hole}$. The current is carried by the asymmetric component of the electron velocity distribution function. In this calculation, however, the Maxwellien distribution was adopted for the electron initial velocities to investigate the dependence on the typical electron energy. The current is calculated by integrating the initial $v_{\rm z}$ (> 0) of electrons which pass through the hole (i.e., $I = -e \int dx \int dy \int v_{\rm z} f_{v_{\rm z}} dv_{\rm z}$). By calculating the current for various θ, the angular dependence of the current is reconstructed. Figure 4.9 shows a comparison between the angular dependences of data obtained experimentally, the orbit calculation result, and

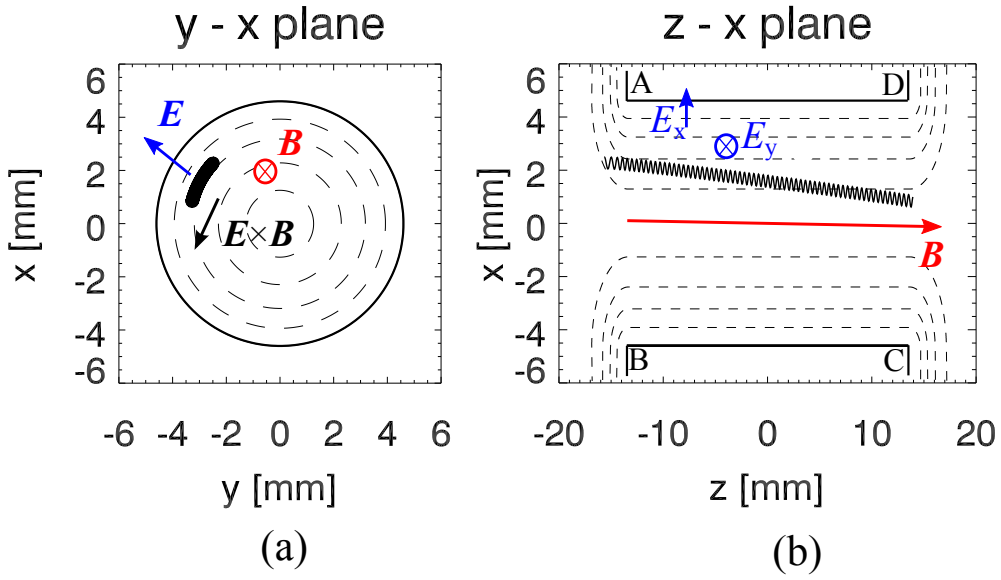

Fig. 4.7: Typical electron orbit when $\theta = 0°$. The thick black circle and the thick black lines in (a) and (b) are wall surfaces. The points A, B, C and D are the same as those in Fig. 4.3. Dotted curves are the sheath contours. Black curves are projections of the electron orbit seen along the z and y axes, respectively. The blue, red and black arrows show the directions of the sheath electric field $\boldsymbol{E}$, the magnetic field $\boldsymbol{B}$ and the $\boldsymbol{E} \times \boldsymbol{B}$ drift.

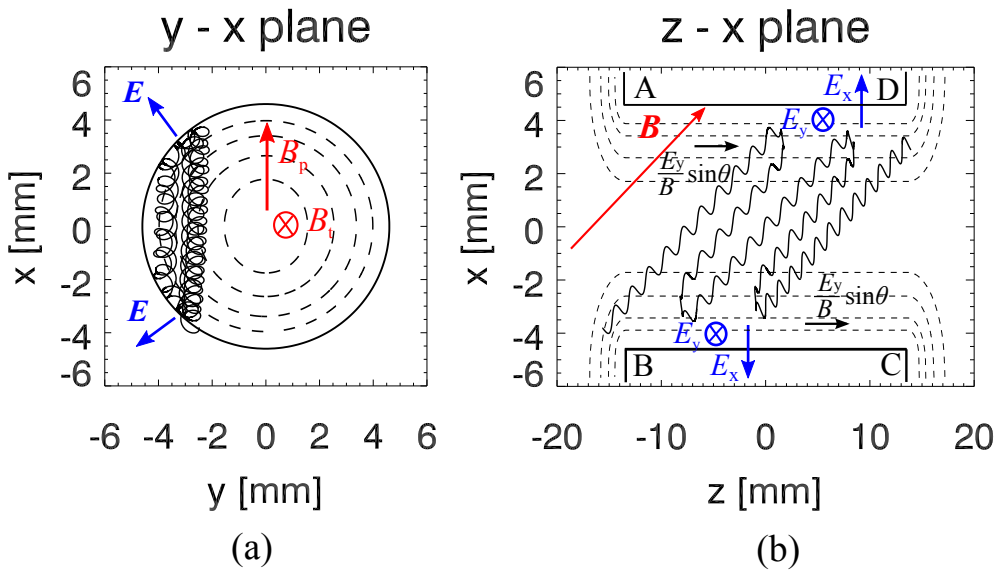

Fig. 4.8: Typical electron orbit when $\theta = 25°$. The thick black circle and the thick black lines in (a) and (b) are wall surfaces. The points A, B, C and D are the same as those in Fig. 4.3. Dotted curves are the sheath contours. Black curves are projections of the electron orbit along from the z and y axes, respectively. The blue, red and black arrows show the directions of the sheath electric field $\boldsymbol{E}$, the magnetic field $\boldsymbol{B}$ and the $\boldsymbol{E} \times \boldsymbol{B}$ drift.

the geometrical curve mentioned in Sec. 4.2.

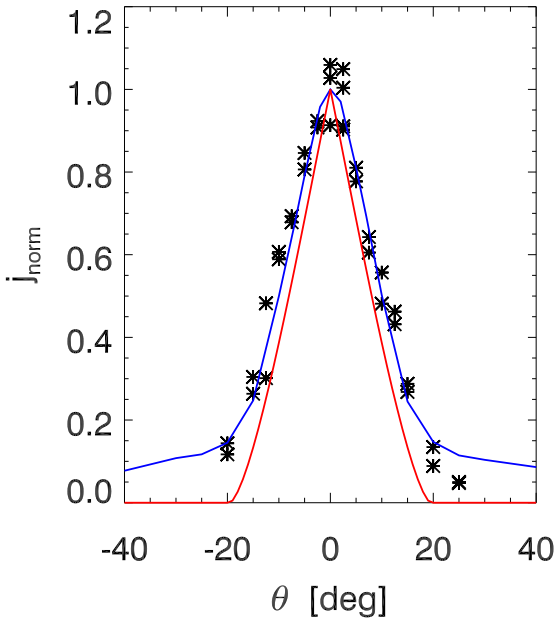

Fig. 4.9: Comparison between angular dependences. Black symbols: experimental data obtained on a shot by shot basis, blue curve: result of orbit calculation, and red curve: geometrical curve expected from the probe geometry [76].

The blue curve in Fig. 4.9 is obtained with the parameters: $\lambda_d = 20$ μm, $L_s = 0.1$ mm, $V_{wall} = -100$ V, $f_d = 0.8$, $T_e = 40$ eV, T_i =10 eV and $B = 0.15$ T. The values used for λ_d, T_e, and B are calculated from the experimentally measured values using the Langmuir probe and the pick-up coils located near the Rogowski coil [74]. In TST-2 Ohmic plasmas, the value of T_i near the plasma edge is in the range 5 to 20 eV. For comparison between measured and calculated dependences, the vertical scale was adjusted so that the peak heights become equal. In the experiment, the current was measured on a shot by shot basis and θ was scanned to obtain the angular dependence. The experimentally obtained result is well reproduced by the orbit calculation, which has a broader width than the geometrical curve (blue). In the calculation, some electrons with the parallel energy higher than $|-eV_{wall}|$ can hit the wall. For that case, we adopted two scenarios: forward elastic scattering and backward elastic scattering, but the results of these scenarios do not show a large difference.

Although we have shown that the width of the angular profile becomes broader due to the sheath potential, we must also consider the electrons repelled by the sheath potential. Here, we discuss the sensitivity at $\theta = 0°$. In this case, all the electrons located in front of the hole can pass through the hole as long as their energies are sufficiently higher than the sheath potential. However, when the electron energy is low, the electron is repelled and cannot pass through the hole. Figure 4.10 shows the initial velocity distribution function (black curve), and that of the electrons which passed through the hole (red curve). In the case of the red curve, the electrons whose energy is lower than $|-eV_{wall}|$ are affected by the sheath electric field. In the case of Fig. 4.10, the current calculated using the blue curve is estimated to be 10% smaller than that calculated using the black curve.

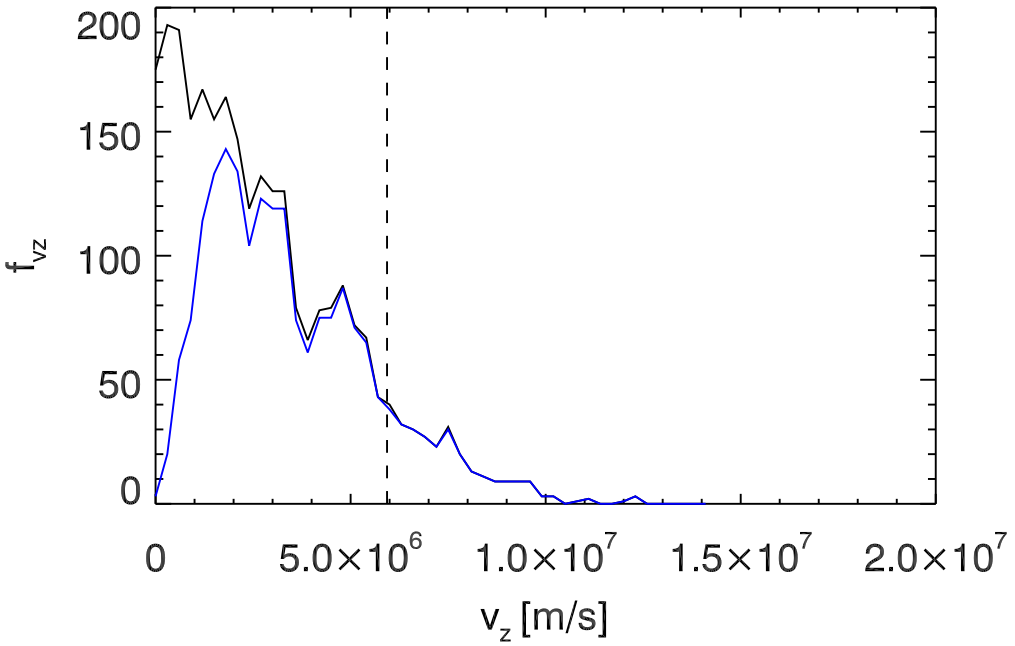

Fig. 4.10: The initial velocity distribution function f_{v_z}. Black: electrons initially located in the region of $\sqrt{x^2+y^2} \leq r_{\rm hole}$, and blue: electrons which passed through the central hole at $\theta = 0°$. Dashed line shows the velocity for an electron with the energy of 100 eV.

4.4 Parameter dependence of the angular dependence

In order to clarify the features of the angular dependence of the current and to understand the physics of the sheath effect, we performed orbit calculations under various conditions. In Secs. 4.1 and 4.2, it was shown that the electron orbit and the height of the angular profile are affected by the $\boldsymbol{E} \times \boldsymbol{B}$ drift due to the sheath electric field $\boldsymbol{E}$ and the sheath potential V. The sheath electric field $\boldsymbol{E}$, the magnetic field strength B and $V_{\rm wall}$ are considered to be important parameters. If $V_{\rm wall}$ is negatively large or the sheath length is large, the fraction of electrons repelled by the sheath potential is also large. $f_{\rm d}$ and $\rho_{\rm i}$ ($T_{\rm i}$) are the parameters that determine the sheath length. $\lambda_{\rm d}$ and $L_{\rm s}$ are negligible since they are much smaller than $\rho_{\rm i}$. In this section, we present the dependences of the angular profile width and the height on $V_{\rm wall}$, $f_{\rm d}$, $\rho_{\rm i}$ ($T_{\rm i}$) and B. $T_{\rm e}$, $\lambda_{\rm d}$, $L_{\rm s}$, $r_{\rm hole}$ and t were set to 40 eV, 20 μm, 0.1 mm, 4.6 mm and 27 mm, respectively. Generally in a plasma, $V_{\rm wall}$ depends strongly on $T_{\rm e}$. However, we proceed with the analysis using a typical electron energy for $T_{\rm e}$, which is independent of $V_{\rm wall}$.

Figure 4.11 shows the dependences of the angular profile width on different parameters. The width is defined as the $1/e$ width of the fitted Gaussian curve obtained from the measured data points larger than 20% of the maximum value. Dashed lines indicate the width of the geometrical curve. The dependences on $V_{\rm wall}$, $f_{\rm d}$ and $T_{\rm i}$ (Figs. 4.11(a), (b) and (c)) are weak and nearly constant. In Fig. 4.11(b), calculations were performed only for the range $0.5 < f_{\rm d} < 0.9$, because other cases such as $f_{\rm d} = 0$ (presheath dominant case) and $f_{\rm d} = 1$ (no presheath) are impractical. In Fig. 4.11(d), a clear dependence on B can be seen. This result suggests that the broadening of the width is quite sensitive to the $\boldsymbol{E} \times \boldsymbol{B}$ drift. Since the drift velocity is proportional to E, dependence on $V_{\rm wall}$ was expected, but we cannot see

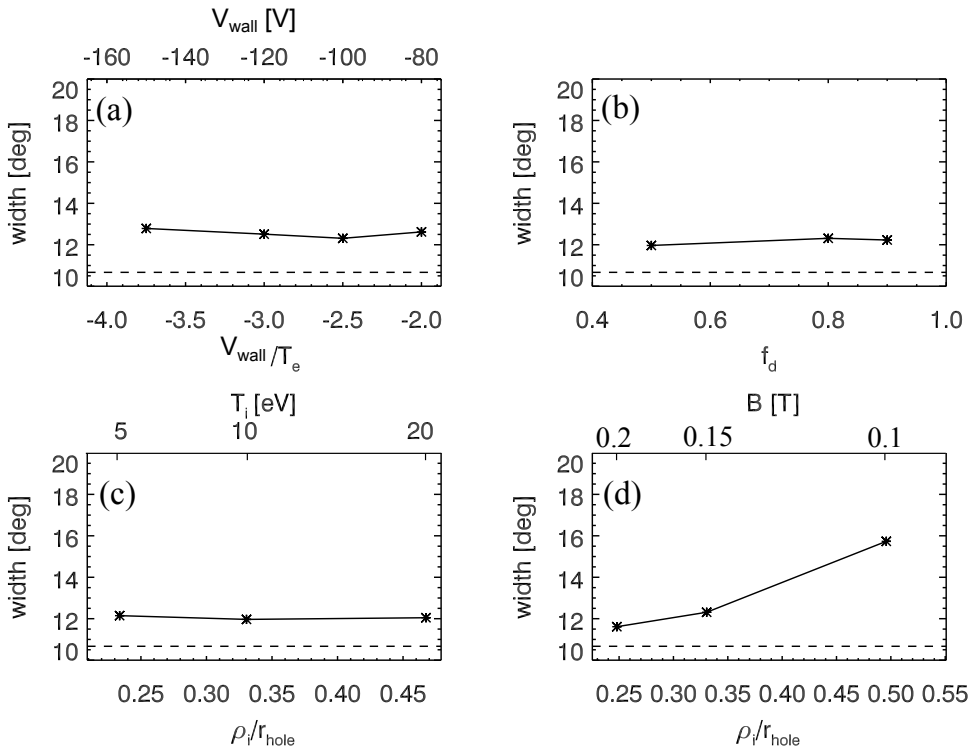

Fig. 4.11: Dependences of the angular profile width on different parameters. (a) Dependence on V_{wall}, with $(f_{\mathrm{d}}, T_{\mathrm{i}}, B) = (0.8, 10\,\mathrm{eV}, 0.15\,\mathrm{T})$, (b) dependence on f_{d}, with $(V_{\mathrm{wall}}, T_{\mathrm{i}}, B) = (-100\,\mathrm{V}, 10\,\mathrm{eV}, 0.15\,\mathrm{T})$, (c) dependence on T_{i}, with $(V_{\mathrm{wall}}, f_{\mathrm{d}}, B) = (-100\,\mathrm{V}, 0.8, 0.15\,\mathrm{T})$, and (d) dependence on B, with $(V_{\mathrm{wall}}, f_{\mathrm{d}}, T_{\mathrm{i}}) = (-100\,\mathrm{V}, 0.8, 10\,\mathrm{eV})$. Dashed lines indicate the width for the geometrical curve.

such a dependence in Fig. 4.11 (a). We will discuss the reason in Sec 4.5. Weak dependences on $f_{\rm d}$ and $T_{\rm i}$ can be explained by the fact that the $\boldsymbol{E} \times \boldsymbol{B}$ drift velocity does not depend on these parameters.

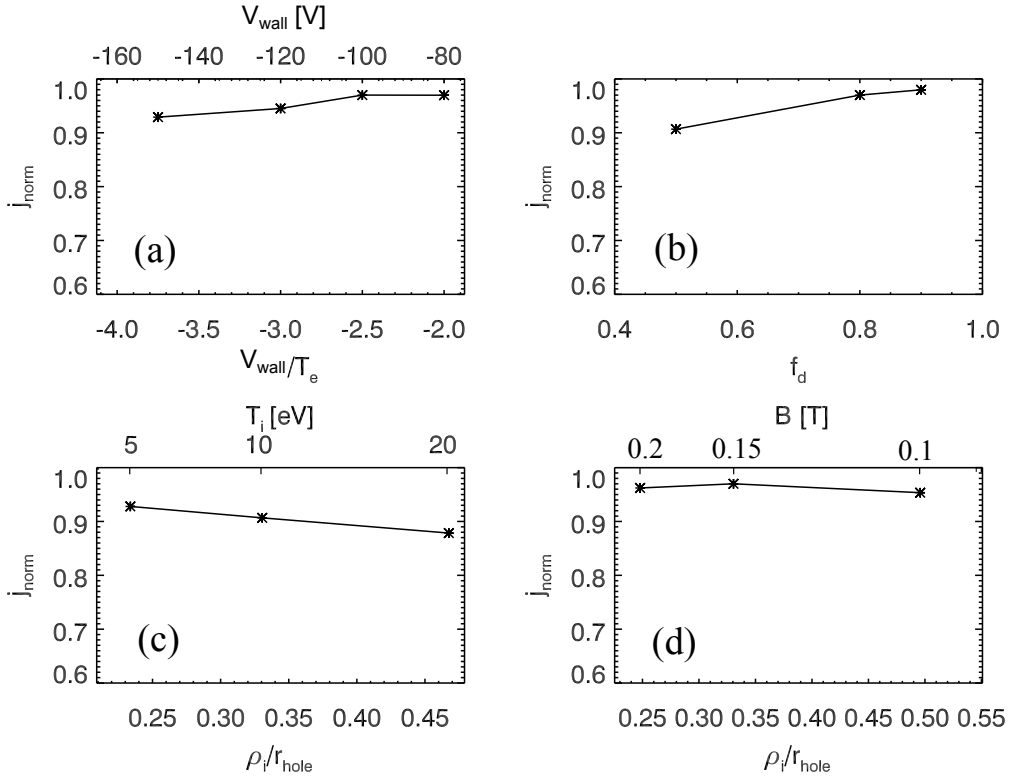

Fig. 4.12: Dependences of the height of the angular profile on different parameters. (a) Dependence on $V_{\rm wall}$, with $(f_{\rm d}, T_{\rm i}, B) = (0.8, 10\ {\rm eV}, 0.15\ {\rm T})$, (b) dependence on $f_{\rm d}$, while $(V_{\rm wall}, T_{\rm i}, B) = (-100\ {\rm V}, 10\ {\rm eV}, 0.15\ {\rm T})$, (c) dependence on $T_{\rm i}$, while $(V_{\rm wall}, f_{\rm d}, B) = (-100\ {\rm V}, 0.8, 0.15\ {\rm T})$, and (d) dependence on B, while $(V_{\rm wall}, f_{\rm d}, T_{\rm i}) = (-100\ {\rm V}, 0.8, 10\ {\rm eV})$.

Figure 4.12 shows the dependences of the height of the angular profile on different parameters. The current is calculated by integrating the distribution function for the electrons passing through the hole. In order to clarify the features of the angular profile height, the calculated current is normalized by the current due to the electrons located in front of the hole as $j_{\rm norm}$. Due to this normalization, the current at angle $\theta = 0$ should be that when we omit the sheath effect. In Figs. 4.12(a) and (b), the angular profile height decreases with the decrease of $V_{\rm wall}$ and $f_{\rm d}$. Since low energy electrons are repelled by the sheath potential as shown in Fig. 4.10, the $V_{\rm wall}$ dependence (Fig. 12(b)) is reasonable. When the value of $f_{\rm d}$ becomes small, the presheath contribution increases (see Fig. 4.5) and the $f_{\rm d}$ dependence becomes similar to the $V_{\rm wall}$ dependence. In Fig. 4.12(c), the presheath length increases with the increase of $T_{\rm i}$ and the dependence can be interpreted by the electrons repelled in the presheath region. A clear dependence of the height on B is not observed (Fig. 4.12(d)).

In TST-2 Ohmic plasmas, the ion temperature is 5 to 20 eV near the plasma edge. Generally, the fraction of the presheath is much smaller than the Debye sheath, and the cases for $f_{\rm d} = 0.8$ and 0.9 are more realistic than that for $f_{\rm d} = 0.5$. If we estimate $f_{\rm d}$ to be 0.8, the current measured in TST-2 using the Rogowski probe is 5–10% smaller than the actual

current. Figure 4.13 shows the dependence of the angular profile width and height on T_e. In order to clarify the dependence on the electron energy, the values of other parameters which depend on T_e are fixed to be those for a typical electron temperature of 40 eV. In Fig.

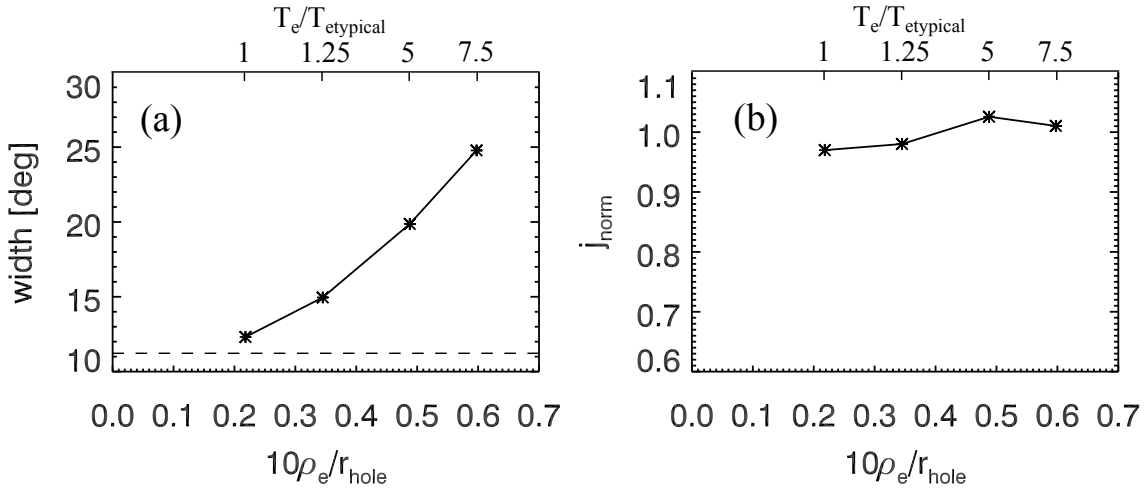

Fig. 4.13: Dependence of the angular profile width and height on T_e with (V_{wall}, f_d, T_i, B) = (−100 V, 0.8, 10 eV, 0.15 T). Dashed line in (a) indicates the width of the geometrical curve.

4.13(a), a clear dependence can be seen. This result suggests that the angular profile width is also affected by energetic electrons. In Fig. 4.13(b), the normalized current is greater than 1 at high T_e. In such cases, some energetic electrons with large Larmor radii can wrap around the rim of the hole and enter the hole even if the initial locations are outside the hole (i.e., $r_0 = \sqrt{{x_0}^2 + {y_0}^2} \geq r_{hole}$).

4.5 Analytic calculation with rhombus tube

As shown in Fig. 4.8, electrons exhibit precession in the z direction, while making round trips between the upper and lower walls (zigzag motion). Since the precession arises from E_x and E_y, it is useful to consider electron orbits in a square tube oriented along the z direction and rotated from the x axis by 45° as shown in Fig. 4.14. E_x and E_y are assumed to be finite and constant only near the wall. In this analysis, the orbit of the electron guiding center with a finite angle of θ from the z axis is calculated. The initial location and velocity are set to $(x_O, y_O, 0)$ and $(v_{xO}, 0, v_{zO})$. Figure 4.14(a) shows the cross section of the tube in the z-x plane at $y = y_O$ and Fig. 4.14(b) shows the cross section in the y-x plane. For simplicity, the strength of the electric field in the sheath region is set to be constant and ∇B and the curvature of B are not considered.

Initially, the electron travels from point O to point P (Fig. 4.14). P is the entry point to the sheath region whose width is λ. The location of the electron at this point (x_P, y_P, z_P) is given by

$$x_P = y_O + a - \sqrt{2}\lambda, \tag{4.8}$$

$$y_P = y_O, \tag{4.9}$$

$$z_P = \frac{v_{zO}}{v_{xO}}(x_P - x_O), \tag{4.10}$$

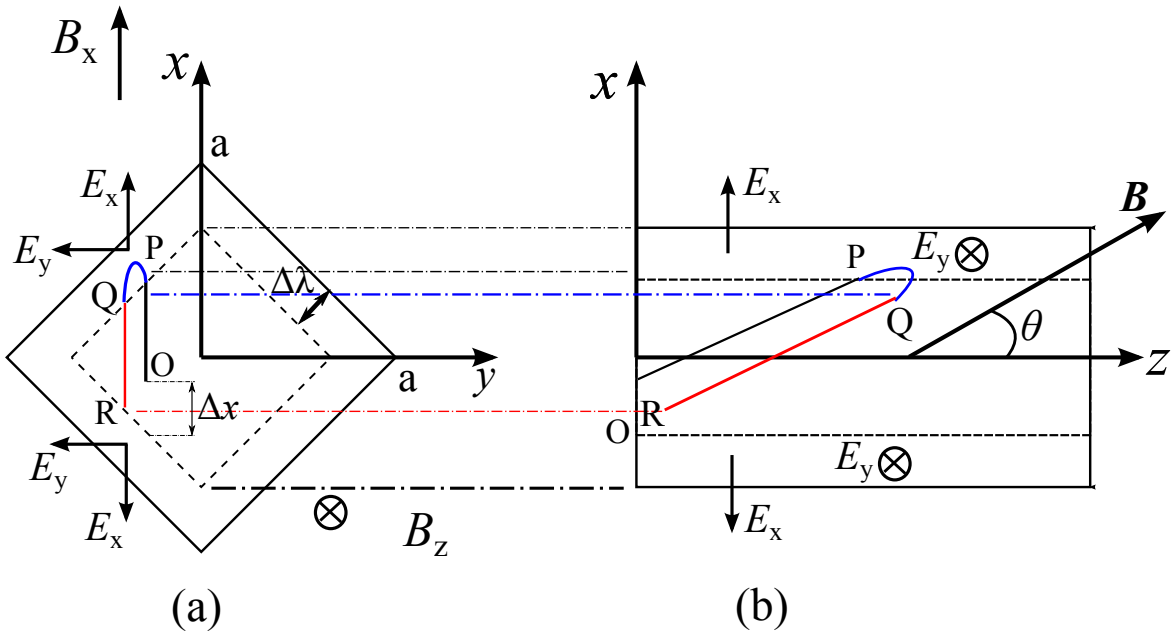

Fig. 4.14: Configuration for analytic calculation. Black line (OP), blue curve (PQ) and red line (QR) indicate the electron orbit, $\Delta\lambda$ is the length of the sheath, E_x and E_y are x and y components of the electric field, B_x and B_z are x and z components of the magnetic field, and θ is the angle between $\boldsymbol{B}$ and the z axis.

In the sheath region (PQ), $E_\perp$ and $E_\parallel$ (the sheath electric field components perpendicular to and parallel to the magnetic field) are finite. The electron is reflected in the parallel direction when the electron energy is low. In the perpendicular direction, the electron exhibits the $\boldsymbol{E} \times \boldsymbol{B}$ drift. The electron velocity in this region is given as

$$v_{\mathrm{xPQ}} = (v_\parallel + \frac{eE_\parallel}{m_e}t)\sin\theta + \frac{E_y}{B}\cos\theta, \tag{4.11}$$

$$v_{\mathrm{yPQ}} = -\frac{E_x}{B}\cos\theta, \tag{4.12}$$

$$v_{\mathrm{zPQ}} = (v_\parallel + \frac{eE_\parallel}{m_e}t)\cos\theta - \frac{E_y}{B}\sin\theta, \tag{4.13}$$

where $v_\parallel$ is the velocity in parallel to $\boldsymbol{B}$. We calculate the rightward displacement $z_\mathrm{Q} - z_\mathrm{P}$ during the transit of the electron in the sheath region (red curve in Fig. 4.14). This displacement is an important quantity, which causes net movement along the hole as shown in Fig. 4.8.

Q is the exit point from the sheath region, and the coordinates $(x_\mathrm{Q}, y_\mathrm{Q}, z_\mathrm{Q})$ can be calculated using the staying time in the sheath region Δt_PQ and the velocity expressed by Eqs. (4.11)–(4.13). Since both the entry and exit points are located on the straight boundary, the displacements should satisfy the condition $\Delta x_\mathrm{PQ} = \Delta y_\mathrm{PQ}$. Using these relationships, Δt_PQ can be calculated and the resultant coordinates for $\mathrm{Q}(x_\mathrm{Q}, y_\mathrm{Q}, z_\mathrm{Q})$ are written as

$$x_\mathrm{Q} = x_\mathrm{P} + \frac{2v_\parallel}{\Omega}\frac{E_y}{E_\parallel}\cos\theta, \tag{4.14}$$

$$y_{\rm Q} = y_{\rm P} - \frac{2v_\parallel}{\Omega}\frac{E_{\rm x}}{E_\parallel}\cos\theta, \tag{4.15}$$

$$z_{\rm Q} = z_{\rm P} - \frac{2v_\parallel}{\Omega}\frac{E_{\rm x}}{E_\parallel}\sin\theta, \tag{4.16}$$

where $\Omega = qB/m_{\rm e}$. From Q to R, the electron travels along $\boldsymbol{B}$ since there is no electric field. At point Q, the velocity is given by ($v_{\rm xO}$, 0, $-v_{\rm zO}$). The time it takes from Q to R is determined by $v_{\rm xO}$ and $x_{\rm Q}$, and is given by

$$z_{\rm R} = z_{\rm Q} - 2\frac{v_{\rm zO}}{v_{\rm xO}}x_{\rm Q}. \tag{4.17}$$

When $z_{\rm R} > 0$, the electron exhibits a similar zigzag motion as shown in Fig. 4.8, and the electron can pass through the hole. On the other hand, when $z_{\rm R} < 0$, the electron moves leftward and escapes from the hole. The condition for the electron to pass through the hole is given by

$$\begin{aligned}\frac{2v_\parallel}{\Omega} &> \frac{\tan\theta}{\tan^2\theta+2}(x_{\rm O}+y_{\rm O}+a-\sqrt{2}\lambda)\\ &> \frac{\tan\theta}{\tan^2\theta+2}\Delta x.\end{aligned} \tag{4.18}$$

where Δx is defined in Fig. 4.14. $\tan\theta/\tan^2\theta+2$ is a positive increasing function of θ as long as $|\theta| < 50°$. Eq. (4.18) implies that an electron with a large parallel velocity and an initial position located in the left lower region in Fig. 4.14(b) has a possibility to pass through the hole due to the $\boldsymbol{E}\times\boldsymbol{B}$ drift in the sheath region. This result is consistent with the orbit calculation results shown in Figs. 4.11 and 4.13. In Eq. (4.18), the contribution of the sheath electric field $\boldsymbol{E}$ is cancelled out. This can explain the weak $V_{\rm wall}$ dependence shown in Fig. 4.11(a). The λ term on the right hand side of Eq. (4.18) also contributes to relax the condition, and has a similar effect to $V_{\rm wall}$.

4.6 Experiments at low B and high B

Ohmic plasma experiments at low B and high B were performed to verify the dependence of the angular profile. These experiments were carried out with special care to maintain the $I_{\rm p}$ waveform the same. The central hole of the Rogowski coil was located at $R = 515.5$ mm, and the angular dependence of the current was measured by rotating the direction of the hole on a shot by shot basis. B, $T_{\rm e}$ and $n_{\rm e}$ were also measured by the pick-up coils and the Langmuir probe located near the Rogowski coil. The waveforms of plasma discharges at low B and high B are shown in Fig. 4.15. The waveforms of $I_{\rm p}$ are almost the same in these two discharges, and the hatched interval in Fig. 4.15(a) where good reproducibility was obtained, was analyzed. Time evolutions of $V_{\rm f}$, $T_{\rm e}$ and $n_{\rm e}$ measured by the Langmuir probe on the Rogowski probe are nearly the same in these two discharges. Thus, a comparison between these two cases reflects the B dependence. The angular profile width was calculated according to the definition described in Sec. 4.4.

Figure 4.16 shows the time evolutions of the angular profile width for these two cases. The width is larger for the lower B case than the higher B case. This is consistent with the calculated width of 13° for $B = 0.13$ T and 12° for $B = 0.17$ T. In Fig. 4.16, the widths in increase monotonically with time. This trend cannot be explained by the time variations of measured plasma parameters, which are nearly constant. Although energetic electrons may

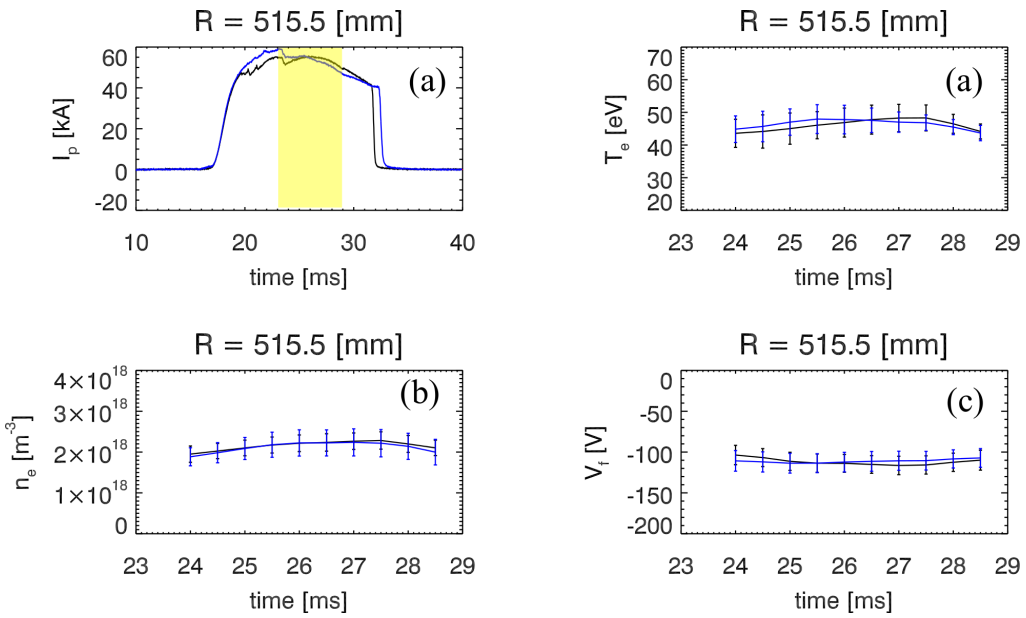

Fig. 4.15: Waveforms of plasma discharges at low B (0.13 T, black) and high B (0.17 T, blue). I_p (a), T_e (b), n_e (c), floating potential measured by the Langmuir probe V_f (d). The error bars show the scatter of averaged values.

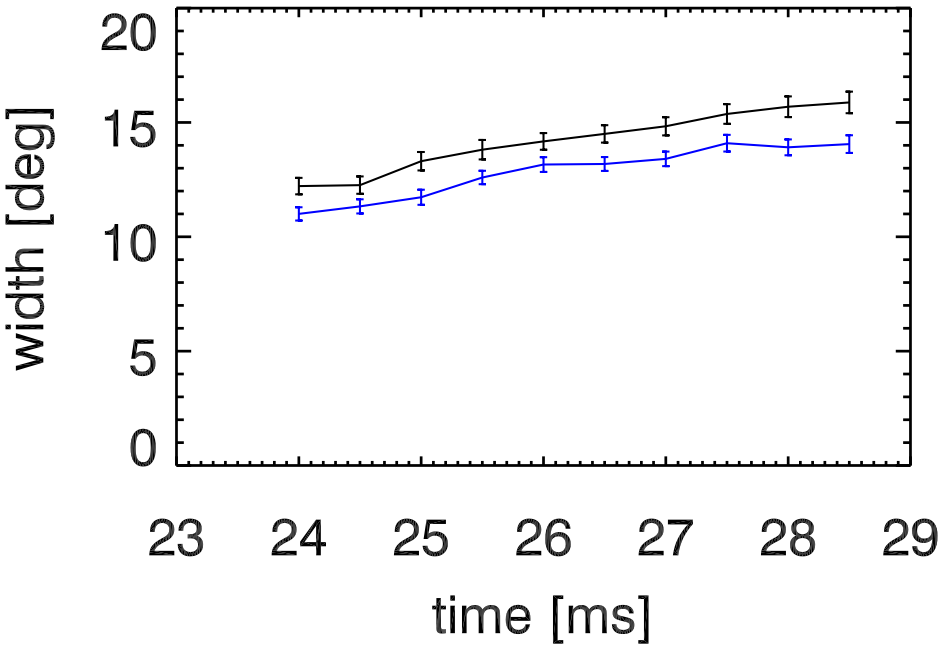

Fig. 4.16: Comparison of the angular profile width at low B (black) and high B (blue). The error bars show the fitting errors.

affect the width as was shown by the T_e dependence shown in Fig. 4.13(a), we cannot find such a trend in the measured floating potential, suggesting that the contribution of energetic electrons is small. Thus, further study is necessary to interpret this trend.

4.7 Summary of the sheath effect

Sheath effects on the Rogowski probe measurement were studied using orbit calculations of electrons passing through the hole of the Rogowski coil, combined with analytic calculations of a simplified configuration. The calculations suggest that the angular profile width is affected by the $\boldsymbol{E} \times \boldsymbol{B}$ drift and repulsion by the sheath electric field. The height of the angular profile is affected by V_{wall} and by the fraction of the presheath (i.e., T_i and f_d). In TST-2 Ohmic plasmas, the measured current using the Rogowski coil is estimated to be 5–10% smaller than the real current. Experiments at low B and high B were also performed to verify the effect of the $\boldsymbol{E} \times \boldsymbol{B}$ drift on the angular profile width. The width obtained in the low B case was wider than that obtained in the high B case. This is consistent with both numerical and analytic calculation results. Considering these results, we can conclude that the broadening of the angular profile is explained by the $\boldsymbol{E} \times \boldsymbol{B}$ drift due to the sheath formed around material surfaces.

In the orbit calculation, the $\boldsymbol{\nabla} B$ drift and the curvature drift effects are included. For $R = 0.5$ m, $B = 0.1$ T and $T_e = 40$ eV, the sum of the drift velocities is estimated to be 800 m/s. When the distance from the probe wall is $2\lambda_d$, E is 10^5 V/m and the $E \times B$ drift velocity is about 10^6 m/s at $B = 0.1$ T. Thus, in this case, the $\boldsymbol{\nabla} B$ drift and the curvature drift velocities are much smaller than the $E \times B$ drift velocity and can be ignored.

The experimentally obtained result was reproduced well by the calculation. In addition, parameter dependences agreed among the experimental result, numerical calculation, and analytic calculation. In conclusion, we have clarified the sheath effects on the local current measurement by a Rogowski probe.

Chapter 5

Experimental results using the Rogowski probe

5.1 Experimental setup

In order to study plasma equilibrium and instabilities, we employed not only the Rogowski probe, but also the other diagnostics installed in TST-2. Figure 5.1 shows toroidal cross section seen from the top, and the diagnostics placed at $Z = 0$ mm are shown. The details of SBD, AXUV, an interferometer and a fast visible camera are described in Sec. 1.5. These are employed to understand the whole plasma configurations. A mach probe is also placed in a different toroidal location from the Rogowski probe, and it consists of some Langmuir probes and pick-up coils. A schematic configuration of the mach probe is shown in Fig. 5.2. Electrodes A and B for the mach probe in TST-2 are parallel or anti-parallel to the $I_{\rm p}$ direction. Generally, a mach probe is used for the measurement of plasma flow at the plasma edge region in tokamak plasmas [82]. Using the mach probe, we can measure the toroidal asymmetry of ion saturation current $I_{\rm is}$ and floating potential $V_{\rm f}$, which reflect the plasma flow and the electron current, respectively. From the signals of the Rogowski probe and the mach probe, we can get information on plasma parameters at the plasma edge region.

5.2 Radial current density profile for Ohmic plasma

Results of current density profile measurements for Ohmic plasma discharges are presented in this section. The TST-2 Ohmic plasma configurations can be classified into two types. One is the inboard-limited configuration whose radial location of the Last Closed Flux Surface (LCFS) in the low field side ($R_{\rm LCFS}$) is located inside the antenna limiter location ($R_{\rm ant-lim}$) (see Fig. 5.1). The other is the outboard-limited configuration whose $R_{\rm LCFS}$ is the same as $R_{\rm ant-lim}$. Using the Rogowski probe, we investigated the radial current density j profile for these two configurations. The measured profiles and the calculated profiles from EFIT code were compared.

Inboard-limited plasmas

Here, the results for inboard-limited plasma are shown. Figure 5.3(a) shows an example of the j signals measured by the Rogowski 1 and 2, and Figs. 5.3(b) and (c) show the comparison between j and $B_{\rm Z}$ profiles measured by the Rogowski probe and calculated from the EFIT

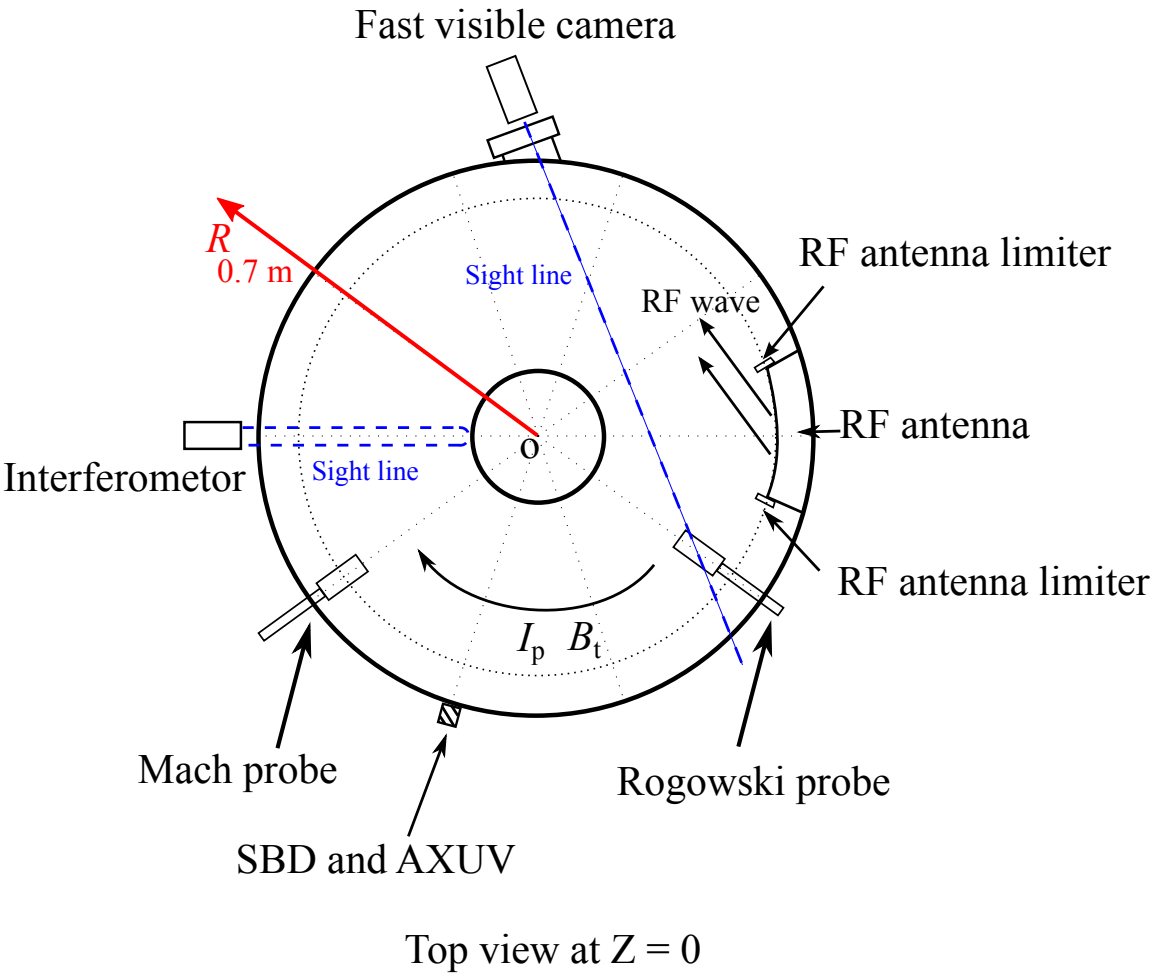

Fig. 5.1: Experimental setup.

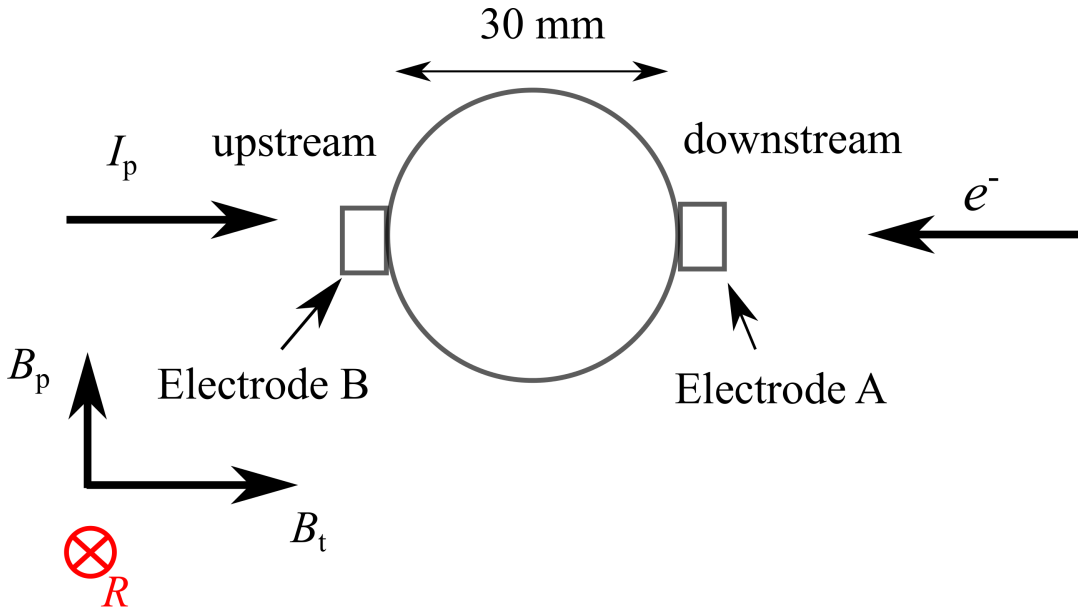

Fig. 5.2: A configuration of the mach probe on TST-2.

code at 29 ms. The location of LCFS at the low field side is calculated by the EFIT code and it is located at $R < R_{\mathrm{ant-limit}}$. From Figs. 5.3(b) and (c), good agreements between the experimental and calculated profiles near the plasma edge were confirmed for both j and B_Z.

Figure 5.4 shows the radial j profiles measured by a shot on shot basis for the inboard-limited configuration and they were measured for three θ cases (10°, 15°, 20°, see Fig. 3.2). In Fig. 5.4, the absolute current density $(j_t^2 + j_z^2)^{0.5}$ calculated by EFIT shows the profiles with (black curves) and without (blue curves) the probe insertion. Similar to Fig. 5.3, a good agreement between the experimentally obtained j profile and the calculated profile near the plasma edge ($R \leq 550$ mm) was confirmed. On the other hand, in the region of $R < 550$ mm, deviations were seen. Due to the time evolution of current direction θ_j and due to the angular dependence of the Rogowski coil signal, the true j can be larger than the values obtained at these three θ cases. Considering these effects, the experimental j seems to be larger than the j from the EFIT code at $R < 550$ mm. This deviations are partly due to the model profile used in EFIT. Therefore, taking into account the systematic error of 5 kA/m^2, and the shot to shot scatter of 5%-20%, it seems to be possible to improve the accuracy of equilibrium reconstruction by using the Rogowski coil data.

Outboard-limited plasmas

Local currents in the vicinity of $R_{\mathrm{ant-lim}}$ were investigated for outboard-limited configurations. The experimental results are shown in Figs. 5.5 and 5.6. In Figs. 5.5(a) and 5.6(a), signals of Rogowski 2 and 1 were finite while they were located in the region of $R > R_{\mathrm{ant-lim}}$. In the EFIT code, toroidal symmetry is assumed and the current outside the LCFS is set to be 0. It is a remarkable fact that both measured and calculated B_Z profiles agreed each other even if the j profiles disagree. These results suggest that the assumptions of toroidal symmetry and no current outside $R_{\mathrm{ant-lim}}$ are not valid. In such a case, a pickup coil array would fail in reconstructing j, and only a Rogowski coil can be used.

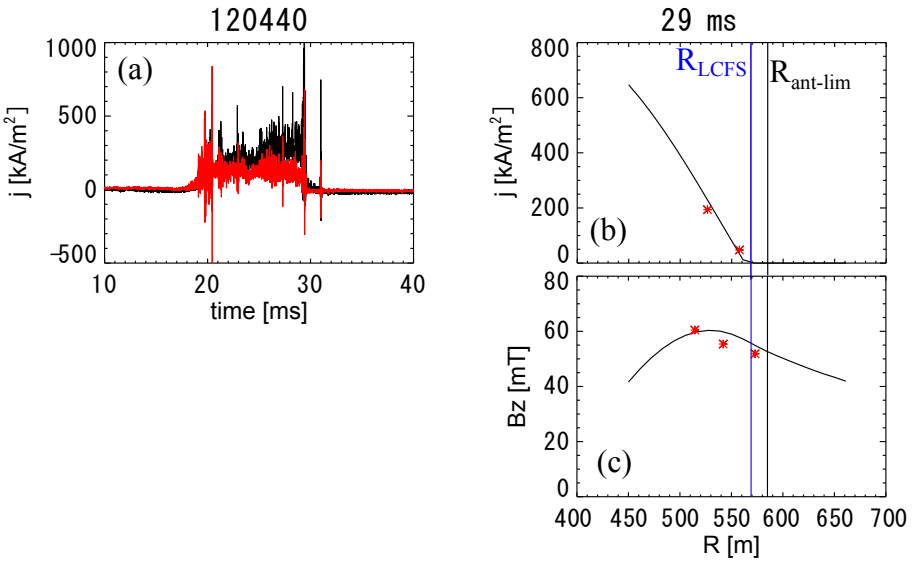

Fig. 5.3: Time evolution of local current densities measured by Rogowski 1 (black) and 2 (red) at $\theta = 15°$ (a), and the radial j profiles obtained from the experiment (red symbols) and EFIT code (black curve) (b) and the radial B_Z profiles obtained from the experiment (red symbols) and EFIT code (black curve) (c). Blue vertical lines indicate $R_{\rm LCFS}$ and black vertical lines indicate $R_{\rm ant-lim}$.

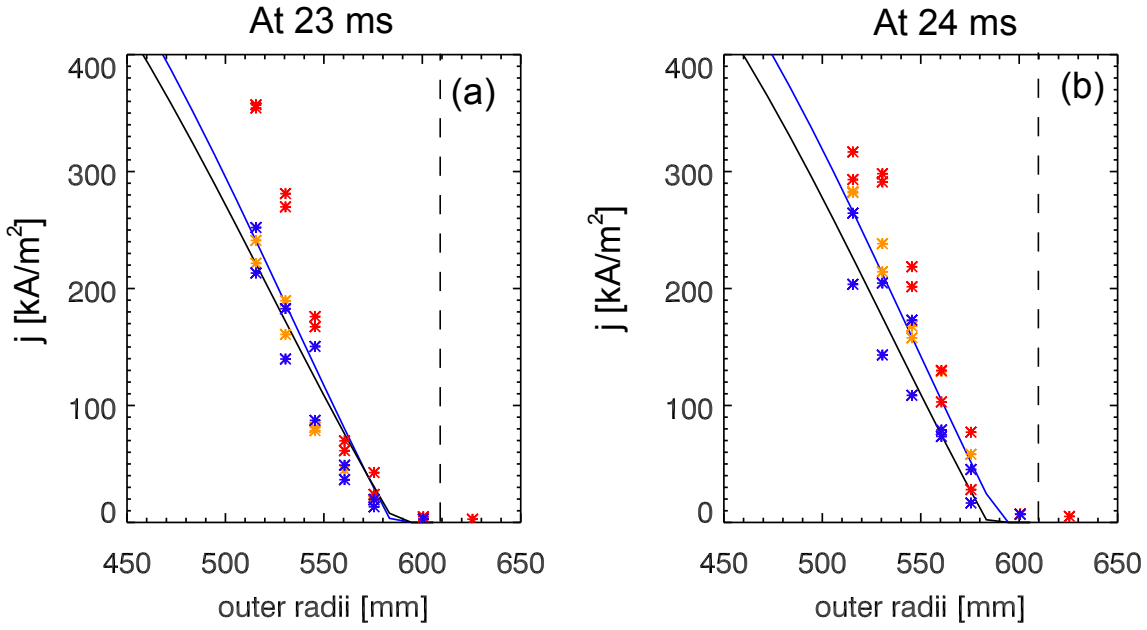

Fig. 5.4: Radial profiles of j at two different times. Black and blue curves represent the EFIT calculations for the cases with the deep insertion of the Rogowski probe (black) and without the insertion of the Rogowski probe (blue), respectively, and orange (10°), red (15°), and blue (20°) symbols represent the measured values. Dashed vertical lines in (a) and (b) indicate $R_{\rm ant-lim}$.

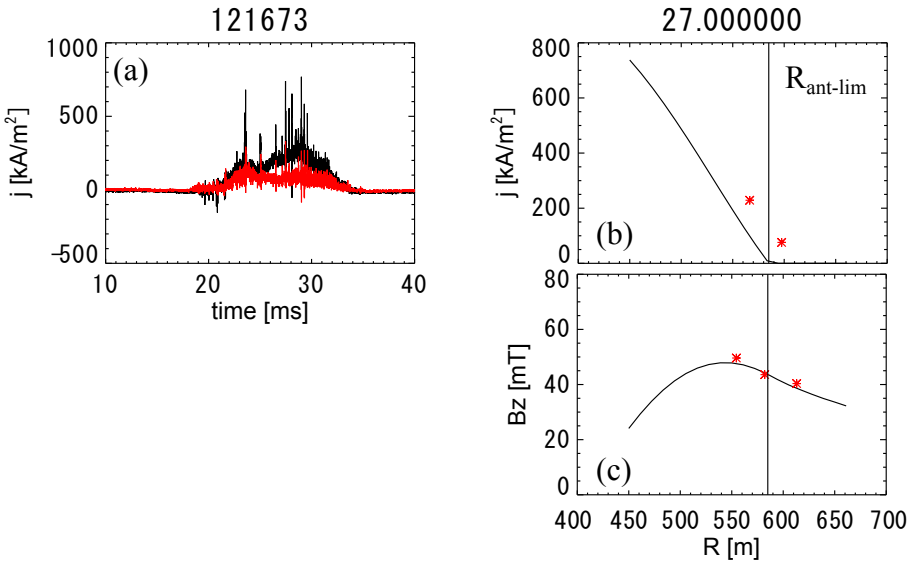

Fig. 5.5: Time evolution of local current densities measured by Rogowski 1 (black) and 2 (red) at $\theta = 15°$ (a), and the radial j profiles obtained from the experiment (red symbols) and EFIT (black curve) (b) and the radial B_z profiles obtained from the experiment (red symbols) and EFIT (black curve) (c). Black vertical lines indicate R_{LCFS} and $R_{\mathrm{ant-lim}}$.

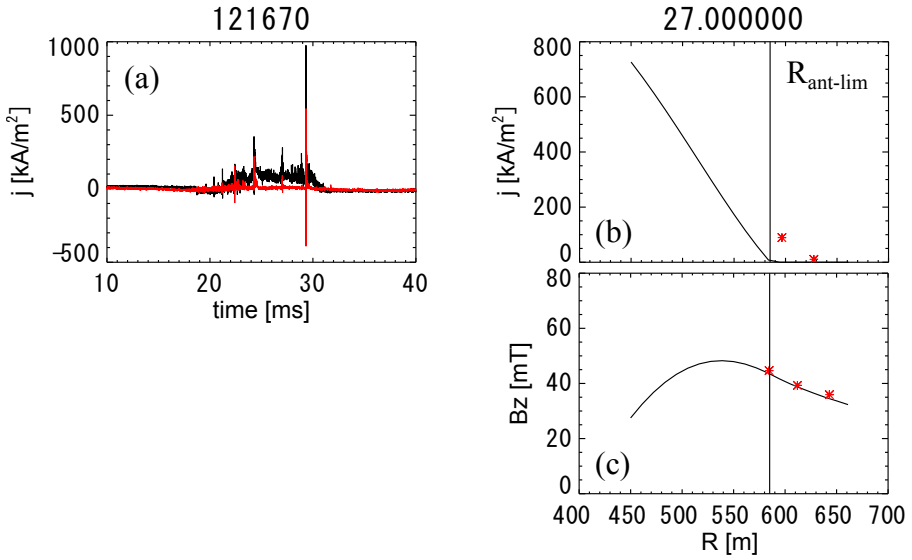

Fig. 5.6: Time evolution of local current densities measured by Rogowski 1 (black) and 2 (red) at $\theta = 15°$ (a), and the radial j profiles obtained from the experiment (red symbols) and EFIT (black curve) (b) and the radial B_z profiles obtained from the experiment (red symbols) and EFIT (black curve) (c). Black vertical lines indicate R_{LCFS} and $R_{\mathrm{ant-lim}}$.

5.3 Current density measurement for RF plasma

In TST-2, non-inductive plasma startup experiments using RF (Radio frequency) waves in the frequency ranges of LHW (Lower hybrid wave) have been performed using various types of antennas [54]. By using the Rogowski probe, we successfully measured j at the plasma edge region for RF startup plasmas, which is driven by the waves from the dielectric loaded 4-waveguide array (GRILL) antenna. A photograph of the GRILL antenna is shown in Fig. 5.7.

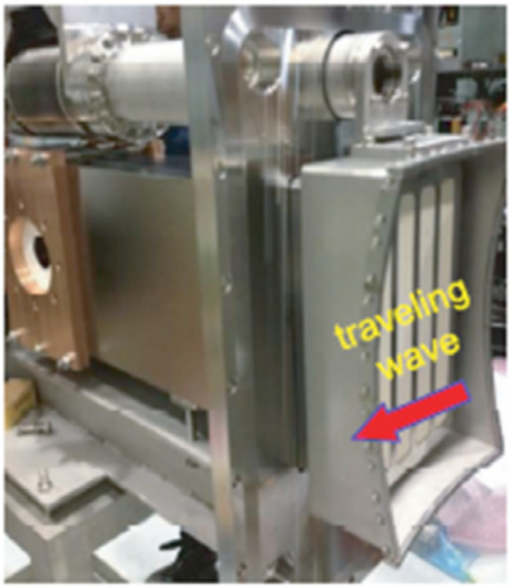

Fig. 5.7: A photograph of the GRILL antenna [54].

Each waveguide consists of a rectangular alumina block whose surfaces are covered with a layer of 80 μm thick nickel [83]. The cross-sectional dimensions of the waveguide is 30 mm (width) $\times$ 285 mm (height). In the experiment, the GRILL antenna was located at the man hole (see Fig. 5.1) and RF wave is injected oppositely to the B_t and I_p directions. The experimental result is shown in Fig. 5.8.

In this experiment, plasmas is initially excited by LHW and ECW, and I_p is driven up to 1.5 kA. The RF antenna limiter was located at $R = 585.5$ mm and the Rogowski 1 was located at $R = 501.5$ mm, and the hole direction (θ) was set to be 0°, since the magnetic pitch angle in this experiment is almost 0° due to the small I_p. At the initial of plasma discharge, abrupt increases of both line integrated density and j are observed. Since the line integrated density depends not only on the electron density but also on the plasma size, it is inferred that the plasma size is large at the initial of the discharge, and the increase of the current density can be explained from its time evolution. In RF startup plasmas, localized j at the open flux surface region is expected by the equilibrium calculation which allows the existence of the finite current density where $R > R_\mathrm{LCFS}$ [58]. In the EFIT code, the current density outside R_LCFS is considered to be 0 and EFIT cannot be applied to such plasma equilibrium reconstruction. Thus, we compared the result of equilibrium calculation used in Ref. [58] and the experimentally obtained result (see Fig. 5.9). Even if the existence of the current density at the open flux surface is allowed in the equilibrium calculation, the large current outside

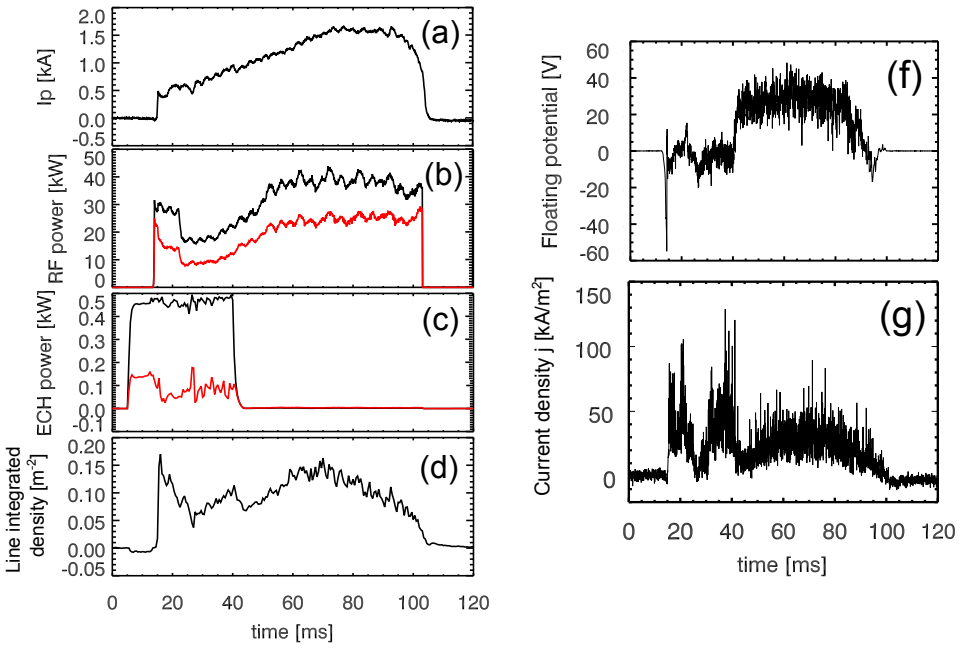

Fig. 5.8: The experimental result for a RF startup plasma. (a) plasma current, (b) RF power (black : injection, red : reflection), (c) ECH power (black : injection, red : reflection), (d) line integrated density, (e) floating potential at $R = 501.5$ mm, (f) current density measured by the Rogowski 1 at $R = 501.5$ mm. The hole direction (θ) is 0°.

of LCFS was observed. At 70 ms, the averaged j in the poloidal cross-section ($I_{\rm p}/S_{\rm poloidal}$, where $S_{\rm poloidal}$ is the poloidal cross-sectional area inside of LCFS) is about 7 kA/m^2 and the measured value is seven times larger than it. From this experiment, we obtained the first result which indicates the existence of a large current in the open flux region.

5.4 Results for plasma instabilities for TST-2 Ohmic plasmas

5.4.1 Typical Ohmic plasma discharges

In Ohmic plasma discharges, there are mainly two types of plasma instabilities. One is an IRE (Internal Reconnection Event) and the other is instabilities accompanying fluctuations in the frequency ranges from 10 - 100 kHz. These instabilities are being studied to understand the underlying physics for spherical tokamak instabilities and the turbulences [18, 84].

Firstly, we show typical signals of magnetic fluctuation dB/dt at $Z = 7$ mm and $R = 700$ mm, current density j, and ion saturation current $I_{\rm is}$ which were measured by the Rogowski probe ($R = 551.5$ mm) (see Fig. 5.10). dB/dt signal mainly reflects the global fluctuations, and j and $I_{\rm is}$ reflect local fluctuations. From Fig. 5.10(a), sudden increase of plasma current ($I_{\rm p}$ spike) due to an IRE can be seen at 29 ms. At the same time of the $I_{\rm p}$ spike, the large fluctuations of dB/dt, j and $I_{\rm is}$ appeared. In addition, different types of magnetic fluctuations are seen at the initial, the middle and the end of the plasma discharge (17-21.5 ms, 26-28 ms and 30-36 ms), respectively. For these time periods, j and $I_{\rm is}$ also show fluctuations with almost similar frequency ranges of dB/dt. Hereafter, we call these time periods as Phase 1, Phase 2 and Phase 3. Figure 5.11 shows enlarged views of fluctuations, dB/dt, j and $I_{\rm is}$ for

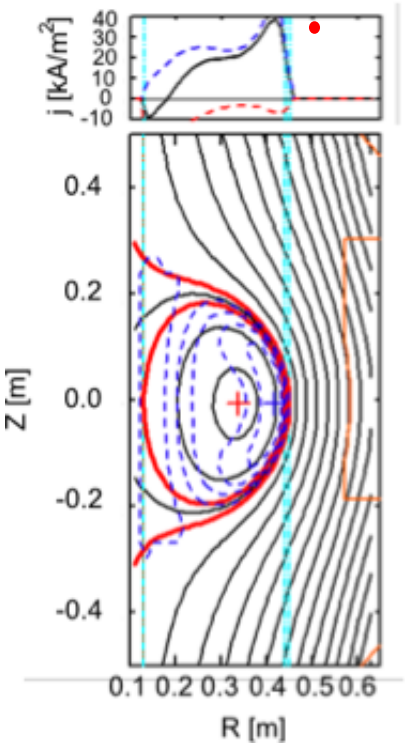

Fig. 5.9: The comparison between the equilibrium calculation and the experimentally obtained current density at 70 ms for the plasma discharge shown in Fig. 5.8. Red symbol is the measured data using the Rogowski 1.

Phase 1, 2 and 3 respectively. In Phase 1 and 3, sinusoidal oscillations for dB/dt are seen, and the fluctuations of j and $I_{\rm is}$ seem to be correlated. In Phase 2, sudden spikes for dB/dt, j and $I_{\rm is}$ are observed and they show very different appearance from the oscillations in Phase 1 and 2. In addition, the shape of spikes of j and $I_{\rm is}$ are quite similar. Since the signal of $I_{\rm is}$ is affected by both $n_{\rm e}$ and $\sqrt{T_{\rm e}}$, we need to investigate that which has large contribution to the current spikes.

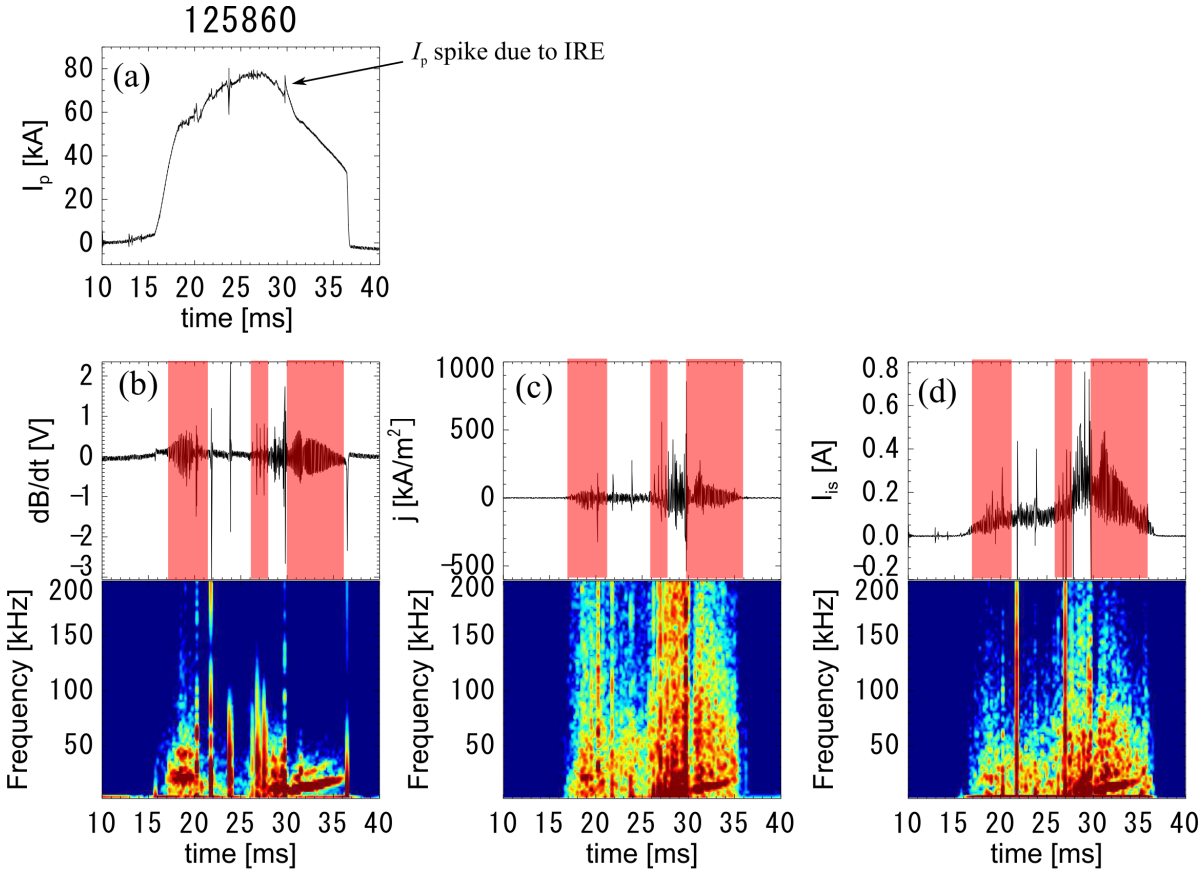

Fig. 5.10: Typical Ohmic plasma discharge in TST-2. Time evolution of plasma current $I_{\rm p}$ (a). Figures (b), (c) and (d) are the sets of the raw data and power spectrum for dB/dt (Z = 7 mm and R = 700 mm), j fluctuation (above 2 kHz, R = 551.5 mm) and $I_{\rm is}$ (R = 551.5 mm).

As described in Sec. 1.5.2, we carefully performed the IV curve fitting for the estimation of electron temperature $T_{\rm e}$ and electron density $n_{\rm e}$. Figure 5.12 shows the time evolutions of j, $n_{\rm e}$, $T_{\rm e}$ and the electron pressure $P_{\rm e}$ measured by the Rogowski probe at the plasma edge region. Hatched regions of Figs. 5.12(a) and (b) (red and blue) represent during Phase 2 and IRE, respectively. During the sudden spikes and IRE, some IV curves were not able to be measured due to the abrupt changes of the plasma potentials in the vicinity of the measurement regions. In such a case, we cannot estimate $T_{\rm e}$ and $n_{\rm e}$. In Fig. 5.12(c)-(h), the data points those who show clear experimental IV curve and good IV curve fitting are plotted. For example, IV curve I and II in Fig. 5.12 show the fitting results for the sudden increases of $n_{\rm e}$ and $T_{\rm e}$. The fitting curves (red and blue) are well fitted to the experimental data (black curves), and the estimations of $n_{\rm e}$ and $T_{\rm e}$ seems to be reliable. From Fig. 5.12,

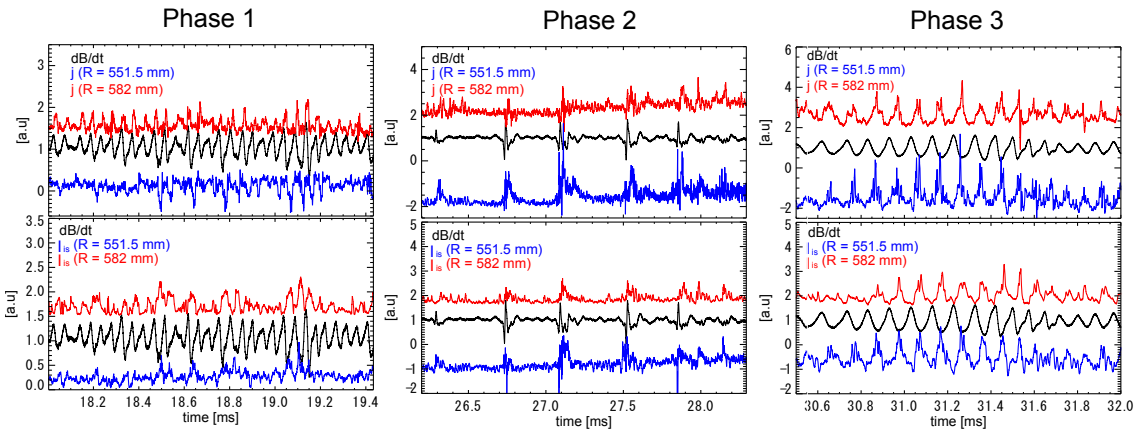

Fig. 5.11: Enlarged views of dB/dt, j and $I_{\rm is}$ for Phase 1, 2 and 3, respectively.

we can see that the shape of sudden spikes for j are quite similar to those for $n_{\rm e}$. On the other hand, such similarities between j and $T_{\rm e}$ cannot be seen. These result indicate that the increase of $n_{\rm e}$ near the region of the Rogowski probe mainly contribute to sudden spikes for j. Two scenarios which can cause these sudden spikes are possible. One is a simple increase of $n_{\rm e}$ at the edge region, and second one is that the high dense structure crosses the region around the Rogowski probe head. Detailed investigation for the sudden spikes are presented in Sec. 5.4.6. Typical values of $n_{\rm e}$ and $T_{\rm e}$ at the central region of TST-2 Ohmic plasmas are $\sim 5 \times 10^{19}$ m^{-3} and 200-300 eV. From Fig. 5.12, $n_{\rm e}$ and $T_{\rm e}$ at the edge often increases up to 10-20% of their central values during Phase 2. Similar to Phase 2, increases of j and $n_{\rm e}$ are also observed during an IRE, but the increase of $T_{\rm e}$ cannot be seen.

5.4.2 Tow types of IRE and characterization of IRE

In TST-2 Ohmic discharges, there are two typical IREs. One is that occurs at the initial or the middle of phase of a discharge duration, and it often induces a plasma disruption. Second is that occurs at the end of a discharge duration and it does not induce a disruption. Hereafter, we call these IREs as type A and type B, respectively. Typical plasma discharges for these two types of IREs are shown in Fig. 5.13. In the case of type A, $I_{\rm p}$ spike and a plasma disruption are induced at 27.3 ms, and in the case of type B, $I_{\rm p}$ spike occurred at 31.5 ms.

Similar to in Ref. [18], we are going to use $I_{\rm p}$ spike as a representative parameter for the analysis. In Ref. [18], the magnitude of $I_{\rm p}$ spike is used to analyze IREs and $\Delta I_{\rm peak}$ is introduced as the height of $I_{\rm peak}$. They have a linear relationship each other. In the following, we are going to use $DeltaI_{\rm peak}$ as the representative indicator for IRE and, hereafter, we denote $\Delta I_{\rm peak}$ as $\Delta I_{\rm p}$. Figure 5.14(c) shows an example of the estimation of $\Delta I_{\rm p}$. Before the peak of $I_{\rm p}$ spike, the waveform of $I_{\rm p}$ is fitted by $\alpha_0 \exp((x-\alpha_1)/\alpha_2)$ where $\alpha_{0,/;1,/;2}$ are fitting parameters and x is the time (see blue curve in Fig. 5.14(c)). As shown in Fig. 5.14(c), $\Delta I_{\rm p}$ is the height of $I_{\rm p}$ from the linear trend before the peak of $I_{\rm p}$ spike. Δt is like a time width of $I_{\rm p}$ spike. For the type B of IRE, typical Δt is about 0.45 ms. Δj describes peak to peak amplitude of the current spike during an IRE. Note that the current density shows a bipolar

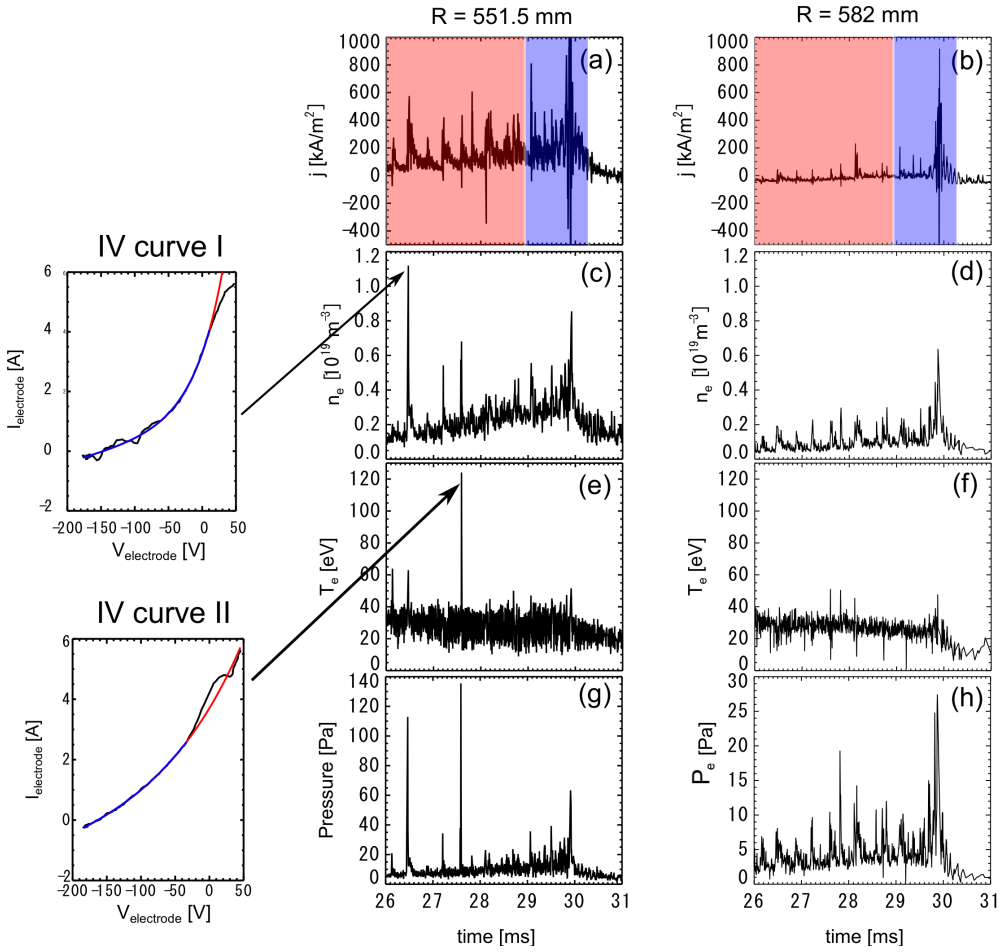

Fig. 5.12: A typical time evolutions of j, n_{e}, T_{e}, and P_{e} during Phase 2 (red hatched region) and an IRE (blue hatched region). Time evolutions of j ((a) and (b)), time evolutions of n_{e} ((c) and (d)), time evolutions of T_{e} ((e) and (f)) and time evolutions of plasma pressure P_{e} ((g) and (h)). Black curves for IV curve I and II are the experimentally obtained data which show sudden spikes of n_{e} and T_{e}, respectively. Red and blue curves in IV curve I and II are the fitting results, and the plotted region of blue curves shows the fitting regions.

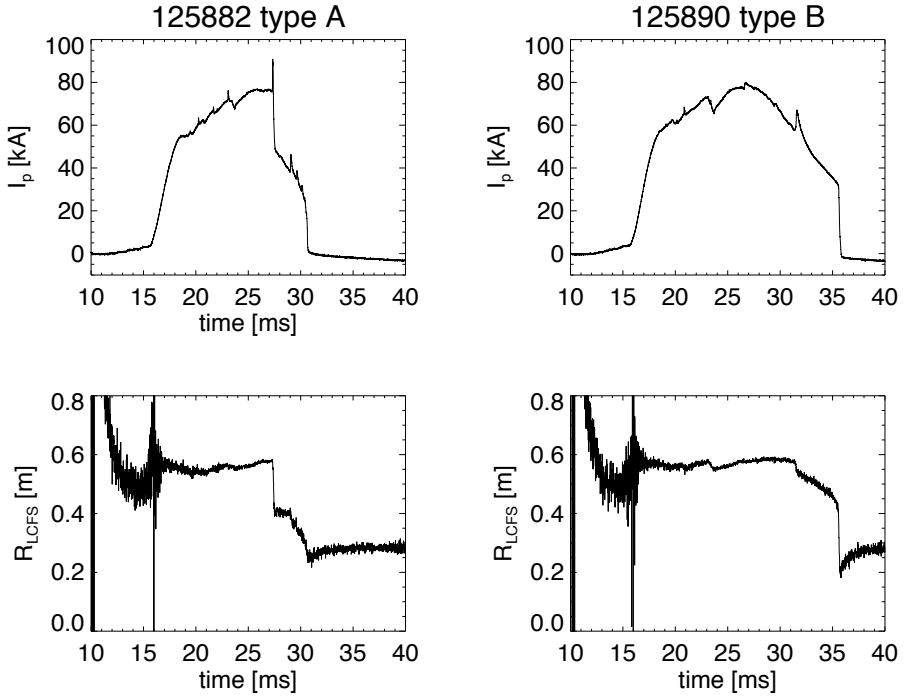

Fig. 5.13: Two typical plasma discharges with type A (black) and type B (red) of IREs.

spike. The detailed description on the bipolar spike is presented in Sec. 5.4.4.

Figure 5.15 shows the comparison of the shapes of I_p spikes for type A (a) and B (b), respectively. ΔI_p are normalized to 1 and peak timings of the spikes are set to be 0. In order to perform the analysis of IRE, some kinds of characterization of IRE is important. The shape of I_p spike should be affected by many kinds of reasons. Actually, there are some kinds of shapes of I_p spikes in both type A and B. From Fig. 5.15, it is clearly seen that shapes of I_p spikes appeared to be almost the same (each ΔI_p have almost the same Δt), and we can assume that IREs which have almost the same Δt as IREs induced by the same reasons. In the following, we proceeded analysis gathering data which have almost the same Δt for type A and B.

5.4.3 Time sequence of the changes of plasma parameters due to IRE

When an IRE occurs, many plasma parameters changes. Some parameters response to the IRE quickly. On the other hand, the others show delayed responses to the IRE. The investigation of the time sequence of plasma parameters during an IRE can be helpful to determine the precursor or the cause of an IRE. In addition, the comparison between the time sequences for type A and B can clarify the main cause for a disruption. Firstly, the time sequences of main plasma parameters which reflect the global plasma status (SXR emissions, plasma radiations, electron densities, and magnetic fluctuations) for type A and B are investigated. Secondly, the edge plasma parameters are investigated using the Rogowski probe signals. Comparison between these plasma parameters during IREs gives us understandings of plasma motions and its frequencies (or velocities) during IREs.

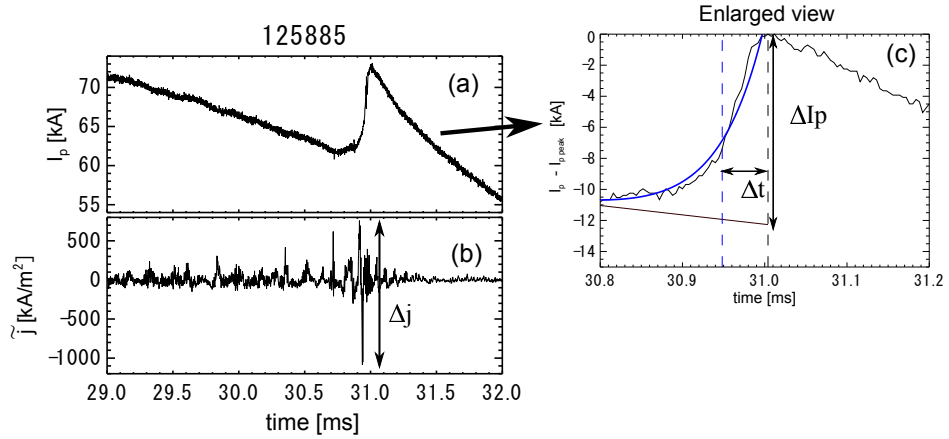

Fig. 5.14: Characterization of $I_{\rm p}$ spike. The waveform of $I_{\rm p}$ (a), the waveform of j fluctuation measured by Rogowski 1 (b) and the enlarged view of (a) (c). $\Delta I_{\rm p}$ and Δt are the amplitude and the time width of $I_{\rm p}$ spike. Δj is the peak to peak amplitude of local current spike due to IRE.

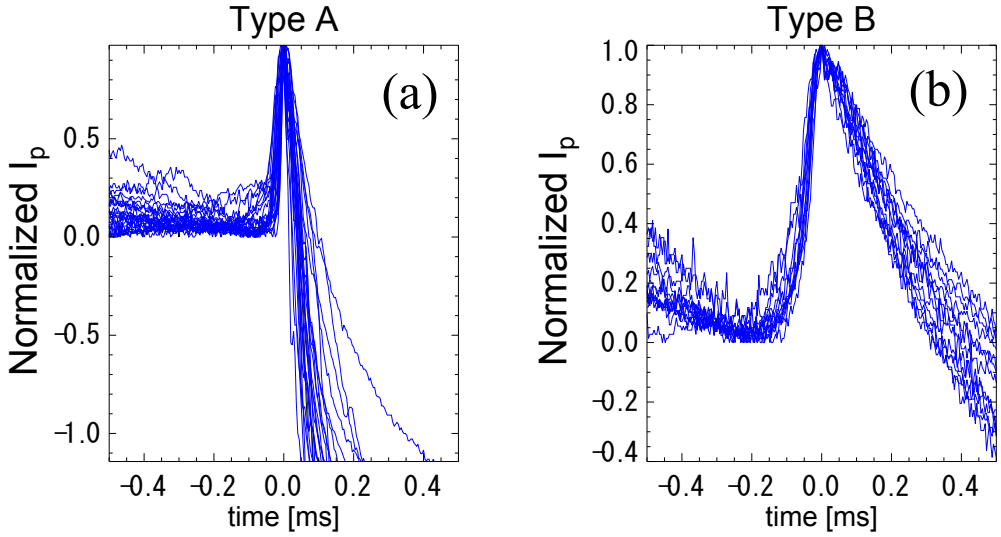

Fig. 5.15: Comparison of normalized $I_{\rm p}$ spikes for type A IRE (a) and type B IRE (b), respectively.

SXR emissions, radiations and line-integrated density before $I_{\rm p}$ spike

SXR emissions, plasma radiations and electron densities are one of the main plasma parameters varying during an IRE in TST-2. As shown in Fig. 5.15, we gathered their data for type A and B, respectively, and SXR emissions (SBD), radiations (H_α, AXUV) and line-integrated densities ($n_{\rm e}l$) of the discharges with type A and B are plotted in Figs. 5.16 and 5.17. For the comparison, the peak of each $I_{\rm p}$ spike are set to be 0 ms. In Figs. 5.16(f) and 5.17(f), values of $n_{\rm e}l$ just before 0 ms are adjusted to be 0. Numbers of positive spikes of SXR signals for type A are quite larger than those for type B (see Figs. 5.16 and 5.17 of (b) and (c)). For both cases, SXR emissions decrease just before 0 ms. Similar to it, $n_{\rm e}l$ for both cases decreases before 0 ms. In type A, $n_{\rm e}l$ is almost constant before the decrease of $n_{\rm e}l$. On the other hand, in type B, $n_{\rm e}l$ increases before the decrease.

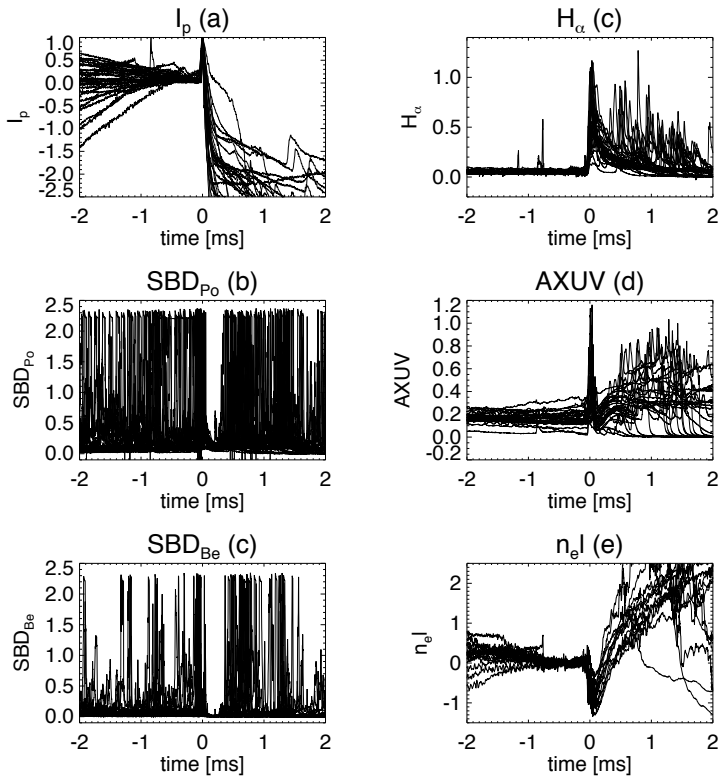

Fig. 5.16: $I_{\rm p}$ (a), SBD signal with polypropylene filter ($\rm SBD_{Po}$: sensitive up to 400 eV) (b), SBD signal with Beryllium filter ($\rm SBD_{Be}$: sensitive up to 1 keV) (c), $\rm H_\alpha$ (d), AXUV (e), and $n_{\rm e}l$ (f) for type A.

Figure 5.18 shows the comparison between the averaged waveforms for type A (black) and type B (red) shown in Figs 5.16 and 5.17, respectively. On average, SXR emissions for type A are quite larger than those for type B. This is due to many positive spikes before $I_{\rm p}$ spikes (see Fig. 5.16). In addition, the SXR emissions show keen spikes (i.e., with a shorter Δt) before 0 ms for type A. The responses of H_α emissions for both type A and B have time delays to those of SXR emissions, AXUV and $n_{\rm e}l$. Thus, H_α emission is a result of the IRE for both cases. As is shown in [85], the pressure gradient can cause an IRE. Since the increase of $n_{\rm e}l$ is seen in the case of type B, it can be assumed that one of the reasons to cause type

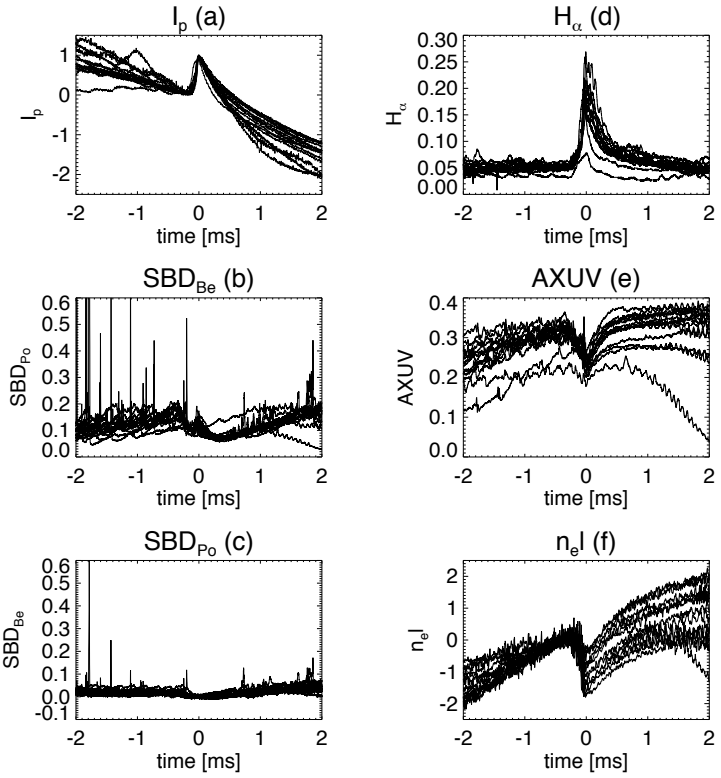

Fig. 5.17: I_p (a), SBD signal with polypropylene filter ($\mathrm{SBD_{Po}}$: sensitive up to 400 eV) (b), SBD signal with Beryllium filter ($\mathrm{SBD_{Be}}$: sensitive up to 1 keV) (c), H_α (d), AXUV (e), and $n_\mathrm{e}l$ (f) for type B.

B is the pressure gradient. However, in the case of type A, the increase of $n_e l$ cannot be seen before 0 ms. Since type A occurs at the initial and the middle of a discharges duration, the plasma temperature is probably not so high. Thus, the cause of type A seems to be different from that of type B.

The event timings for type A and B are different. For example, positive spikes for SBD signals tend to be observed at the initial of the discharges in TST-2 Ohmic plasmas. Thus, we need to check whether the differences of averaged SXR emissions for type A and B can be attributed to the difference of the timing or not. For the check, we compared two types of discharges: with type A and another without type A but showing almost the same time evolutions of plasma parameters before the timing of the IRE. As shown in Fig. 5.19, averaged SBD signals with polypropylene and beryllium filters for the latter discharge are less than 0.1 and 0.02, and these are smaller than those for the discharges with type A of IRE (see Figs. 5.18(b) and (c)). On the whole, we found that lots of positive SBD signals tend to occur before the disruptions, and this is one of the precursors of type A.

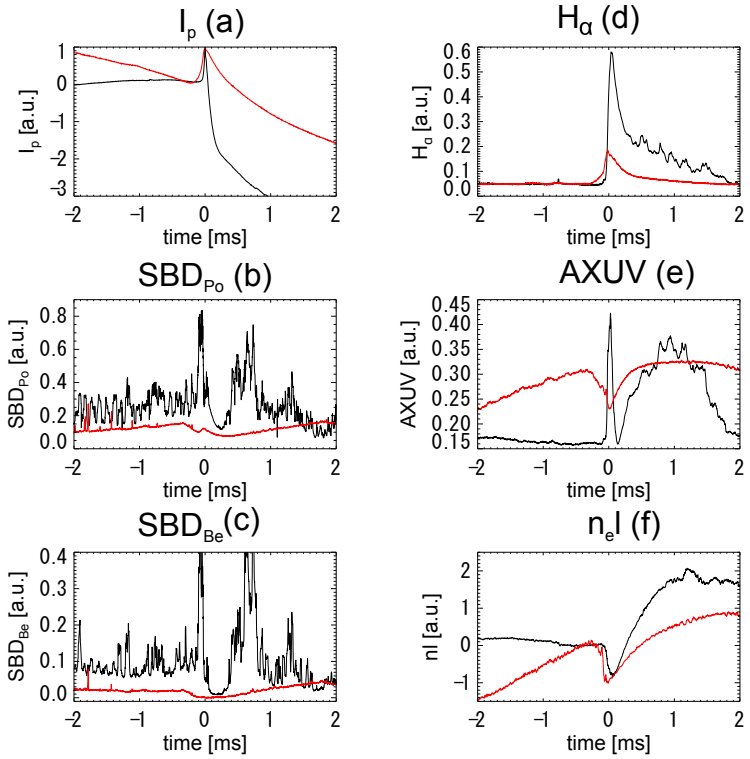

Fig. 5.18: Comparison of the averaged time evolutions of the plasma parameters for type A (black) and type B (red). I_p (a), SXR emissions ($\mathrm{SBD_{Po}}$ (b) and $\mathrm{SBD_{Be}}$ (c)), H_α (d), AXUV (e), and $n_e l$ (f) are plotted.

Fluctuations before I_p spike

We investigated the behaviors of magnetic fields and edge plasma parameters measured by the Rogowski as we did on the SXR emissions and etc. Figure 5.20 shows I_p and the magnetic fluctuations above 10 kHz and those from 1 to 10 kHz, respectively. Before the disruption (27.3 ms), the waveforms of the magnetic fluctuations above 10 kHz for type A and B are

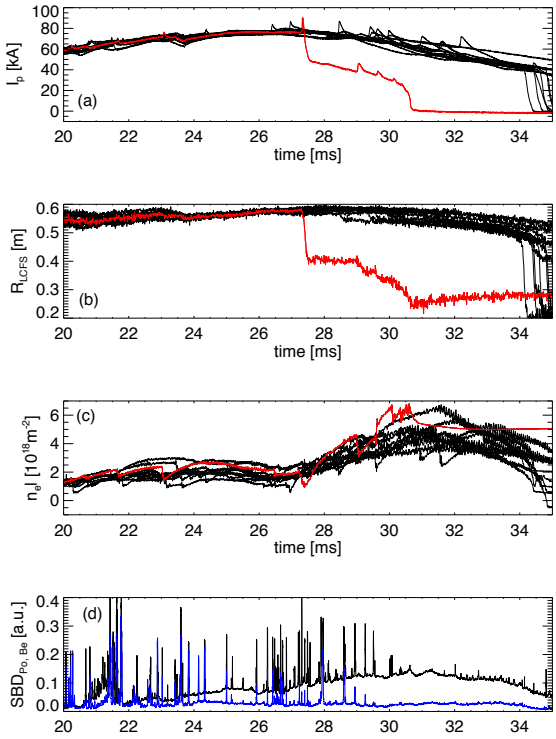

Fig. 5.19: Time evolutions of I_{p} (a), R_{LCFS} (b), $n_{\mathrm{e}}l$, and $\mathrm{SBD}_{\mathrm{Po,\,Be}}$ (d). Red curves in plots (a), (b) and (c) are the waveforms for the case with type A. Black curves in plots for (a), (b) and (c) are the waveforms for the case without type A. Plot (d) shows averaged $\mathrm{SBD}_{\mathrm{Po,\,Be}}$ (Black and blue) over the discharges without disruption.

almost the same. On the other hand, there is significant difference between the waveforms from 1 to 10 kHz (see Fig. 5.20(c)). Figures 5.20(d) and (e) show the contours of magnetic fluctuations measured by the poloidal pickup coil array, and it can be seen that the magnetic fluctuations for type A is much larger than those for type B. This difference indicates that the low frequency magnetic fluctuations can be one of the precursors of a plasma disruption. The detailed comparison of time evolutions is shown in Fig. 5.21.

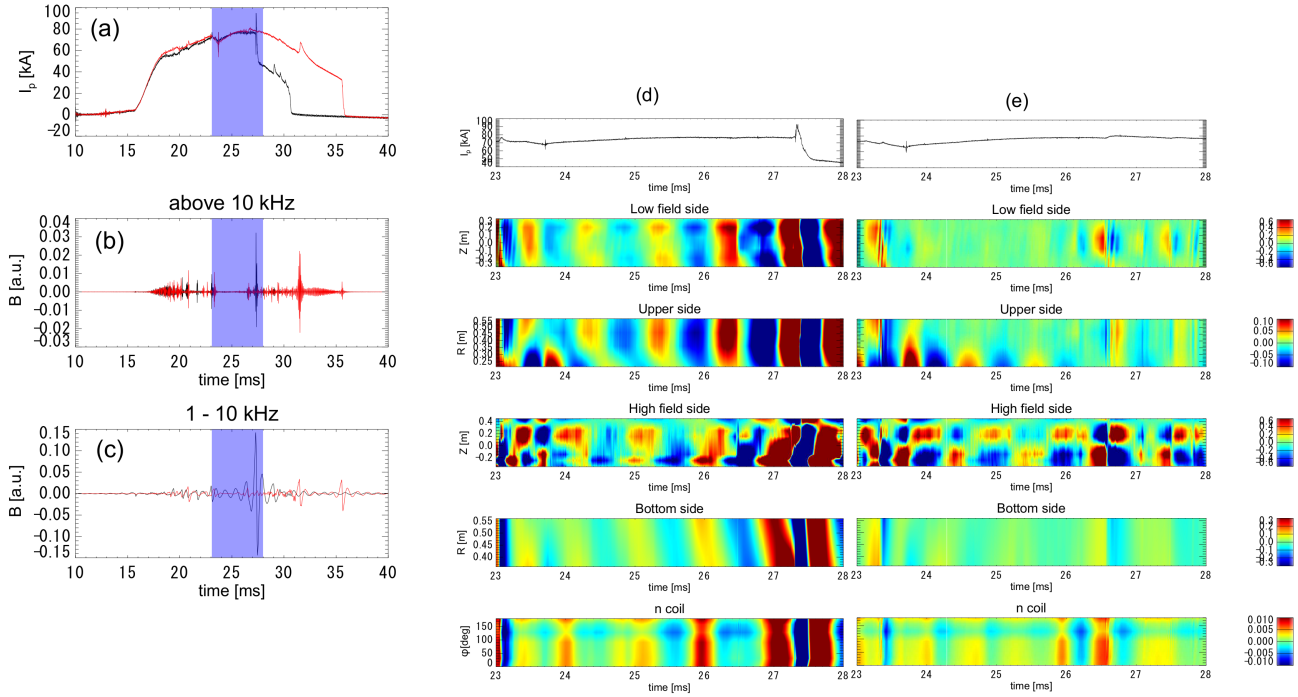

Fig. 5.20: A typical waveforms of magnetic field measured by pick-up coils located inside the vacuum vessel (R=700 mm and Z=7 mm) for the cases with type A and type B. $I_{\rm p}$ (a), poloidal magnetic field $B_{\rm p}$ fluctuations above 10 kHz (b) and from 1 to 10 kHz at $Z = 7$ mm and $R = 700$ mm (c) are shown. The time evolutions of m and n coil signals with type A (d) and B (e) are shown. The time period hatched in plots (a), (b) and (c) are plotted.

Figure 5.21 shows $B_{\rm p}$ fluctuations at $Z = 7$ mm and $R = 700$ mm for the discharges with type A and type B. To clarify the difference, fluctuations above 10 kHz and those from 1 to 10 kH are plotted in different figures (see Figs. 5.21(b), (c), (f) and (g)).

In both cases, the lower frequency fluctuations start to grow 1 ms before the $I_{\rm p}$ spikes, while the higher frequency fluctuations start to grow 0.1 ms and 0.3 ms before the spikes in type A and type B. These results suggested that lower frequency fluctuations are one of the precursors of an IRE. Especially, in the case of type A, its magnitude is quite large, and it can be considered to be one of the causes for a disruption. Thus, controlling low frequency magnetic fluctuations is an important issue to suppress disruptions induced by IRE.

We need to determine the position where such low frequency fluctuation happens. Figure 5.22 shows j fluctuations for the cases with type A and type B. Two frequency bands are plotted as in Fig. 5.21. High frequency fluctuations for j are seen before 0 ms for both cases. This is similar to the result of magnetic fluctuations. However, low frequency fluctuations

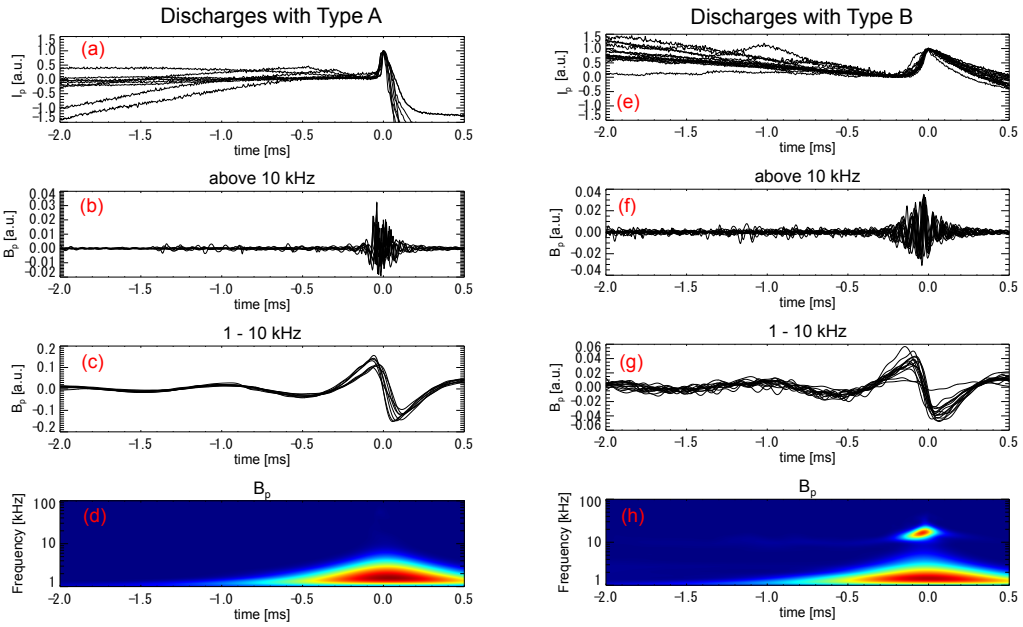

Fig. 5.21: Time evolutions of $I_{\rm p}$ (a) and (e), higher frequency $B_{\rm p}$ fluctuation (b) and (f), lower frequency $B_{\rm p}$ fluctuation from 1 to 10 kHz (c) and (g), and power spectrum density for $B_{\rm p}$ above 1 kHz (d) and (h) are plotted. For the comparison, the peak timings of the each $I_{\rm p}$ spike are set to be 0 ms.

for j cannot be identified for both cases (see Figs. 5.22(d) and (h)). From Figs. 5.22(c) and (g), the increases of j near the plasma edge region seem to start from 0.1 and 0.3 ms before the $I_{\rm p}$ spike. This is the current transported from the core region to edge region due to the IRE. From Fig. 5.18(f), the decreases of $n_{\rm e}l$ before $I_{\rm p}$ spike are seen and they start from 0.1 and 0.3 ms before the $I_{\rm p}$ spike. These timings are the same as those of the increase of edge j. In general, current and pressure flattenings occur as a result of IRE [86], and q profile is also changed. In Fig. 5.22, high frequency fluctuations start after the low frequency j fluctuation and the decrease of $n_{\rm e}l$. Since q, current and pressure profiles are related to some kinds of plasma instabilities, high frequency j fluctuations are probably the results of the changes of them.

Figures 5.23 and 5.24 show the time evolutions of $I_{\rm is}$ and $V_{\rm f}$ during the IRE. As in the case of j fluctuations, low frequency fluctuations are not clearly seen, but, the increase of $I_{\rm is}$, abrupt changes of $V_{\rm f}$, and high frequency fluctuations are clearly observed.

In Ref. [18], the relationship between $\Delta I_{\rm p}$ and the plasma parameters are investigated and it was found that $\Delta I_{\rm p}$ and the increase of ion temperature $T_{\rm i}$ during IREs showed almost linear relationships. As shown in Fig. 5.14, j fluctuates in both positive and negative directions and it is important to know which physical parameters are correlated to Δj. Figure 5.25 shows the relationship between Δj measured by the Rogowski 1 and 2 (a), and the relationship between $\Delta I_{\rm p}$ and Δj. It was found that inner Δj (Rogowski 1) are larger than outer Δj (Rogowski 2) for both type A and type B. From Fig. 5.25(b), a rough linearity between $\Delta I_{\rm p}$ and Δj can be seen. In Ref. [18], $\Delta I_{\rm p}$ is introduced as a good indicator for the degree of IRE strength. The linearity between $\Delta I_{\rm p}$ and Δj indicate that the edge instabilities becomes large when the magnitude of IRE is large.

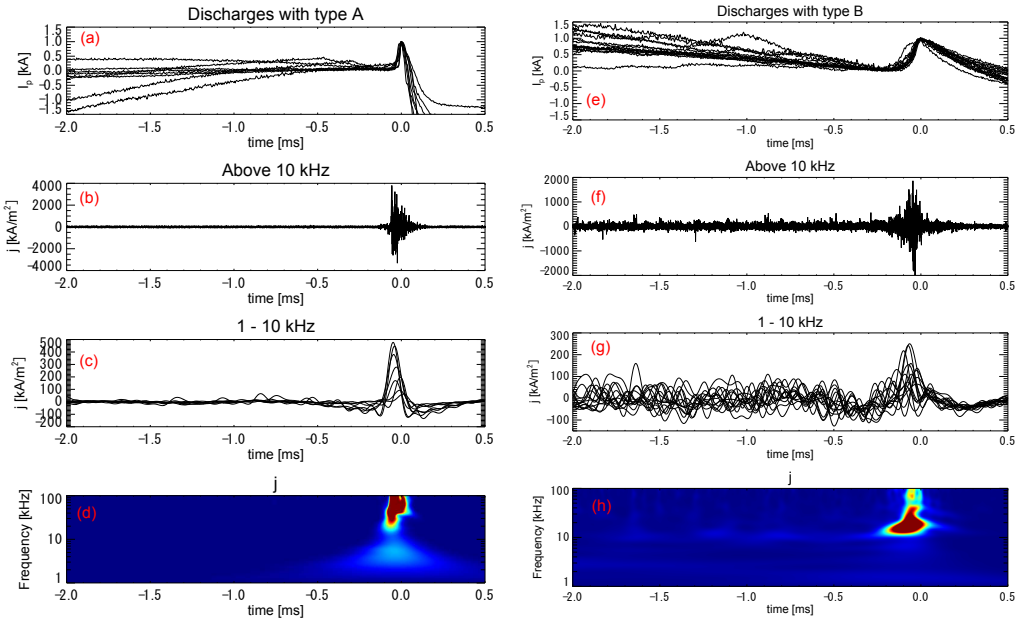

Fig. 5.22: Time evolutions of j fluctuations measured by Rogowski 1 (located at $Z = 0$ mm and $R = 551$ mm) for the discharges with type A and type B. $I_{\rm p}$ (a) and (e), j fluctuations above 10 kHz (b) and (f), j fluctuations from 1 to 10 kHz (c) and (g), and power spectrum densities for j above 1 kHz are shown. For the comparison, the peak timings of the $I_{\rm p}$ spikes shot are set to be 0 ms.

Figure 5.26 shows radial Δj profiles, where the horizontal axis represent the radial distance between the measurement position and the Last Closed Flux Surface position. The figure indicates that quite large current flows near $R_{\rm LCFS}$ during IREs. For example, a typical current density at the core region is about 1 MA/m^2, and the maximum of the observed Δj is much larger than this typical j.

Lastly, we summarize the time sequence before $I_{\rm p}$ spike as follows:

1. The growth of low frequency magnetic fluctuations at the core region before 1 ms.
2. The increase of the current density at the edge region and decrease of $n_{\rm e}l$ at 0.1 and 0.3 ms before $I_{\rm p}$ spike for type A and B, respectively.
3. The growth of the high frequency fluctuations (B, j, $n_{\rm e}$ and $V_{\rm f}$).
4. The decay of the high frequency fluctuations and start of $I_{\rm p}$ spike.

The differences of type A and B of IREs are as follows:

- The number of sudden positive spikes in SBD signals before $I_{\rm p}$ spikes.
- The magnitude of low frequency magnetic fluctuation.

These results suggest that controlling sudden SXR emissions and low frequency fluctuations at the core region is important to suppress the disruption in TST-2 Ohmic discharges.

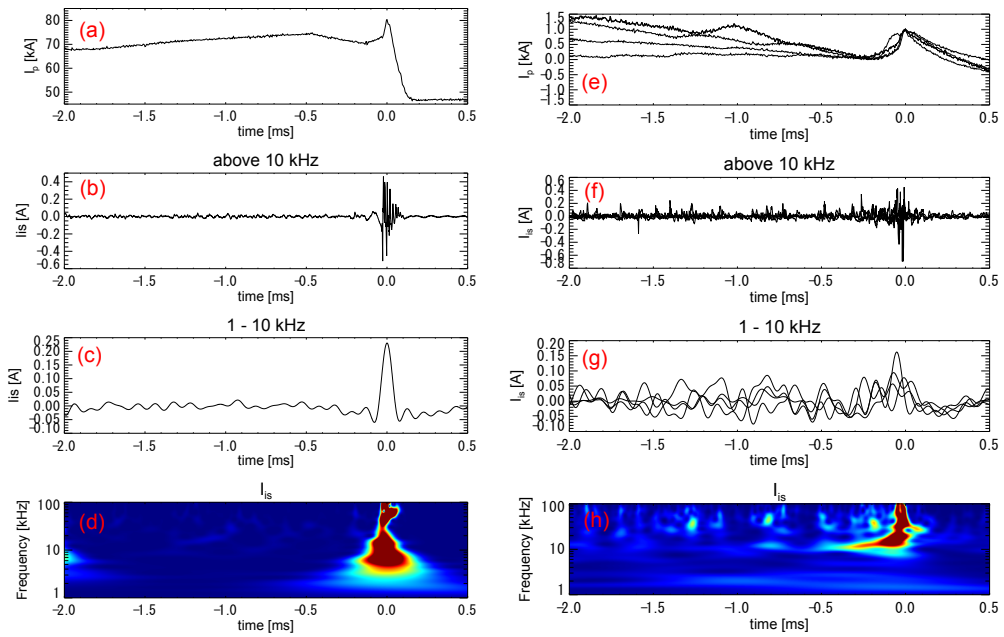

Fig. 5.23: $I_{\rm is}$ fluctuations measured by Electrode 2 (located at $Z = 0$ mm and $R = 582$ mm) for the discharges with type A and type B. $I_{\rm p}$ (a) and (e), $I_{\rm is}$ fluctuations above 10 kHz (b) and (f), $I_{\rm is}$ fluctuations from 1 to 10 kHz (c) and (g), and power spectrum densities for $I_{\rm is}$ above 1 kHz are shown. For the comparison, the peak timings of the $I_{\rm p}$ spikes are set to be 0 ms.

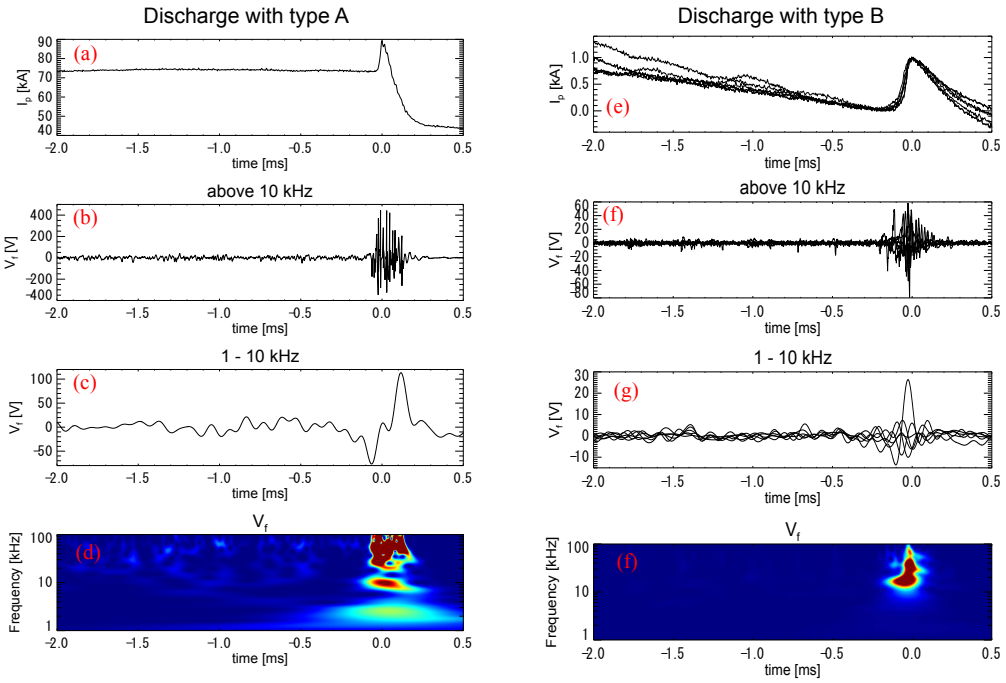

Fig. 5.24: V_f fluctuations measured by Electrode 2 (located at $Z = 0$ mm and $R = 582$ mm) for the discharges with type A and type B. I_p (a) and (e), V_f fluctuations above 10 kHz (b) and (f), V_f fluctuations from 1 to 10 kHz (c) and (g), and power spectrum densities for V_f above 1 kHz are shown. For the comparison, the peak timings of the I_p spikes are set to be 0 ms.

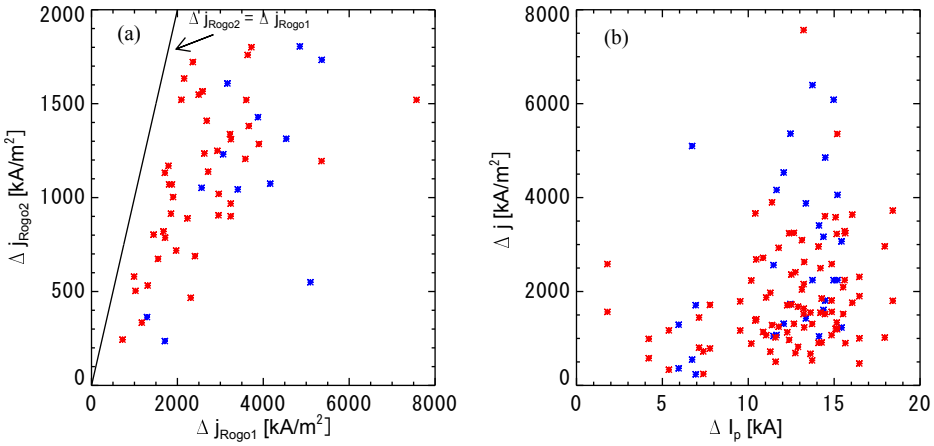

Fig. 5.25: The relationship between Δj measured by the Rogowski 1 and 2 (a), and the relationship between ΔI_p and Δj. Blue and red symbols represent the cases with type A and type B, respectively. Black line in (a) represents $\Delta j_\mathrm{Rogowsk2} = \Delta j_\mathrm{Rogowsk1}$.

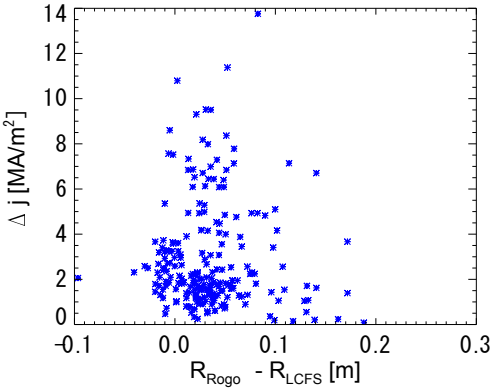

Fig. 5.26: Radial Δj profile. The horizontal axis represents the distance between the radial location of the Rogowski 1 and 2 R_{Rogo} and R_{LCFS}.

5.4.4 Negative current and filamentary structures during IRE

The generation of filamentary structures during IRE is predicted by a 3 dimensional MHD simulation, and such structure was observed using a fast visible camera in START experiment [25]. Similar to Ref. [25], filamentary structures were detected using a fast visible light camera (FastCAM-512PCI 32K, Photoron) in TST-2 Ohmic discharge as shown in Fig. 5.27. This experiment was carried out without the Rogowski probe insertion. Figure 5.27(b) shows the time sequence of the visible image of the whole plasma. At 13 ms (5.27(b) I), the plasma is in steady state and the emission is dark, then the emission becomes bright with the increase of I_{p} (Fig. 5.27(b) II). The size of plasma in 13.25 ms is much larger than those in the others. After the I_{p} spike, the emission becomes dark again. Figure 5.27(c) shows the enlarged view at 13.25 ms, and we can see the filamentary structure crossing the RF antenna area (blue arrow). The height of the RF antenna in Z direction is 60 cm, and the width of the filamentary structure in Z direction is less than about 20 cm. In Fig. 5.27(b) IV, a helical structure can also be seen.

We also performed measurements using the fast visible camera with 100,000 fmps (see Sec. 1.5.4) to see the visible light emission around the Rogowski probe during the IRE (see Fig. 5.28). The experimental geometry is shown in Fig. 5.1. In order to see the time relationshiips precisely, time evolutions of the visible light emission, I_{p} and j were recorded by the same data acquisition system (MEMRECAM HX-3, NAC Image Technology. Inc.) and the clock time for these data acquisition was adjusted to be the same. Thus, there is no time delay for the data shown in Fig. 5.28. During the spikes and large fluctuations of j, strong visible light emissions are observed. These emissions are probably due to the impurity emissions caused by the electron hitting the ceramics cover of the Rogowski probe head. When j becomes negative, the inversion of the visible light emission area is seen. This result indicate that the negative j is not a noise signal but it is the real current signal. The strong visible light emission region in radial direction is about 5 cm in the R direction. Thus, the radial size of the filamentary structure is greater than 5 cm. In Fig. 5.26), lots of data points are in $0 < R < R_{\mathrm{LCFS}} + 5\mathrm{cm}$. The estimation from the visible light image is consistent with the radial Δj profile. As a result, the size of the filamentary structure during the IRE was about 20 cm $\times$ above 5 cm in Z and R directions. We found that the local current

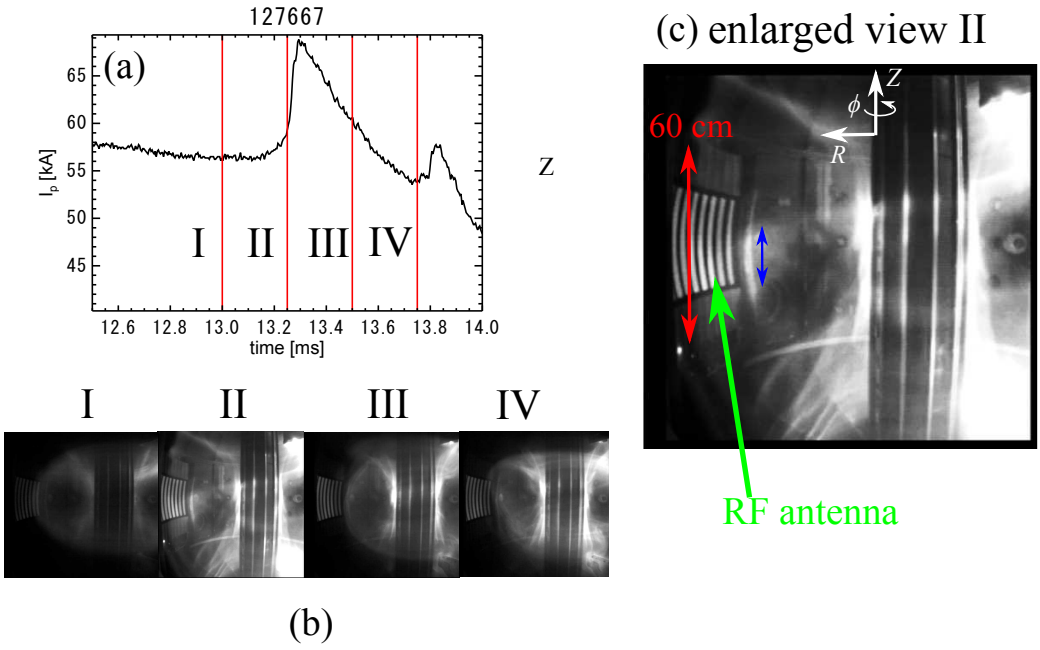

Fig. 5.27: Visible light image during an IRE. (a) I_p, (b) visible light images (I, II, III, IV), and (c) enlarged view for the picture of II.

flowing both positive and negative direction during the IRE. Such bipolar currents are the first observations in spherical tokamak plasmas.

5.4.5 Filamentary structures during Phase 1

During Phase 1, we also detected filamentary structure during Phase 1 by the fast visible camera (1,6000 fmps). Figure 5.29 shows the time evolutions of I_p and dB/dt (Z = 7 mm and R = 700 mm), and the visible light images in the peripheral region during Phase 1. As shown in Figs. 5.29(b) and (c), the magnetic field is oscillating with frequencies from 10 to 20 kHz, and clear filamentary structures localized at plasma edge regions are observed (Fig. 5.29(d)). The height of the bright filamentary structure near the antenna is about about 5 cm. In addition, the filamentary structure in the upper region of Fig. 5.29(d)I crosses the antenna area during 3 frames (i.e., the elapse time for the crossing is about 0.1875 ms). Thus, the velocity of the filamentary structure in θ direction (poloidal direction, see Fig. 1.2) is estimated to be about 2 km/s. The vertical distance between the two adjacent filamentary structures is about 20 cm (see Fig. 5.29(d) I), and the frequency of the filamentary structure crossing the equatorial plane is 10 - 20 kHz. This is the consistent with the frequency of the magnetic fluctuation (see Fig. 5.29(c) and (d)). Since the correlation between the fluctuations of dB/dt and j is high (Fig. 5.11(a)), it is suggested that the fluctuation of j in Phase 1 reflects signal due to the filamentary structures passing through the Rogowski probe region. Figure 5.30 shows radial profile of the amplitude of j fluctuation during Phase 1 obtained from various plasma discharges. In Fig. 5.30, radial profile of the rms amplitude of j fluctuation is shown. The j fluctuation is localized near R_{LCFS} with a width of 3 to 5 cm, the peak value is almost 20 kA/m^2. During Phase 1, typical value of j near the plasma edge (equilibrium current) is less than 100 kA/m^2. By multiplying the peak current density 20 kA/m^2 and the

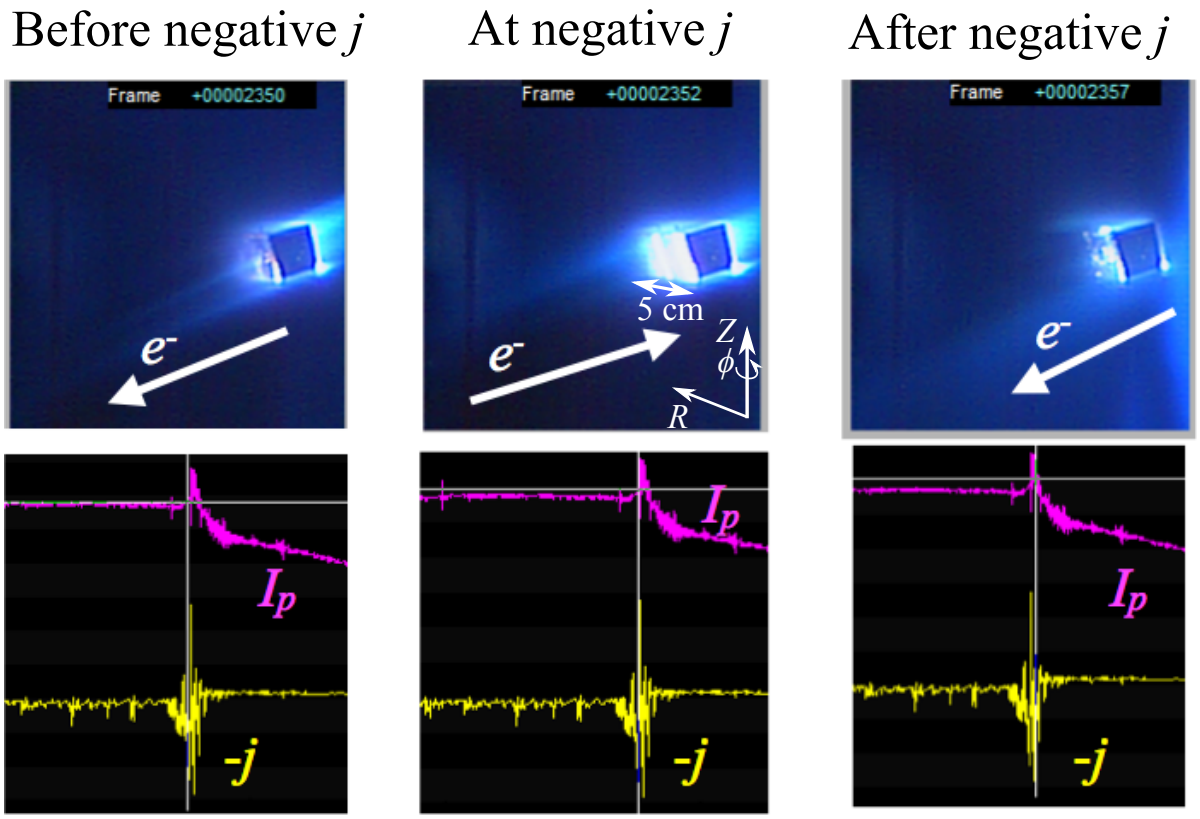

Fig. 5.28: Time sequence of the visible light emission from the Rogowski probe during IRE.

are 5 cm × 5 cm the total current of the filament becomes 50 A, and it carries the current comparable to more than 20% of equilibrium current.

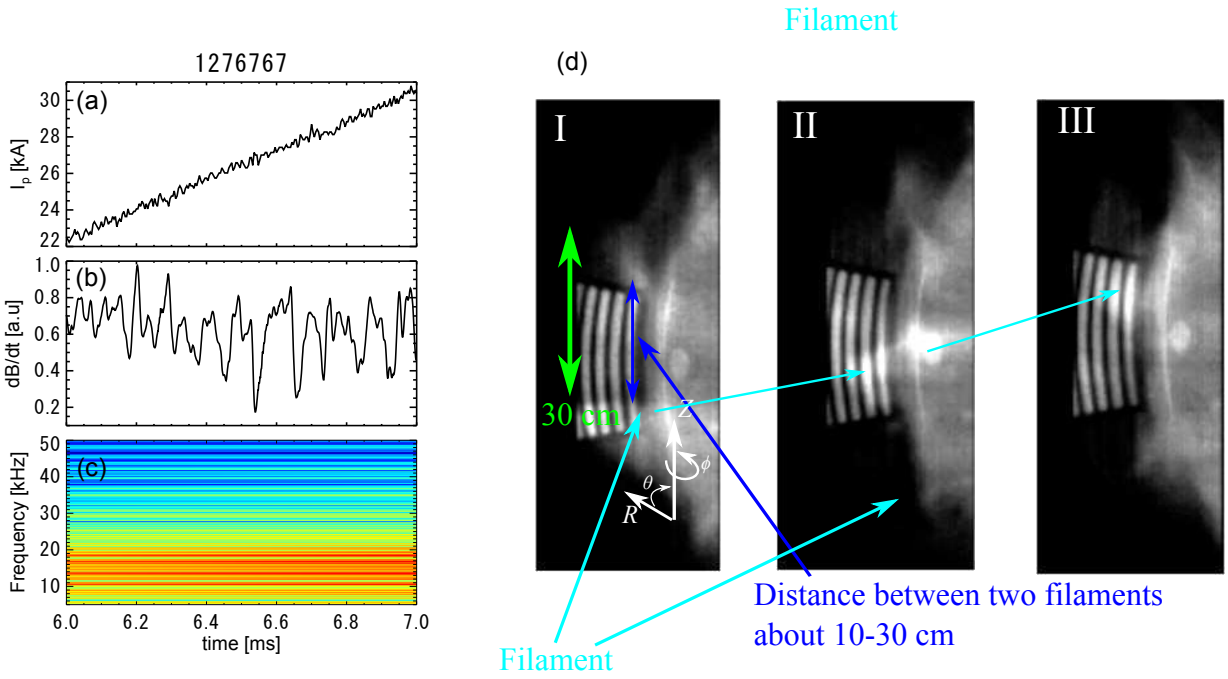

Fig. 5.29: Magnetic fluctuation and visible light emission during Phase 1. (a) plasma current $I_{\rm p}$, (b) magnetic fluctuation dB/dt, and (d) visible light images in the plasma edge.

Figure 5.31 shows time evolutions of $I_{\rm p}$ and m coil signals for a certain Ohmic plasma discharge. From m coil signal, it can be seen that magnetic fluctuations propagate from bottom side to upper side, and this direction is consistent with the direction of the filamentary structure crossing the antenna area.

5.4.6 Analisys for sudden spikes for j

In this section, analysis of the sudden spikes during Phase 2 in TST-2 Ohmic discharges is represented. We found that the sudden spikes in j and $n_{\rm e}$ show a good correlation. There are two possible causes for these sudden spikes. One is simple increase of j and $n_{\rm e}$ at the edge region. Second is that the generation of high density localized structure, and it crosses the Rogowski probe head. In order to verify the cause, we compared the signals measured by the Rogowski probe and mach probe (see Sec. 5.1). Using Electrodes A and B of the mach probe, toroidal asymmetry of $I_{\rm is}$ can be measured. Figure 5.32 shows the typical time evolution of j, dB/dt, $I_{\rm is}$, and fluctuations of $\tilde{n_{\rm e}}l$ measured by the interferometer during Phase 2. The visible light images (100,000 fmps) near the Rogowski probe head are also shown. All signals are correlated with the spikes of dB/dt. Here, we can see that $\tilde{n_{\rm e}}l$ increases before the spikes and decreases at the spikes. In addition, the toroidal asymmetry in $I_{\rm is}$ measured by Electrodes A and B is seen. If these spikes are caused by a simple increase of electron density at the edge region, the toroidal asymmetry of $I_{\rm is}$ (Fig. 5.32(c)) should not be observed. Thus, these sudden spikes cannot be explained by the simple increase of electron density at the edge region. From the time evolutions of $\tilde{n_{\rm e}}l$ and $I_{\rm is}$ (the Electrode A), we can see that a high

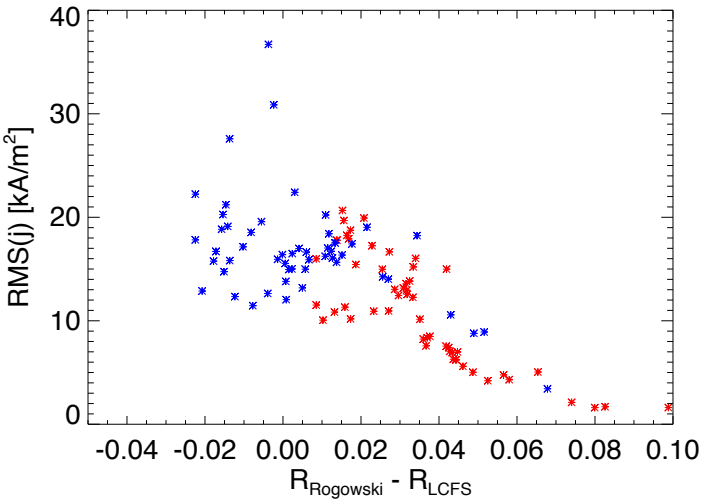

Fig. 5.30: Radial profile of the RMS j amplitude during Phase 1. Many discharges are used to make this plot. The horizontal axis represents the distances between $R_{\mathrm{Rogowski\ 1,\ 2}}$ and R_{LCFS} for each discharge. Blue and red symbols represent the data measured by Rogowski 1 and 2, respectively.

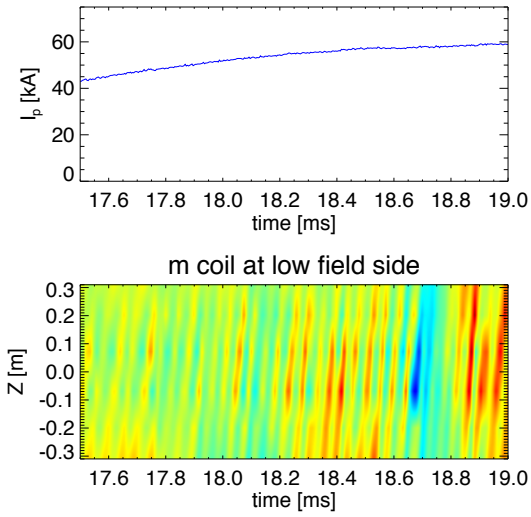

Fig. 5.31: Time evolutions of I_{p} and m coil signals for a certain Ohmic discharge.

density structure is produced in the core region at first, then, it is transported to the edge region. Since the Electrode A is exposed to the direction of the electron flow (see Fig. 5.2), it can be inferred that this asymmetry is due to the high density structures, which carrie a current, crossing around the Rogowski probe head.

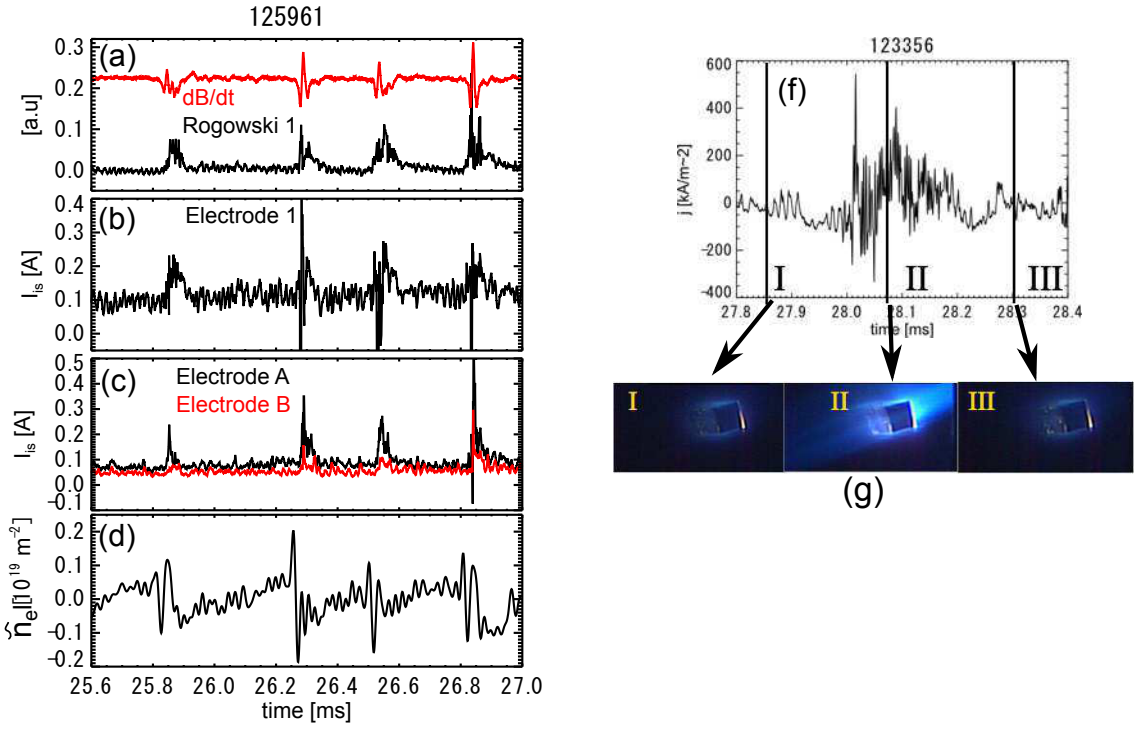

Fig. 5.32: A typical time evolutions of j above the frequency with 1 kHz, dB/dt (a), $I_{\rm is}$ ((b) and (c)), and fluctuations of line integrated density $\tilde{n_{\rm e}}$ measured by the interferometer (e) during Phase 2, enlarged view of (a) (f), and the visible light emissions (g). j and $I_{\rm is}$ were measured at the same radial location (R = 551.5 mm).

Figure 5.33 shows a typical time evolution of $\theta_{\rm B}$ measured by pick-up coil 1 during Phase 2. We can see that $\theta_{\rm pitch}$ near the Rogowski 1 does not vary largely during the sudden spikes. Since the angle sensitivity is not too sharp, the sudden spikes in j cannot be explained by the sudden change in $\theta_{\rm B}$.

Figure 5.34 shows the relationship between Δj (peak to peak amplitude) and $\Delta n_{\rm e}$ at sudden spikes. Δj shows the magnitude of the amplitude of j during the spikes, and $\Delta I_{\rm is}$ is the increase of $I_{\rm is}$ before the spikes. Since we found that $T_{\rm e}$ does not abruptly change during the spikes (see Fig. 5.12), we calculated $n_{\rm e}$ using a typical $T_{\rm e}$ at the plasma edge region (40 eV). Clear linearity was obtained between Δj and $\Delta n_{\rm e}$. From the slope of this result, electron drift velocity $v_{\rm d,\,e}$ ($j = -en_{\rm e}v_{\rm d,\,e}$) can be roughly estimated to be 2000 km/s. In TST-2 Ohmic plasma discharges, typical j and $n_{\rm e}$ at the plasma edge is 200 kA/m^2 and 2.5 $\times$ 10^{18} m^{-3}, and typical $v_{\rm d\,e}$ is calculated as 500 kAm/s. Thus, at the spikes, we found that structures which has a similar density as the background edge density and high $v_{\rm d,\,e}$, crosses across the Rogowski probe head.

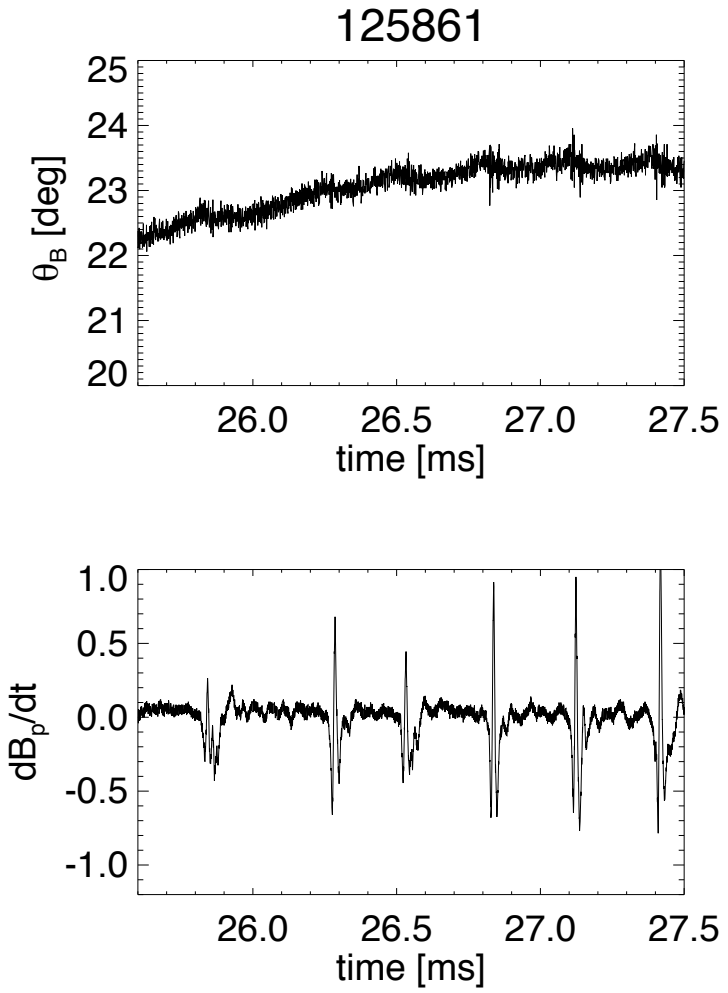

Fig. 5.33: A typical time evolution of $\theta_{\rm B}$ during Phase 2. (a) time evolution of $\theta_{\rm pitch}$ measured by pick-up coil 1 and (b) time evolution of $dB_{\rm p}/dt$ at $Z = 7$ mm and $R = 700$ mm.

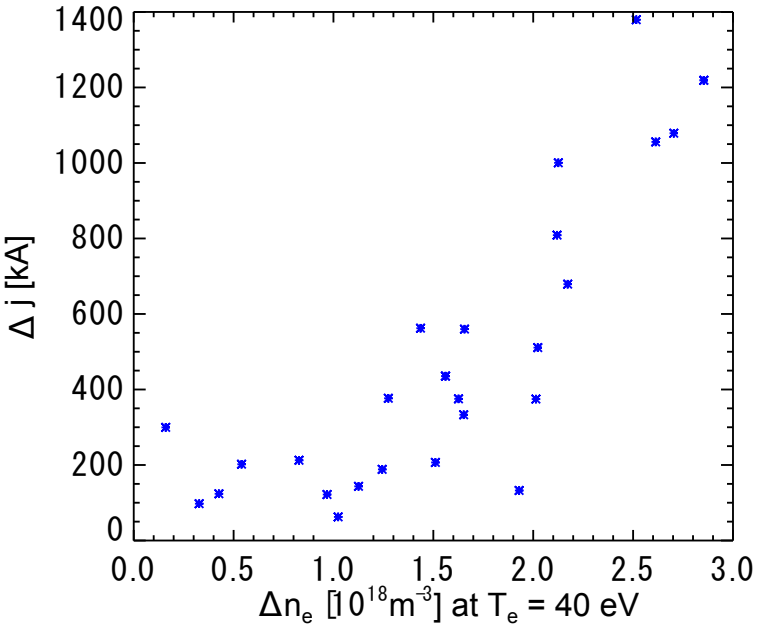

Fig. 5.34: Relationship between Δj and Δn_{e} at the spikes. Δj shows the peak to peak amplitude during the spikes, and Δn_{e} is the increase of the electron density from n_{e} before the spikes.

Chapter 6

Discussion

6.1 Rogowski coil vs magnetic probe array

In the previous chapters, we presented the results of the current density j measurement using the Rogowski probe. In Sec. 1.6, we reviewed current density diagnostics in tokamak study, and we also discussed the j measurement uncertainties for a pick-up coil array. We have pick-up coils on the Rogowski probe head, and the comparison between the current densities measured by using the Rogowski coil and by using the pick-up coils is presented in this section.

In pick-up coil array diagnostic, the spacial differentiations of poloidal and radial magnetic fields must be performed ($\mu_0 j_\mathrm{t} = dB_\mathrm{p}/dR - dB_\mathrm{R}/dZ$, where μ_0 is the magnetic permeability, B_p is poloidal magnetic field and B_R is radial magnetic field). By assuming that the shape of the poloidal magnetic flux surface is a circle, we can use cylindrical coordinate and dB_R/dZ can be given by [63, 64]

$$\frac{dB_\mathrm{R}}{dZ} = \frac{B_\mathrm{p}}{a}, \tag{6.1}$$

where a is the radius of curvature of the magnetic field at the position of the pick-up coil. By using pick-up coils located on the Rogowski probe head, B_p can be measured directly, and dB_R/dZ can be calculated from the EFIT code. Using these values and Eq. 6.1, we can estimate a. As a result, j_t can be calculated.

As described in Chap. 4, the Rogowski coil diagnostic has an dependence on the angle between the directions of the hole and the magnetic field B and it was found that the angular dependence is affected by the plasma sheath formed on the boundary region between plasmas and the ceramic surface, which covers with the Rogowski probe head. Thus, in order to calculate j_t from the Rogowski coil signal, it is needed to consider these effects. From the study of the plasma sheath effect on the Rogowski probe measurement, a typical width of the angular dependence is found to be about 11°. Since we have pick-up coils on the Rogowski probe head, we can measure magnetic pitch angle θ_B and we can estimate the angle between the directions of the hole and B. Since θ_B and θ_j (the pitch angle of the current density) agree each other within ±1° near the plasma edge, the difference between the measured current density j_Rogo and $j_\parallel$ (current density flowing in parallel to the magnetic field direction). Considering above, $j_{\mathrm{t,\,Rogo}}$ can be calculated by

$$j_{\parallel,\,\mathrm{Rogo}} = j_\mathrm{Rogo}(\theta)/\exp\left(-\left(\frac{\theta-\theta_\mathrm{B}}{11}\right)^2\right), \tag{6.2}$$

$$j_{\mathrm{t,Rogo}} \quad = \quad j_{\parallel,\ \mathrm{Rogo}} \cos(\theta_{\mathrm{B}}). \tag{6.3}$$

where $j_{\mathrm{Rogo}}(\theta)$ is the current density passing through the hole of the Rogowski coil at finite θ, a factor of $\exp\left((\theta - \theta_{\mathrm{B}}/11)^2\right)$ represents the Gaussian function term. $j_{\parallel,\ \mathrm{Rogo}}$ is the parallel current along the magnetic field estimated by using Eq. 6.2. Finally, we can estimate $j_{\mathrm{t},\ \mathrm{Rogo}}$ using Eq. 6.3.

Figure 6.1(a) shows the comparison of toroidal current densities of $j_{\mathrm{t},\ \mathrm{Rogo}}$, $j_{\mathrm{t},\ \mathrm{pick}}$ and $j_{\mathrm{t},\ \mathrm{EFIT}}$, which is the current density calculated by EFIT code. The comparison is performed for the inboard-limited plasma discharges since we demonstrated that EFIT code in TST-2 can be employed precisely in this case. A rough agreement between $j_{\mathrm{t},\ \mathrm{Rogo}}$ and $j_{\mathrm{t},\ \mathrm{pick}}$ for the region of 50 kA/m^2 $\leq j_{\mathrm{t}} \leq$ 100 kA/m^2 can be seen. On the other hand, there is a tendency that $j_{\mathrm{t},\ \mathrm{Rogo}}$ becomes much larger than $j_{\mathrm{t},\ \mathrm{pick}}$ for the region of $j_{\mathrm{t}} \geq$100 kA/m^2. On the other hand, $j_{\mathrm{t},\ \mathrm{Rogo}}$ and $j_{\mathrm{t},\ \mathrm{EFIT}}$ agree. The data points in the region of 50 kA/m^2 $\leq j_{\mathrm{t}} \leq$ 100 kA/m^2 were obtained from the initial phase of the discharge durations. In this time periods, the shape of the poloidal magnetic flux surface is almost circular (see Fig. 6.1(b) 20 ms). On the other hand, at the middle phase of discharge durations, the current density near the plasma edge region is $j_{\mathrm{t}} \geq$100 kA/m^2 and the shape of the poloidal magnetic flux surface deviates from a circle (see Fig. 6.1(b) 27 ms). Thus, in this time period, the estimation of a_{EFIT} is difficult and the assumption of a cylindrical symmetry is not satisfied. Since we have evaluated all noises for the Rogowski probe such as the magnetic field, electrostatic fluctuation and the sheath effect, the current value passing through the hole is quite reliable. In addition, the measurement accuracy of the magnetic field using pick-up coils is within 3% (see Sec. 3.3). Thus, the large deviation between $j_{\mathrm{t},\ \mathrm{Rogo}}$ and $j_{\mathrm{t},\ \mathrm{pick}}$ is considered due to the error in the estimation of the magnetic spatial differentiation.

6.2 Measurement of $\boldsymbol{j} \times \boldsymbol{B} = \nabla p$

The feature and the advantage of the diagnostic using a Rogowski probe is the direct measurement. In addition, it also has a high directionality for the measurement of current density direction. When a magnetically confined plasma is in the equilibrium state, the electromagnetic force and the pressure gradient force are balanced ($\boldsymbol{j} \times \boldsymbol{B} = \boldsymbol{\nabla} p$). When there is a finite pressure gradient, the current density direction and the magnetic field direction must be different due to the diamagnetic current j_{D}. By employing the Rogowski probe in TST-2 Ohmic discharges, it is possible to investigate the capability of the measurement of j_{D}. For the investigation, we performed the angular dependence measurement (as shown Sec 3.5) for three types of TST-2 Ohmic discharges (low, middle and high I_{p} cases) shown in Fig. 6.2. In these experiments, we also measured the electron pressures using the Electrodes 1 and 2. The radial pressure gradients in the low and the middle I_{p} cases are almost the same. On the other hand, from 25 to 30 ms, pressure gradient for high I_{p} case is about twice larger than the others. Figure 6.3(a) shows the relationship between θ_{j}, θ_{B}, and the difference of the electron pressure P_{e} measured by the Electrode 1 and 2 (P_1 - P_2). When the pressure difference is from 4 to 12 Pa, θ_{j} and θ_{B} agreed each other within $\pm 1^{\circ}$. On the other hand, we can see that θ_{j} deviates from θ_{B} by about 2° when the pressure difference is large ($\geq$ 14 Pa). As described in Sec. 3.5, near the outboard LCFS, the pressure gradient force ($-\boldsymbol{\nabla} p$) is directed outward so the electromagnetic force $\boldsymbol{j} \times \boldsymbol{B}$ must be directed inward. Thus, θ_{B} should be slightly larger than θ_{j}. This tendency is consistent with the expectation. Figure 6.3(b) shows the angle dependence for a representative case where the angle difference more than is 2°, and it is clearly shown that the Gaussian fitting is good enough to show that 2°

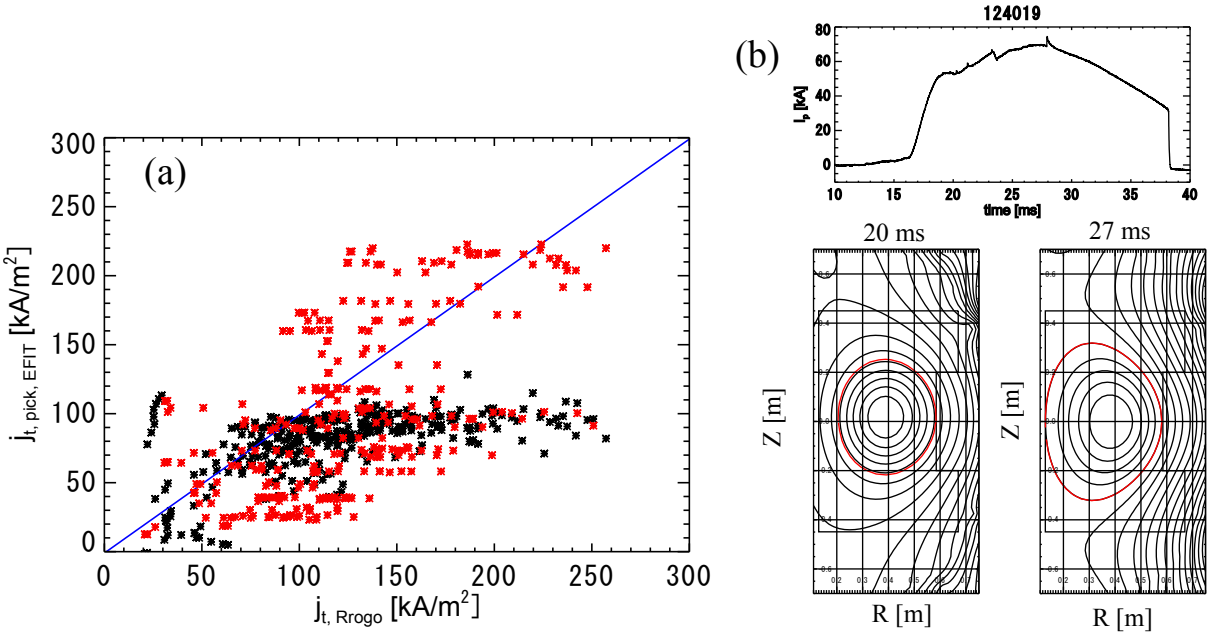

Fig. 6.1: Comparison between j_t measured by the Rogowski 1 $j_{t,\ Rogo}$ and j_t deduced by pick-up coil 1 and 2 $j_{t,\ pick}$ and EFIT code $j_{t,\ EFIT}$ (a). Black and red symbols represent $j_{t,\ pick}$ and $j_{t,\ EFIT}$. The data points were averaged over 1 ms. The waveform of the plasma current and the poloidal magnetic surfaces at 20 ms and 27 ms are also shown (b).

is much larger than the error in the peak angle. Using the values: j, B and dP_e/dR where P_e is the electron pressure, the angle difference $\Delta\theta$ is

$$\Delta\theta = \sin^{-1}\left(\frac{d(P_e + P_i)/dR}{|j||B|}\right), \tag{6.4}$$

where P_i is the ion pressure. Assuming that $P_e = P_i$ ($dP \sim 30$ Pa), and typical $|j|$ and $|B|$ are 200 kA/m^2 and 0.15 T, respectively, the $\Delta\theta$ is estimated to be about 1.85° and it is almost consistent with the experimental result.

In the next, we need to discuss whether it is possible to measure j_D using a Rogowski coil or not. In principle, j_D is the current which is produced by Larmor orbits. If the electrons pass through the hole of the Rogowski probe very slowly, they have enough time to describe a lot of Larmor orbits inside the hole and j_D can be 0 averaging over the time periods for the electrons to pass through. On the other hand, when the electrons have much higher parallel velocity, j_D can be finite as follows. In Figs. 6.4(a) and (b), 3 electron Larmor orbits inside of the hole of a Rogowski coil are considered in the presence of ∇n_e. Circles and squares show the hole of a Rogowski coil and arrows show electron orbit. The directions of the hole and B are considered to be the parallel. In Fig. 6.4(a), the case with a slow parallel velocity is considered, and from $x - y$ plane, we can easily see no finite j_D. In Fig. 6.4(b), the case with high parallel velocity is considered. In this case, electrons have insufficient time to make one Larmor orbit inside the hole. Thus, when there is ∇n_e in y direction, total current in x direction can be finite and this is the diamagnetic current. In TST-2 Ohmic plasma discharges, typical cyclotron frequency f_{ce} is ∼2.45 GHz, and the thickness of the Rogowski 1 and 2 are is 21 mm. Using these values, we can calculate the condition for the electrons

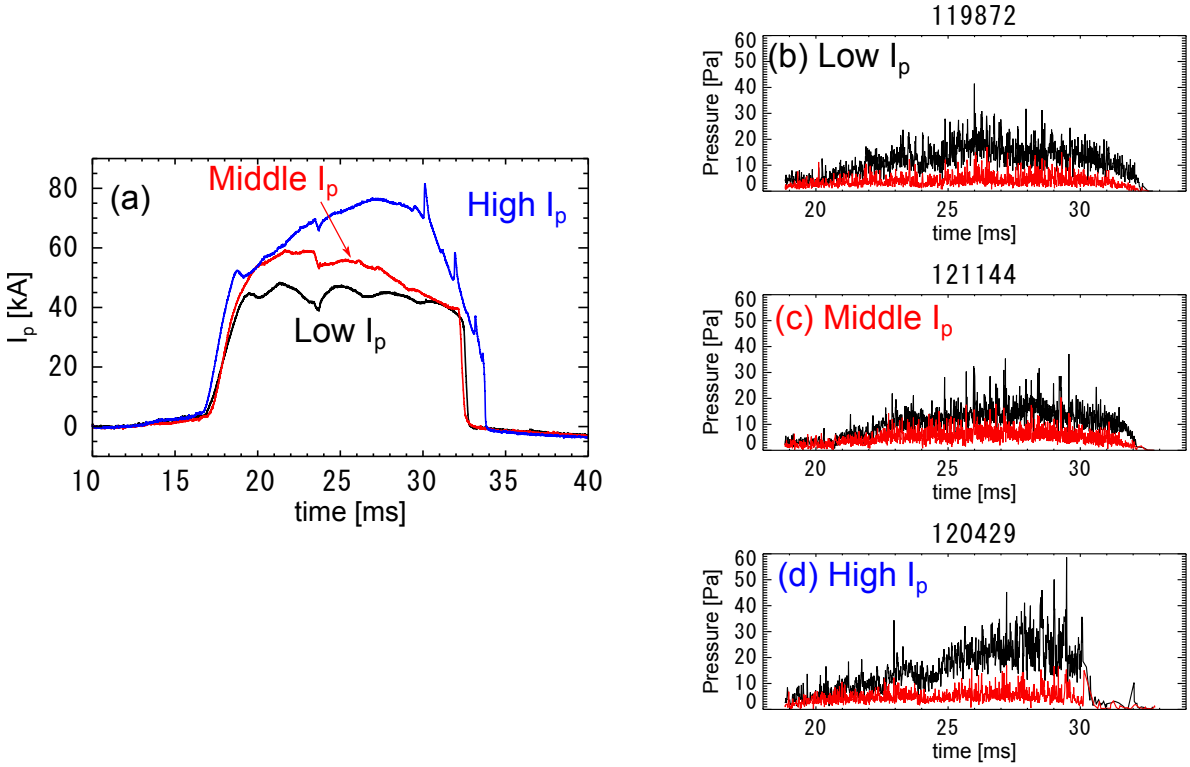

Fig. 6.2: Plasma current I_p for three types discharges (low, middle and high I_p cases) (a). Figures (b), (c) and (d) show the electron pressure measured by the Electrode 1 (black) and 2 (red).

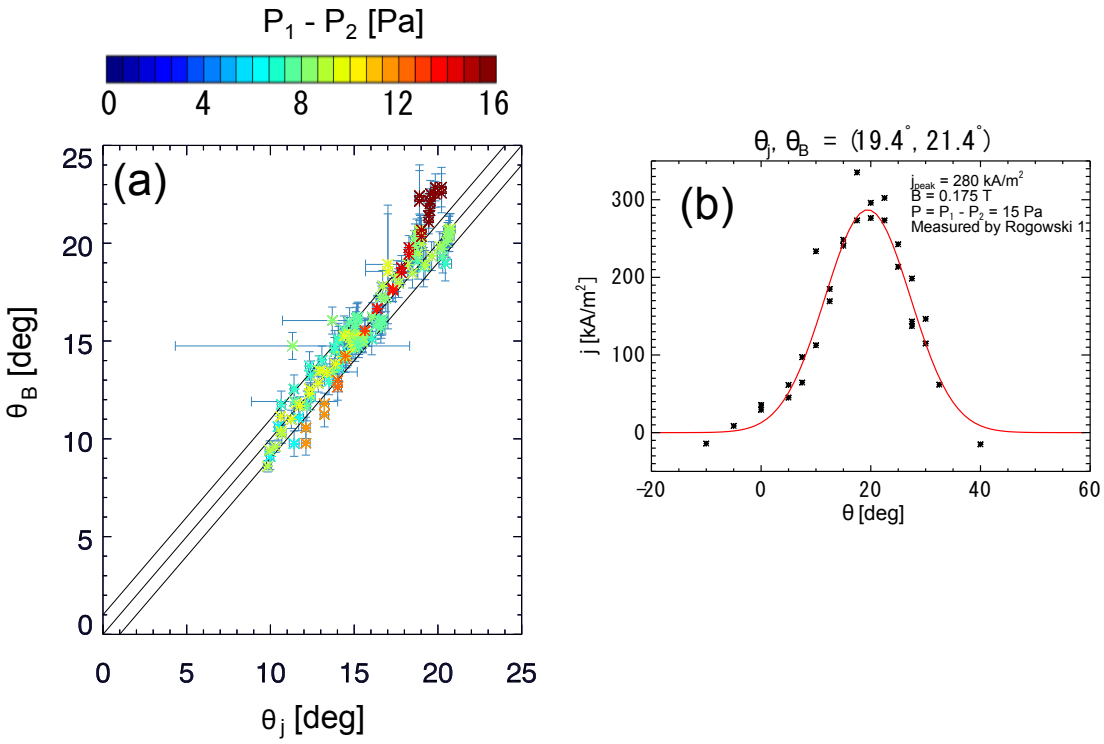

Fig. 6.3: The relationship between θ_j, θ_B, and the difference of the electron pressure measured by the Electrode 1 and 2 (P_1 - P_2) (a). Color bar shows the magnitude of the pressure difference averaged over 1 ms. Angle dependence for a representative case where the angle difference is more than 2° (b). Black symbols represent the data points and red curve represents the fitting result.

to pass through the hole without making one Larmor motion, and the electrons which have parallel velocities equivalent to the electron temperature of 7 keV can pass through the hole. The effect of the high energy electron is one of the probable reason to cause the difference between θ_B and θ_j. Actually, there is a possibility that the number of high energy electrons in the peripheral region is larger than that in core region [87]. Fig. 6.5 shows the time evolutions of SBD signals for the 3 types of plasma discharges. The clear emissions can be seen in the high I_{p} case. The difference between θ_{j} and θ_{B} is larger than the error bars and we can see that θ_{j} deviates from θ_{B} when the edge pressure gradient and the SBD emissions are large.

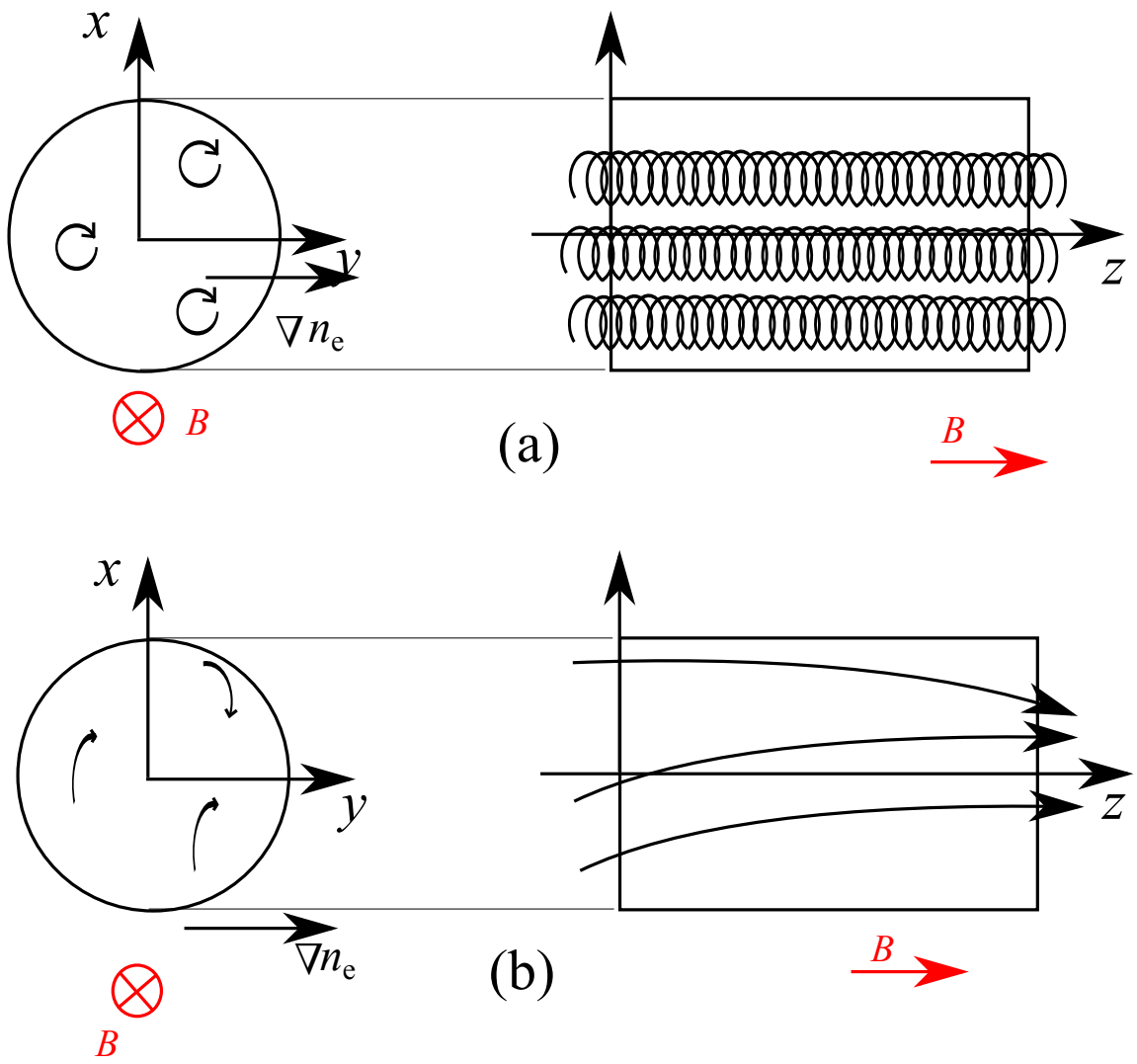

Fig. 6.4: Electron Larmor orbits inside the hole of a Rogowsk coil in the presence of density gradient ∇n_{e}. The case with small parallel electron velocities (a) and the case with electron orbits with high parallel velocities (b) are shown.

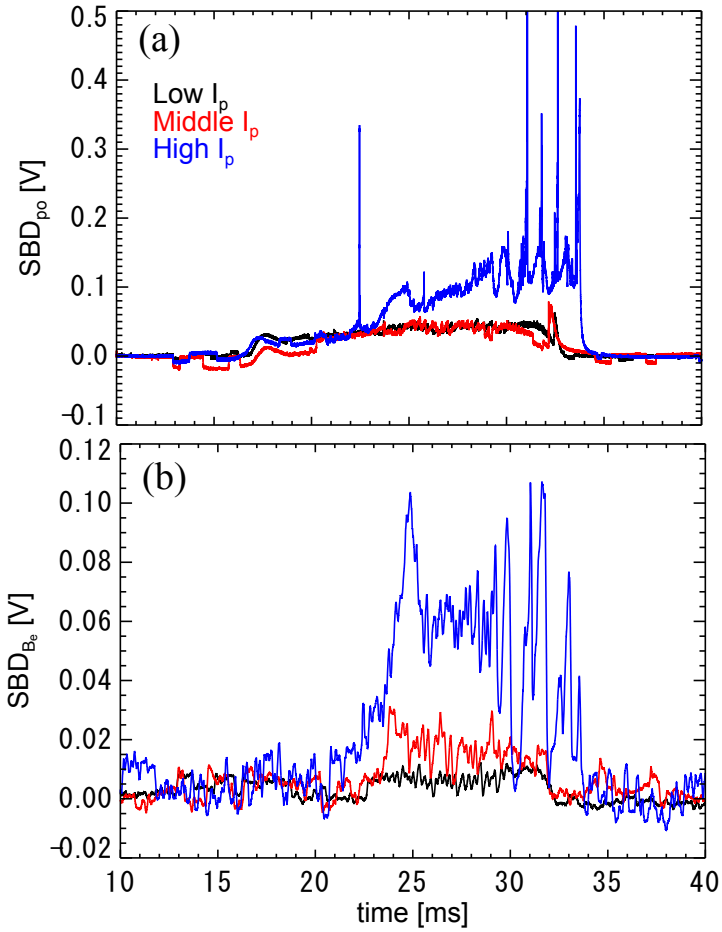

Fig. 6.5: Time evolutions of SBD ((a) Polypropylene and Beryllium) signal for the 3 types of plasma discharges.

6.3 Plasma wall interaction

Issues of plasma wall interactions are frequently important for the diagnostics with an insertion of materials toward plasmas, and there are various considerations for the interactions such as plasma sheath, secondary electron emission and increase of impurities near the surface. As described in Chap. 4, we have already investigated the sheath effect on the Rogowski coil diagnostics and we concluded that it's effect on the measurement of $j_{\parallel}$ is small. As shown in [88], secondary electrons are emitted when electrons collide with the ceramic surfaces. Here, we consider the case with $\theta = 0°$. When the direction of the hole is parallel to the direction of B, most of electrons can pass through the hole gyrating around $\boldsymbol{B}$, and describing $E \times B$ drift without collisions with the ceramic inner surface of the hole. Although electrons with large Larmor radii which are comparable to the radius of the hole can collide with the ceramic surface, the number of such electrons is much smaller than the electrons with small Larmor radii. In addition, even if a secondary electron is emitted due to the collision, the charge will be conserved. Thus, the effect of the collision on the measured $j_{\parallel}$ is quite small.

In Fig. 5.28 (see Sec. 5.4.4), we found that strong visible light emissions from the Rogowski probe appear when the large instabilities occur in TST-2 Ohmic discharges. This emission is probably due to the impurities produced by the electrons hitting the probe surface. In such cases, $T_{\rm e}$ may become small and $n_{\rm e}$ may become large near the surface. Since Debye sheath length is in proportion to $\sqrt{T_{\rm e}/n_{\rm e}}$, the sheath effect becomes small. In addition, a large decrease in $T_{\rm e}$ measured by Electrodes 1 and 2 was not observed during the large instabilities (see Fig. 5.12). The clear increase of $n_{\rm e}$ can be seen during the instabilities. It is not caused by the increase of impurity but it is caused by a high density structure crossing around the region of the Rogowski probe head (see Secs. 5.4, 5.4.3, 5.4.4 and 5.4.6). Thus, actually, the decrease and increase of $T_{\rm e}$ and $n_{\rm e}$ due to the electrons is quite small. Thus, the effect of the impurity emission on the diagnostic is small.

On the whole, we consider that the plasma wall interaction for the Rogowski probe diagnostic is quite small.

Chapter 7

Conclusions

This study consists of two main parts. One is the development of a small and multi-layer Rogowski coil for a current density diagnostic in a tokamak. Second is the studies of plasma equilibrium and instabilities in the TST-2 spherical tokamak device using a Rogowski probe, which contains the developed Rogowski coils.

In order to measure the internal current density with a high signal to noise (SN) ratio, a small Rogowski coil with high precision windings and uniformities (which enable small sensitivities to external currents or external magnetic field), large number of turns (which lead to large sensitivity to the current passing through the hole of a Rogowski coil) is required. In order to fabricate such a Rogowski coil, we devised a new winding pattern with high uniformities. We also used a twisted cable to increase the number of turns and to shorten the fabrication time and to make the coil durable. We call a Rogowski coil fabricated by this method as the small and multi-layer Rogowski coil. Using this Rogowski coil, we have successfully measured the edge current density in TST-2 Ohmic plasma discharges. The resultant SN ratio was estimated to be larger than 20.

We fabricated a Rogowski probe consisting of two multi-layer Rogowski coils, five pick-up coils and two Langmuir probes. The features of this Rogowski probe is that, it can be moved along the major radius of the tokamak and rotated around the shaft axis (in the toroidal-poloidal plane). As a result, the radial current density, magnetic field and pressure profiles and the angular dependence in the toroidal-poloidal plane were obtained. The angular dependence cannot be interpreted by the geometrical structure of the Rogowski probe. For example, a finite current signal was detected when the magnetic field cannot pass through the hole. In order to interpret such phenomena theoretically we have developed a numerical model and analytical model, which include the sheath effect and $E \times B$ drift effect. The experimental angular dependence was quantitatively reproduced by the numerical model and some plasma parameter dependences are confirmed experimentally. While the angular dependence shows a clear sheath (and $E \times B$) effects, the maximum value of the current density (at $\theta = 0°$) was found to be insensitive to such sheath effects under the present plasma parameters.

We have measured the radial current density profile in Ohmic plasma discharges. From the experiment, we have found that there is finite current in the (SOL) region of $R \geq R_{\mathrm{ant-lim}}$ for outboard-limited plasmas. Obviously, such finite current is inconsistent to the results of EFIT code, which cannot take into account SOL current without toroidal symmetry. On the other hand, good agreements were found for the edge region of inboard-limited plasmas. These results indicate that the measured current density profile should be used to improve the accuracy of equilibrium reconstruction.

The measurements for RF startup plasmas were also performed. The equilibrium analysis

or magnetic measurements in TST-2 and LATE suggest a high edge plasma current density. By using the Rogowski probe, we successfully and directly observed such high current density for the first time in a plasma initiated by the dielectric loaded 4-waveguide array (GRILL) antenna. Although we confirmed large edge current density, the position for the large current density is different from that obtained by equilibrium calculation, which allows finite current at the open field line region. These results imply that the accuracy of equilibrium reconstruction can be improved by the Rogowski coil measurements.

In the studies of stabilities, we mainly analyzed IREs in TST-2 Ohmic plasmas. From the SXR emissions and the magnetic signals measured by pick-up coils located inside the vacuum vessels, it was found that positive spikes of SBD signals and low frequency magnetic field fluctuations are two main precursors for the IREs which induce disruptions. Comparing the signals which reflect global structures and the (local) signals measured by the Rogowski probe, it was indicated that the low frequency fluctuations occur near the core regions, while the high frequency fluctuations are related to the changes in current density profile, pressure and q. Besides the IREs, the Rogowski probe signals and the visible light emissions detected by fast visible camera indicated a high density and a high current filamentary structure during instabilities. These results demonstrated the Rogowski probe is also a powerful tool to measure and study such localized structures in tokamak plasmas.

Finally, we have developed a high-performance Rogowski coil and a probe containing two of them. We have demonstrated that the Rogowski coil is a powerful tool for the current density diagnostic due to its capability of the direct measurement.

Acknowledgement

I would like to express my gratitude for people who helped me to complete this thesis. Firstly, I would like to thank Professor Yuich Takase. He is my supervisor and he has given many suggestions for my research through out past five years. He is an excellent professor since he is always willing to respect what students have done and what they have experienced. Thanks to that, I could have a variety of excited experience and I was able to grow up very much compared to the before my coming to this laboratory. Especially, he always guided me to think by myself when I faced difficulties in my research, and I was able to learn how to think and how to execute to solve a difficulty by myself. I am grateful really to Prof. Takase. Secondary, I would like to thank to Associate Professor Akira Ejiri. He also has given many suggestions and advised me to advance my research. He always spends much time for educations of students, and spends much time for research discussions with us. Even if it is a holiday, he always helps us to make progress our research. Actually, his contribution in my research progress is much large. In this five years, occasionally, he gave me a challenging proposition and I had many times to give up my research. However, now, I do believe that my success of the development of the diagnostic using a Rogowski probe is due to his proposition, and I learned it is quite important to do something without giving up all the way to the end. Thirdly, I ' m grateful to Yoshihiko Nagashima. He is now Associate Professor in Kyushu University, and he was Assistant Professor in Takase-ejiri laboratory four years ago. My research of using a small Rogowski coil is originated from his idea. At first, when I started my research, I had many difficulties to develop the Rogowski probe system, and I asked him many questions. In spite of that he had many tasks in Kyushu University, he always responded to my questions in detail. In addition, when I visited Kyushu University for the discussion with him, he made lots of time for me, even when he is busy. I cannot thank enough for his cooperation. Naoto Tsuji is now Assistant Professor in Takase-ejiri laboratory. He was coming in the laboratory after my coming to the lab. He graduated MIT (Massachusetts Institute of Technology) and He always taught me forefront science and technology of tokamak fusion physics. His advice and comments have always excited and surprised me to raise my motivation to fusion research. Mr. Saito is a technician and he is working on the graduate school of the University of Tokyo in Kashiwanoha campus. It is not too much to say that the success of the development of the multi-layer Rogowski coil is thanks to him. Without his help, I was not able to fabricate coil cores for tests, and to learn manufacturing. I can't thank him enough.

From here, I would like to express my gratitude for my colleagues. Mr. Takahiro Shinya is one of the colleagues who have the longest relationship with me in the lab. He has been working on RF startup experiments and he is very good at developments and fabrications of many kinds of devices. From his working, I could have learned many things. He is a very cheerful person and he can make better atmosphere in the laboratory room. Thanks to him, I could have been enjoyed to study every day and every time for five years. In addition,

I always have been playing tennis with Prof. Takase, Mr. Shinya and the other tennis members (Mr. Nakamura, Mr. Kaku) at lunch time. Mr. Shinya started playing tennis from the graduate school. His growing up rate in playing tennis is amazing, and now, he can play tennis at the same level with us. It is deeply in my mind that we won the tennis tournament in Kashiwanoha Campus with the lab members at the end of the year for my PHD.

Mr. Masateru Sonehara is also the colleague who has the longest relationship with me in the lab, and he is a member of the probe team in TST-2 group. For this five years, no newcomers came in our team, and we always worked hard together many times for such as a probe installation for the tokamak, cable wiring and so on. He is very good at physics and when I ask questions about plasma physics to him, he was always willing to answer to my questions.

Mr. Hiro Togashi is the one of the PHD students in the lab. He is also PHD student and he is working on the Thomson scattering diagnostic in TST-2 and QUEST. I went to many places with him in Japan and foreign countries for the study and conferences. I have spent much time for playing tennis in my life. On the other hand, Mr. Togashi may have spent much time for the music, and he knows many things what I don't know and has many kinds of different views. Talking and discussion with him were very interesting and exciting for me, and I could have learned many things from him.

Mr. Takuma Inada, Mr. Kazuhiro Imamura, Mr. Keishun Nakamura, and Mr. Shintarou Tsuda, they have already graduated, but we still have relationships and we often get together for drinking and eating. In this five years, I had many times to face with difficulties in my research. In such a time, they were always playing with me from the night to the morning, then I could tackle many difficulties after that. I'm really grateful to them.

As is mentioned in above, the interesting and bright people including the professors, are coming every year in Takase-ejiri laboratory and thanks to them, I have been able to enjoy the study and to learn many things. Although I would like to express my gratitude for all people, please say a few words for the last for my parents.

When I was a high school student, my dream was to be a professional tennis player and my parents supported me a lot to realize my dream. Now, I know that there are many hardships to support a son who wants to be a professional for some kinds of sports since it costs too much money and time. Nevertheless, my parents admitted me to go to PHD course three years ago. During the past five years, I was able to meet with many excellent people and to have various amazing experiences. It is all thanks to the support of my grateful parents.

Bibliography

[1] Freidberg, J. P. *Plasma physics and fusion energy*. Cambridge university press, (2007).

[2] Goldston, R. J. and Rutherford, P. H. *Introduction to plasma physics*. CRC Press, (1995).

[3] Aymar, R., Barabaschi, P., and Shimomura, Y. *Plasma Physics and Controlled Fusion* **44**(5), 519 (2002).

[4] Wesson, J. and Sykes, A. *Nuclear Fusion* **25**(1), 85 (1985).

[5] KaMaDa, Y. *Journal of Plasma and Fusion Research* **79**(2), 123–135 (2003).

[6] Peng, Y.-K. and Strickler, D. *Nuclear Fusion* **26**(6), 769 (1986).

[7] Nishio, S., Tobita, K., Konishi, S., Ando, T., Hiroki, S., Kuroda, T., Yamauchi, M., Azumi, M., and Nagata, M. In *Proceedings of the 19th IAEA Fusion Energy Conference (Lyon) FT/P1-21*, (2002).

[8] KaMaDa, Y. *Journalof Plasma and Fusion Research* **86**(4), 240–246 (2010).

[9] Tobita, K., Nishio, S., Sato, M., Sakurai, S., Hayashi, T., Shibama, Y., Isono, T., Enoeda, M., Nakamura, H., Sato, S., Ezato, K., Hayashi, T., Hirose, T., Ide, S., Inoue, T., Kamada, Y., Kawamura, Y., Kawashima, H., Koizumi, N., Kurita, G., Nakamura, Y., Mouri, K., Nishitani, T., Ohmori, J., Oyama, N., Sakamoto, K., Suzuki, S., Suzuki, T., Tanigawa, H., Tsuchiya, K., and Tsuru, D. *Nuclear Fusion* **47**(8), 892 (2007).

[10] Takase, Y., Ejiri, A., Kasuya, N., Mashiko, T., Shiraiwa, S., Tozawa, L., Akiduki, T., Kasahara, H., Nagashima, Y., Nozato, H., Wada, H., Yamada, H., Yamada, T., and Yamagishi, K. *Nuclear Fusion* **41**(11), 1543 (2001).

[11] Wesson, J. and Campbell, D. *Tokamaks*, volume 149. Oxford University Press, (2011).

[12] Miyamoto, K. *Fundamentals of plasma physics and controlled fusion*. Iwanami Book Service Center, (1997).

[13] Mukhovatov, V. S. and Shafranov, V. *Nuclear Fusion* **11**(6), 605 (1971).

[14] Johnson, J. L., Dalhed, H., Greene, J., Grimm, R., Hsieh, Y., Jardin, S., Manickam, J., Okabayashi, M., Storer, R., Todd, A., et al. *Journal of Computational Physics* **32**(2), 212–234 (1979).

[15] Riemann, K. U. *Journal of Physics D: Applied Physics* **24**(4), 493 (1991).

[16] Stangeby, P. *Nuclear Fusion* **52**(8), 083012 (2012).

[17] Izzo, V. and Parks, P. *Nuclear Fusion* **50**(5), 058001 (2010).

[18] Ejiri, A., Shiraiwa, S., Takase, Y., Yamada, T., Nagashima, Y., Kasahara, H., Iijima, D., Kobori, Y., Nishi, T., Taniguchi, T., et al. *Nuclear fusion* **43**(7), 547 (2003).

[19] Shiraiwa, S., Takase, Y., Ejiri, A., Yamagishi, K., Nagashima, Y., Kasuya, N., Mashiko, T., Nozato, H., Ushigome, M., Tozawa, L., Durah, S., Akiduki, T., Kasahara, H., Yamada, H., Ymada, T., and H, W. *Contr. Fusion and Plasma Phys. B* **24**, 1400 (2000).

[20] Tojo, H., Ejiri, A., Takase, Y., Nagashima, Y., Watanabe, O., Adachi, Y., Oosako, T., Yamaguchi, T., An, B. I., Kobayashi, H., et al. *Plasma and Fusion Research* **4**, 015–015 (2009).

[21] Sykes, A., Bosco, E. D., Colchin, R., Cunningham, G., Duck, R., Edlington, T., Goodall, D., Gryaznevich, M., Holt, J., Hugill, J., Li, J., Manhood, S., Parham, B., Robinson, D., Todd, T., and Turner, M. *Nuclear Fusion* **32**(4), 694 (1992).

[22] Jarboe, T., Gu, P., Izzo, V., Jewell, P., McCollam, K., Nelson, B., Raman, R., Redd, A., Sieck, P., Smith, R., Nagata, M., and Uyama, T. *Nuclear Fusion* **41**(6), 679 (2001).

[23] Semenov, I., Mirnov, S., Darrow, D., Roquemore, L., Fredrickson, E. D., Menard, J., Stutman, D., and Belov, A. *Physics of Plasmas* **10**(3), 664–670 (2003).

[24] Hayashi, T., Mizuguchi, N., Watanabe, T., Todo, Y., Sato, T., and Group, C. S. *Nuclear Fusion* **40**(3Y), 721 (2000).

[25] Mizuguchi, N., Hayashi, T., and Sato, T. *Physics of Plasmas* **7**(3), 940–949 (2000).

[26] Spitzer, J., Ono, M., and Peng, M. *Fusion Technology* **30**(CONF-9606116–) (1996).

[27] Lao, L., John, H. S., Stambaugh, R., Kellman, A., and Pfeiffer, W. *Nuclear Fusion* **25**(11), 1611 (1985).

[28] Hutchinson, I. H. *Principles of plasma diagnostics*. Cambridge university press, (2005).

[29] Langmuir, I. and Mott-Smith, H. *Gen. Elec. Rev* **27**, 449 (1924).

[30] Stangeby, P. C. *Plasma Physics and Controlled Fusion* **37**(9), 1031 (1995).

[31] EJIRI, A., YAMAGUCHI, T., HIRATSUKA, J., TAKASE, Y., HASEGAWA, M., and NARIHARA, K. *Plasma and Fusion Research* **5**, S2082–S2082 (2010).

[32] Babický, V., Koláček, K., Ullschmied, J., and Malych, N. *Czechoslovak Journal of Physics B* **27**(10), 1125–1128 (1977).

[33] *Plasma Boundary Reconstruction using Fast Camera on the COMPASS Tokamak*. MATFYZPRESS, (2014).

[34] Koch, B., Herrmann, A., Kirk, A., Meyer, H., Dowling, J., Harhausen, J., Neuhauser, J., Müller, H., Bohmeyer, W., and Fussmann, G. *Journal of Nuclear Materials* **363–365**, 1056 – 1060 (2007). Plasma-Surface Interactions-17.

[35] `https://www.nacinc.jp/analysis/memrecam-hx-3hx-4hx-5hx-6/`.

[36] Yamasaki, K., Inoue, S., Kamio, S., Watanabe, T. G., Ushiki, T., Guo, X., Sugawara, T., Matsuyama, K., Kawakami, N., Yamada, T., Inomoto, M., and Ono, Y. *Physics of Plasmas* **22**(10) (2015).

[37] Imazawa, R., Nakagawa, M., Kamio, S., Hihara, R., Yamada, T., Inomoto, M., Takase, Y., and Ono, Y. *Electrical Engineering in Japan* **179**(2), 20–26 (2012).

[38] Inomoto, M., Watanabe, T., Gi, K., Yamasaki, K., Kamio, S., Imazawa, R., Yamada, T., Guo, X., Ushiki, T., Ishikawa, H., Nakamata, H., Kawakami, N., Sugawara, T., Matsuyama, K., Noma, K., Kuwahata, A., and Tanabe, H. *Nuclear Fusion* **55**(3), 033013 (2015).

[39] Liewer, P. C. *Nuclear Fusion* **25**(5), 543 (1985).

[40] Shen, W., Dexter, R. N., and Prager, S. C. *Phys. Rev. Lett.* **68**(0), 1219–1233 Mar (1992).

[41] Stoneking, M. R., Hokin, S. A., Prager, S. C., Fiksel, G., Ji, H., and Den Hartog, D. J. *Phys. Rev. Lett.* **73**(0), 549–552 Jul (1994).

[42] Fluctuation and transport reduction in a reversed field pinch by inductive poloidal current drive. *Phys. Rev. Lett.* **72**(0), 3670–3673 Jun (1994).

[43] Nagata Masayoshi, Kanki Takashi, F. N. and Tadao, U. .

[44] Wagner, F., Fussmann, G., Grave, T., Keilhacker, M., Kornherr, M., Lackner, K., McCormick, K., Müller, E. R., Stäbler, A., Becker, G., Bernhardi, K., Ditte, U., Eberhagen, A., Gehre, O., Gernhardt, J., Gierke, G. v., Glock, E., Gruber, O., Haas, G., Hesse, M., Janeschitz, G., Karger, F., Kissel, S., Klüber, O., Lisitano, G., Mayer, H. M., Meisel, D., Mertens, V., Murmann, H., Poschenrieder, W., Rapp, H., Röhr, H., Ryter, F., Schneider, F., Siller, G., Smeulders, P., Söldner, F., Speth, E., Steuer, K. H., Szymanski, Z., and Vollmer, O. *Phys. Rev. Lett.* **53**(0), 1453–1456 Oct (1984).

[45] Wagner, F., Becker, G., Behringer, K., Campbell, D., Eberhagen, A., Engelhardt, W., Fussmann, G., Gehre, O., Gernhardt, J., Gierke, G. v., Haas, G., Huang, M., Karger, F., Keilhacker, M., Klüber, O., Kornherr, M., Lackner, K., Lisitano, G., Lister, G. G., Mayer, H. M., Meisel, D., Müller, E. R., Murmann, H., Niedermeyer, H., Poschenrieder, W., Rapp, H., Röhr, H., Schneider, F., Siller, G., Speth, E., Stäbler, A., Steuer, K. H., Venus, G., Vollmer, O., and Yü, Z. *Phys. Rev. Lett.* **49**(0), 1408–1412 Nov (1982).

[46] Sykes, A., Akers, R. J., Appel, L. C., Carolan, P. G., Connor, J. W., Conway, N. J., Counsell, G. F., Dnestrovskij, A., Dnestrovskij, Y. N., Gryaznevich, M., Helander, P., Nightingale, M. P. S., Ribeiro, C., Roach, C. M., Tournianski, M., Walsh, M. J., Wilson, H. R., Team, T. S., and Team, T. N. *Phys. Rev. Lett.* **84**(0), 295–298 Jan (2000).

[47] Sykes, A., Ahn, J.-W., Akers, R., Arends, E., Carolan, P. G., Counsell, G. F., Fielding, S. J., Gryaznevich, M., Martin, R., Price, M., Roach, C., Shevchenko, V., Tournianski, M., Valovic, M., Walsh, M. J., Wilson, H. R., and Team, M. *Physics of Plasmas* **8**(5), 2101–2106 (2001).

[48] Ono, M., Kaye, S., Peng, Y.-K., Barnes, G., Blanchard, W., Carter, M., Chrzanowski, J., Dudek, L., Ewig, R., Gates, D., Hatcher, R., Jarboe, T., Jardin, S., Johnson, D.,

Kaita, R., Kalish, M., Kessel, C., Kugel, H., Maingi, R., Majeski, R., Manickam, J., McCormack, B., Menard, J., Mueller, D., Nelson, B., Nelson, B., Neumeyer, C., Oliaro, G., Paoletti, F., Parsells, R., Perry, E., Pomphrey, N., Ramakrishnan, S., Raman, R., Reweldt, G., Robinson, J., Roquemore, A., Ryan, P., Sabbagh, S., Swain, D., Synakowski, E., Viola, M., Williams, M., Wilson, J., and Team, N. *Nuclear Fusion* **40**(3Y), 557 (2000).

[49] Bongard, M. W., Fonck, R. J., Hegna, C. C., Redd, A. J., and Schlossberg, D. J. *Phys. Rev. Lett.* **107**(4), 035003 (2011).

[50] Connor, J. W. *Plasma Physics and Controlled Fusion* **40**(5), 531 (1998).

[51] Bock, M. F. M. D., Citrin, J., Saarelma, S., Temple, D., Conway, N. J., Kirk, A., Meyer, H., Michael, C. A., and the MAST team. *Plasma Physics and Controlled Fusion* **54**(2), 025001 (2012).

[52] Shevchenko, V., De Bock, M., Freethy, S., Saveliev, A., and Vann, R. *Fusion Science and technology* **59**(4), 663–669 (2011).

[53] Bongard, M. W., Fonck, R. J., Lewicki, B. T., and Redd, A. J. .

[54] Shinya, T., Takase, Y., Wakatsuki, T., Ejiri, A., Furui, H., Hiratsuka, J., Imamura, K., Inada, T., Kakuda, H., Kasahara, H., et al. *Nuclear Fusion* **55**(7), 073003 (2015).

[55] Ishiguro, M., Hanada, K., Liu, H., Ogata, R., Isobe, M., Tashima, S., Zushi, H., Sato, K., Fujisawa, A., Nakamura, K., Idei, H., Sakamoto, M., Hasegawa, M., Takase, Y., Maekawa, T., Kishimoto, Y., Mitarai, O., Kawasaki, S., Nakashima, H., and Higashijima, A. *Journal of Physics: Conference Series* **511**(1), 012041 (2014).

[56] Tanaka, H., Maekawa, T., Uchida, M., Yoshinaga, T., Nishi, S., Yamada, J., Matsumoto, T., Tanahashi, T., Yoshida, K., Yamahana, Y., et al. Technical report, EX/P6-6, (2006).

[57] Shevchenko, V., O'Brien, M., Taylor, D., Saveliev, A., and team, M. *Nuclear Fusion* **50**(2), 022004 (2010).

[58] Ejiri, A., Takase, Y., Kasahara, H., Yamada, T., Hanada, K., Sato, K. N., Zushi, H., Nakamura, K., Sakamoto, M., Idei, H., Hasegawa, M., Iyomasa, A., Imamura, N., Esaki, K., Kitaguchi, M., Sasaki, K., Hoshika, H., Mitarai, O., and Nishino, N. *Nuclear Fusion* **46**(7), 709 (2006).

[59] Two-Fluid Equilibrium Considerations of Te/Ti $\gg$ 1, C. S. P. S. b. R. E. H. *Plasma Fusion Res* **9**(3403146) (2014).

[60] Wakatsuki, T., Ejiri, A., Kakuda, H., Takase, Y., Ambo, T., Furui, H., Hashimoto, T., Hiratsuka, J., Kasahara, H., Kato, K., et al. *IEEJ* **132**(7), 485–489 (2012).

[61] Wakatsuki, T., Ejiri, A., Shinya, T., Takase, Y., Furui, H., Hiratsuka, J., Imamura, K., Inada, T., Kakuda, H., Kasahara, H., Nagashima, Y., Nakamura, K., Nakanishi, A., Oosako, T., Saito, K., Seki, T., Sonehara, M., Togashi, H., Tsuda, S., Tsujii, N., and Yamaguchi, T. *Nuclear Fusion* **54**(9), 093014 (2014).

[62] Kirk, A., Koch, B., Scannell, R., Wilson, H. R., Counsell, G., Dowling, J., Herrmann, A., Martin, R., and Walsh, M. *Phys. Rev. Lett.* **96**(4), 185001 (2006).

[63] Hutchinson, I. H. *Phys. Rev. Lett.* **37**(0), 338–341 (1976).

[64] Giannone, L., Cross, R., and Hutchinson, I. *Nuclear Fusion* **27**(12), 2085 (1987).

[65] Yang, J., Lee, J. W., Jung, B. K., Chung, K. J., and Hwang, Y. S. .

[66] Rogowski, W. and Steinhaus, W. *Electrical Engineering (Archiv fur Elektrotechnik)* **1**(4), 141–150 (1912).

[67] Tumanski, S. *Measurement Science and Technology* **18**(3), R31 (2007).

[68] Narayanan, R. and Sekar Iyengar, A. N. *Review of Scientific Instruments* **77**(3), – (2006).

[69] Abdallh, A. A.-E. and Dupré, L. *Measurement Science and Technology* **21**(10), 107003 (2010).

[70] Levinton, F. M., Fonck, R. J., Gammel, G. M., Kaita, R., Kugel, H. W., Powell, E. T., and Roberts, D. W. *Phys. Rev. Lett.* **63**(0), 2060–2063 Nov (1989).

[71] Shevchenko, V. *Plasma Physics Reports* **26**(12), 1000–1004 (2000).

[72] FURUI, H., NAGASHIMA, Y., TAKASE, Y., EJIRI, A., KAKUDA, H., SONEHARA, M., OOSAKO, T., TSUJII, N., HIRATSUKA, J., IMAMURA, K., et al. *Plasma Fusion Res* **9**, 342078 (2014).

[73] Ray, W. and Hewson, C. *Power electronic measurements Ltd* (2000).

[74] Furui, H., Nagashima, Y., Takase, Y., Ejiri, A., Kakuda, H., Sonehara, M., Oosako, T., Tsujii, N., Hiratsuka, J., Imamura, K., et al. *Review of Scientific Instruments* **85**(11), 11D813 (2014).

[75] Paul, M. K., Chattopadhyay, P. K., and Bora, D. *Measurement Science and Technology* **18**(8), 2673 (2007).

[76] Furui, H., Nagashima, Y., Takase, Y., Ejiri, A., Kakuda, H., Sonehara, M., Oosako, T., Tsujii, N., Hiratsuka, J., Imamura, K., et al. *Review of Scientific Instruments* **85**(11), 11F9903 (2014).

[77] Chodura, R. *Physics of Fluids* **25**(9), 1628–1633 (1982).

[78] Kono, A. *Journal of Physics D: Applied Physics* **37**(14), 1945 (2004).

[79] Brooks, J. N. *Physics of Fluids B* **2**(8), 1858–1863 (1990).

[80] Brooks, J. N. *Physics of Fluids B* **2**(8), 1858–1863 (1990).

[81] Schmitz, H., Riemann, K., and Daube, T. *Physics of Plasmas* **3**(7), 2486–2495 (1996).

[82] Hutchinson, I. H. *Physics of Plasmas (1994-present)* **9**(5), 1832–1833 (2002).

[83] Takase, Y., Ejiri, A., Kakuda, H., Oosako, T., Shinya, T., Wakatsuki, T., Ambo, T., Furui, H., Hashimoto, T., Hiratsuka, J., Kasahara, H., Kato, K., Kumazawa, R., Moeller, C., Mutoh, T., Nakanishi, A., Nagashima, Y., Saito, K., Sakamoto, T., Seki, T., Sonehara, M., Shino, R., Togashi, H., Watanabe, O., and Yamaguchi, T. *Nuclear Fusion* **53**(6), 063006 (2013).

[84] Sonehara, M., Nagashima, Y., Takase, Y., Ejiri, A., Yamaguchi, T., Ambo, T., Kakuda, H., Hiratsuka, J., Sakamoto, T., Shino, R., et al. *IEEJ* **132**(7), 499–504 (2012).

[85] Tojo, H., Gryaznevich, M. P., Ejiri, A., Sykes, A., and Takase, Y. *Plasma and Fusion Research* **3**, S1065–S1065.

[86] Buttery, R., Bevir, M., Caloutsis, A., Gates, D., Gimblett, C., Gryaznevich, M., Hender, T., Jenkins, I., Sykes, A., Valovic, M., et al. (1996).

[87] Hiratsuka, J., EJIRI, A., HASEGAWA, M., NAGASHIMA, Y., NAKAMURA, K., TAKASE, Y., TOGASHI, H., and TOJO, H. *Plasma Fusion Res.* **10** (2015).

[88] Elizondo, J. M., Meredith, K., and Lapetina, N. *Plasma Science, IEEE Transactions on* **30**(5), 1955–1960 (2002).